

MODELS FOR BROWNIAN AND BIOMOLECULAR MOTORS

by

ERIN MICHELLE CRAIG

A DISSERTATION

Presented to the Department of Physics
and the Graduate School of the University of Oregon
in partial fulfillment of the requirements
for the degree of
Doctor of Philosophy

September 2008

University of Oregon Graduate School

Confirmation of Approval and Acceptance of Dissertation prepared by:

Erin Craig

Title:

"Models for Brownian and biomolecular motors"

This dissertation has been accepted and approved in partial fulfillment of the requirements for the degree in the Department of Physics by:

Roger Haydock, Chairperson, Physics
Heiner Linke, Member, Physics
Stephen Remington, Member, Physics
Daniel Steck, Member, Physics
Marina Guenza, Outside Member, Chemistry

and Richard Linton, Vice President for Research and Graduate Studies/Dean of the Graduate School for the University of Oregon.

September 6, 2008

Original approval signatures are on file with the Graduate School and the University of Oregon Libraries.

© September 2008, Erin Michelle Craig

An Abstract of the Dissertation of

Erin Michelle Craig for the degree of Doctor of Philosophy

in the Department of Physics to be taken September 2008

Title: MODELS FOR BROWNIAN AND BIOMOLECULAR MOTORS

Approved: _____
Dr. Heiner Linke

Biological molecular motors, which use chemical energy from ATP hydrolysis to generate mechanical force, are involved in a variety of important mechanical processes in eukaryotic cells, such as intracellular transport, cell division and muscle contraction. These motors, which produce motion on the nanoscale, operate in the presence of substantial thermal noise.

In this dissertation, two approaches are used to model the physics of nanoscale motors: (1) A theoretically established type of Brownian motor called the “flashing ratchet” is studied. This motor transports diffusive particles in a preferred direction. (2) A coarse-grained mechanical model for the biological molecular motor myosin-V is developed, and used to study the role of Brownian diffusion, and the interaction

between chemical and mechanical degrees of freedom, in the transport mechanism of this motor.

In chapter III, Brownian dynamics simulations and analytical calculations demonstrate that the average velocity of rigid chains of particles in a flashing ratchet reverses direction in response to changing the size of the chain or the temperature of the heat bath.

Recent studies have introduced policies for “closed-loop” control of a flashing ratchet, in which the system is controlled based on information about its internal state (such as the positional distribution of particles). In chapter IV, the effect of time delay on the implementation of closed-loop control of a flashing ratchet is investigated. For a large ensemble, a well-chosen delay time improves the ratchet performance (increasing the velocity) by synchronizing into a quasi-stable mode that takes advantage of the semi-deterministic nature of the time development of average quantities for a large ensemble.

In chapter V, a coarse-grained mechanical model is presented for the transport mechanism of myosin-V, which walks along intracellular filaments. The model is well constrained by experimental data on the mechanical properties of myosin V and on the kinetic cycle. An experimentally motivated model for the intramolecular coordination of the motor’s steps is proposed and tested.

CURRICULUM VITAE

NAME OF AUTHOR: Erin Michelle Craig

PLACE OF BIRTH: Spokane, Washington

DATE OF BIRTH: July 17, 1980

GRADUATE AND UNDERGRADUATE SCHOOLS ATTENDED:

University of Oregon, Eugene, Oregon
Washington State University, Pullman, Washington

DEGREES AWARDED:

Doctor of Philosophy in Physics, 2008, University of Oregon
Master of Science in Physics, 2004, University of Oregon
Bachelor of Science in Physics, 2002, Washington State University

AREAS OF SPECIAL INTEREST:

Biological physics
Molecular machines
Brownian motors
Feedback control of noisy systems

PROFESSIONAL EXPERIENCE:

Graduate Research Fellow,
University of Oregon, 2007 - 2008
Graduate Teaching Fellow,
University of Oregon, 2002 - 2007
Teaching Assistant,
Washington State University, 1999 - 2002

GRANTS, AWARDS AND HONORS:

NSF IGERT Research Fellowship, Materials Science Institute, University of Oregon, Eugene, OR, 2007-2008

NSF IGERT travel award, Materials Science Institute, University of Oregon, Eugene, OR, 2004-2005, 2005-2006

NSF GK-12 teaching fellowship, Materials Science Institute, University of Oregon, Eugene, OR, 2003-2004, 2005-2006

Claire May Band Award for Women in Physics, Washington State University, Pullman, WA, 1999-2000

Paul A. Bender Award for Freshmen in Physics, Washington State University, Pullman, WA, 1998-1999

PUBLICATIONS:

B. J. Lopez, N. J. Kuwada, E. M. Craig, B. R. Long and H. Linke, "Realization of a feedback-controlled flashing ratchet", manuscript submitted to Phys. Rev. Lett.

E. M. Craig, N. J. Kuwada, B. J. Lopez, and H. Linke, "Feedback control in flashing ratchets," Ann. Phys. (Berlin), **17**, 115 (2008).

E. M. Craig, B. R. Long, J. M. R. Parrondo, and H. Linke, "Effect of time delay on feedback control of a flashing ratchet," Europhys. Lett. **81**, 10002 (2008).

E. M. Craig, M. J. Zuckermann, and H. Linke, "Mechanical coupling in flashing ratchets," Phys. Rev. E **73**(5), 051106 (2006).

M. T. Downton, M. J. Zuckermann, E. M. Craig, M. Plischke, and H. Linke, "Single-polymer Brownian motor: A simulation study," Phys. Rev. E **73**(1), 011909 (2006).

ACKNOWLEDGEMENTS

First and foremost, I would like to thank my research advisors Professor Heiner Linke from UO and Professor Martin Zuckermann from Simon Fraser University. Professor Linke and Professor Zuckermann have been a constant source of encouragement, ideas, and thoughtful advice. I have learned a lot from them and am grateful for all the opportunities they have given me to grow as an individual and as a scientist.

I would like to thank Professor Michael Plischke and Dr. Matthew Downton, who contributed substantially to the development of my research through help with programming, careful reading of manuscripts, and countless helpful discussions. I am also grateful to my dissertation committee, whose constructive feedback has contributed to the development of my research.

I have greatly benefited from detailed discussions about myosin-V with Dr. Alex Dunn and Dr. Giovanni Cappello, who have given helpful feedback on the myosin-V model presented here and whose experimental results were a source of inspiration for the model. I am also grateful to Professor Ivan Raymont for helpful feedback on the structural assumptions of our myosin-V model. Many thanks to Professor Juan Parrondo for discussions that contributed to the study of time-delayed feedback control of flashing ratchets.

I am grateful for funding and career development opportunities from the UO Materials Science Institute through the NSF GK-12 teaching program and the NSF

IGERT program. The research in this dissertation was enabled by use of the IRMACS computing facilities and Academic Computing resources at Simon Fraser University.

I would like to thank all of my colleagues and friends in the Linke research group. I have learned a lot from discussions and collaborative work with Brian Long, Ruth Saunders, Benjamin Lopez and Nathan Kuwada.

Mom and Dad, I am truly grateful and can not even begin to thank you enough for all that you have done for me over the years. To my sister, Kelli Craig, my father and mother in-law, Arthur and Janet Ricketson, my grandma Tillie Goertzen, as well as aunts, uncles, cousins, and friends: Thank you for your encouragement and support.

Last but not least, I would like to thank my husband Derek Ricketson – for listening and giving helpful suggestions on the myosin-V project, for encouraging me when I was discouraged, for having confidence in me, and most of all for being the person who makes me happy on a daily basis.

TABLE OF CONTENTS

Chapter	Page
I. INTRODUCTION	1
Molecular Motors	1
Brownian Motors	5
Role of Mechanical Coupling in Brownian Motors	10
Feedback Control of Brownian Motors	13
Experimental Realization of a Feedback-controlled Flashing Ratchet	21
Myosin-V: A Biological Molecular Motor	22
II. MOLECULAR DYNAMICS SIMULATION METHODS	38
Basic Verlet Algorithm	39
Leapfrog Algorithm	40
Langevin Dynamics: Molecular Dynamics With an Implicit Solvent	42
Overdamped Langevin Dynamics	44
Organization of Simulation Programs	45
III. COUPLED MOTION IN A BROWNIAN RATCHET	48
Introduction	48
Model	49
Coupled Motion in Low-temperature Regime	51
Temperature Dependence	61
Coupled Motion in Three Dimensions	64
Finite-sized Spherical Bead in a Quasi-one-dimensional Ratchet	65
IV. DELAYED FEEDBACK CONTROL OF FLASHING RATCHETS	74
Introduction	74
Model	75
Implementation Delay	77
Measurement Delay	85
Experimental Feasibility	91
Concluding Remarks	97

Chapter	Page
V. MECHANICAL MODEL FOR MYOSIN-V WALKING MECHANISM	99
Introduction	99
Predominant Mechanochemical Cycle	103
Structural Assumptions for Minimal Mechanical Model	106
Semi-flexible Polymer Model for Myosin-V Neck Domains	108
Combined Mechano-chemical Simulations	111
Choice of Input Parameters	114
Average Motion During a Step: Comparison with Experiments	117
Coordination of Stepping: Strain-dependent Internal Feedback	128
Tethered Diffusion of the Detached Head in the One-head-bound State	137
Concluding Remarks	143
VI. DISCUSSION AND OUTLOOK	146
Coupled Motion in Flashing Ratchets	147
Mechanical Model for Myosin-V Walking Mechanism	151
APPENDIX: SIMULATIONS OF MECHANICAL MODEL FOR MYOSIN-V	157
Neck Domain Joints	157
Head-neck Junctions	159
Distance Constraints	161
First Passage Time for the Diffusional Search of a Detached Head	162
BIBLIOGRAPHY	164

LIST OF FIGURES

Figure	Page	
1.1	Active transport in eukaryotic cells	3
1.2	Schematic: flashing ratchet	7
1.3	Simulations: Comparison between feedback control schemes	18
1.4	Schematic of myosin-V structure	24
1.5	Hand-over-hand stepping	25
1.6	Schematic of hypothetical stepping mechanism	28
1.7	Average of experimental step trajectory for myosin-V	31
1.8	Experimental observation of tethered diffusion of detached head	33
3.1	Sawtooth ratchet potential	50
3.2	Effective potential for dimer in a ratchet potential	54
3.3	Simulations: Reversal of ratchet velocity for dimers of different length	56
3.4	Effective potential for trimer in a ratchet potential	57
3.5	Simulations: Reversal of ratchet velocity for trimers of different length	59
3.6	Simulations: Multiple reversals for particle chains	60
3.7	Temperature dependence of probability distribution in ratchet potential	62
3.8	Simulations: Reversal of dimer velocity as a function of temperature	63
3.9	Schematic: 3D dimer in a ratchet potential	65
3.10	Simulations: Velocity of a freely-rotating dimer in a flashing ratchet	66
3.11	Schematic: finite-sized bead in a sawtooth ratchet potential	67
3.12	Effective potential for finite-sized bead in a ratchet	70
3.13	Experimental and theoretical effective potential	72
4.1	Schematic: Two possible types of time delay	78
4.2	Simulations: Implementation delay in a feedback-controlled ratchet	79
4.3	Simulations: Average force in a time-delayed feedback ratchet	81
4.4	Simulations: Time-delayed feedback control of a large ensemble	83
4.5	Simulations: Impact of implementation delay and measurement delay	86
4.6	Simulations of mode-locking for a large ensemble	87
4.7	Schematic: Mode-locking with measurement and implementation delays	88
4.8	Feedback control: comparison between theory and experiment	96
5.1	Schematic: predominant chemical cycle for a myosin-V monomer	104
5.2	Schematic: predominant mechano-chemical cycle for a myosin-V dimer	105
5.3	Schematic of mechanical model for myosin-V	110
5.4	Mechanical states for a myosin-V dimer	113
5.5	Schematic: dependence of conformation on filament stiffness	116
5.6	Schematic: Myosin-V “relaxation distance”	122

Figure	Page
5.7 Relaxation distance in the limit of rigid neck domains.....	124
5.8 Simulations: relaxation distance as a function of mechanical parameters	126
5.9 Angular displacement of neck domains in state II	131
5.10 Simulations: Angular sensitivity calibration.....	132
5.11 Simulations: Kinetic asymmetry.....	134
5.12 Brownian dynamics simulations of walking	136
5.13 Simulations: First passage time for diffusional search	140
5.14 Simulations: Dependence of stall force on physical properties of motor	142
A.1 Schematic: Three body interactions in polymer model	158

LIST OF TABLES

Table	Page
5.1 Kinetic Rates for the Chemical Transitions of a Myosin-V Head	106
5.2 Mechanical Parameters	118
5.3 Performance Features	119

CHAPTER I

INTRODUCTION

Molecular Motors

A motor is a machine or device that converts any form of energy into mechanical energy, or imparts motion. On the macroscopic scale, motors are essential to the operation of many man-made machines from cars to computers. Motors also exist in nature on a much smaller size scale: In living systems, molecules called molecular motors convert chemical energy from ATP hydrolysis (or, in some cases, electrical potential differences across membranes) into work. Molecular motors are essential for a wide range of biological functions, including cell division, muscle contraction, DNA replication, and intracellular transport [1].

Eukaryotic cells have a complex internal organization that relies on the ability to transport material to specific locations within the cell. This is made possible through a system of active transport. A network of structurally polar protein filaments called the cytoskeleton makes up the “road” system for active transport within the cell (see fig. 1.1(a)). Molecular motors transport cargo through cells by moving along filaments in a preferred direction. For example, the molecular motors kinesin and dynein both move along microtubule filaments, but kinesin moves toward the plus

end of microtubules (which is typically directed toward the outside of the cell) and dynein moves toward the minus end. The motor myosin-V transports a variety of cargos by moving unidirectionally along actin filaments (fig. 1.1(b)).

Understanding the physical mechanism that these tiny motors use to convert chemical energy into directed motion has posed a challenging task, which has benefited from the contributions of structural studies, biochemical measurement of reaction rates, and motility assays that monitor the motion of the motors under different physical and chemical conditions. Theoretical models have also been instrumental in exploring ideas about how the motors produce motion and force. Some models assume that the motion is tightly coupled to steps in the ATP hydrolysis cycle, such that a stochastic chemical transition triggers a deterministic conformational change (sometimes referred to as a “power stroke”) that drives the motor [3–6]. Others treat the motors as Brownian ratchets, in which the thermal motion of a diffusive object is rectified to produce net motion [7–9]. In these models, the motion is more loosely coupled to the chemical cycle, and fluctuations are essential to the operation of the motor. Some theoretical treatments of molecular motors have begun to include elements of both a power stroke and a Brownian ratchet mechanism [10–12].

In this dissertation, two approaches are used to model the physics of nanoscale motors: First, we study a model for a thermal motor called the “flashing ratchet” in which diffusive particles are transported in a preferred direction [13–15]. This model provides a conceptual testing ground to explore general physical principles

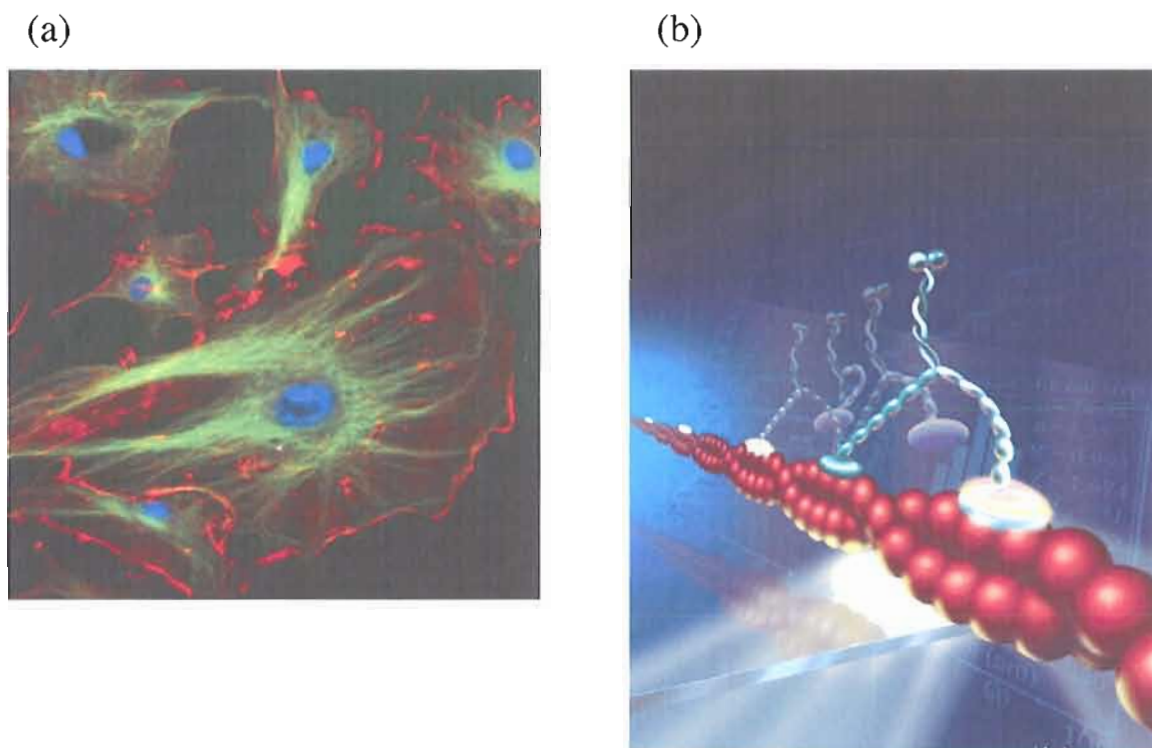


Figure 1.1. Active transport in eukaryotic cells: (a) The cytoskeleton is a dynamic structure composed of filaments that help a cell maintain its shape, and play a role in cellular motility and cell division. In eukaryotic cells, the cytoskeletal filaments also provide tracks on which molecular motors can move unidirectionally to transport cargo to its destination within the cell. In this image of endothelial cells taken by fluorescence microscopy, actin filaments are tagged with a red fluorescent dye, microtubules with green, and the nuclei are stained blue. (Source: <http://rsb.info.nih.gov/ij/images/> (public domain, lacking author information)) (b) This artistic rendition of a myosin-V molecule walking along an actin filament illustrates an example of active transport along cytoskeletal filaments in cells. (Source: Science Magazine [2])

of a system that transports material in the presence of substantial thermal noise. Although the study of this type of motor has been primarily driven by theoretical investigation in the past, one of the key motivations of the research in this dissertation is to help bridge the gap between the models and experimental realization of artificial thermal motors based on the flashing ratchet concept. To this end, we specifically address aspects of the system that are often neglected in theoretical studies, but are likely to play a role in an experiment. For example, we consider the role of time delay in measurement and control of the system. The theoretical predictions in this dissertation have contributed to the design and analysis of an experimental flashing ratchet system. Secondly, we develop a coarse-grained mechanical model for the cytoskeletal motor myosin-V, and use this model to study the role of Brownian diffusion, and the interaction between chemical and mechanical degrees of freedom, in the transport mechanism of this motor.

In this chapter, background material and motivation for each of the topics of research in the dissertation are presented. The concept of Brownian motors is introduced, and an overview is given of past theoretical investigation of the flashing ratchet concept. A brief introduction is given of an experimental flashing ratchet system that Benjamin Lopez in the Linke group is using to test theoretical predictions, including some of the results in this dissertation. At the end of this chapter, the biological motor myosin-V is introduced, detailing some of the key experimental studies that have advanced the understanding of how this motor operates.

The remainder of the dissertation has the following layout: Chapter II describes molecular dynamics simulation methods that are used for the computational research presented in chapters III-V. Chapter III addresses the flashing ratchet transport of mechanically interacting particles and objects with internal structure, showing that the symmetry of the system and the corresponding direction of transport depends critically on the size and shape of the objects being transported. Chapter IV presents a study of the impact of time delay on a feedback control scheme for a flashing ratchet in which the system is controlled based on information about the current state of the system. In chapter V, a mechanical model for the transport mechanism of myosin-V is presented. Chapters III and IV are partially based on published results [16–18]. The myosin-V model presented in chapter V will form the basis for a manuscript that will be prepared for submission to a peer-reviewed journal.

Brownian Motors

Molecular motors such as myosin-V, which produce motion on the nanoscale, are subject to thermal fluctuations in the surrounding environment that are comparable to the energy that drives the motor [19]. Inertial motion is damped out on a time scale given by the ratio of the mass, m , and the drag coefficient, γ , of the object. The small mass of a molecular motor ensures that the characteristic time for momentum relaxation, m/γ , is very small compared to the relevant time scales for the operation of the motor [9]. In other words, the motion of molecular motors is overdamped,

and the effect of inertia is negligible. It is clear that the operation of motors on the nanoscale must be fundamentally different than that of macroscopic motors, which operate in the absence of any significant thermal noise and often include inertial forces as an essential component of their operation. Motors that operate in the overdamped regime must at least tolerate the thermal motion of the environment. Motor designs in which thermal fluctuations play an essential role in the function are referred to as “Brownian motors” [9, 19–23].

A theoretically established type of Brownian motor called the flashing ratchet [13, 14] is often used as a conceptual ‘toy model’ to reveal general principles about the rich dynamics of motors that operate in a thermal environment. In a flashing ratchet (illustrated in fig. 1.2), diffusive particles are subjected to a spatially asymmetric, periodic potential that is switched on and off, either periodically, randomly or by some other protocol. During the off phase, particles diffuse isotropically, producing no net motion in either direction. During the on phase, the particles move toward the minimum of the nearest potential well. Due to the asymmetry of the potential, a majority of particles will move to the right when the potential turns on, assuming that they are evenly distributed at the beginning of the on phase. Over time, this produces a particle current in the $+x$ -direction. The average velocity is sensitive to the amount of time spent in the on and off states, because the mechanism of transport relies on particles having enough time to localize in the potential when it is on, and to diffuse away from the potential minimum when the potential is off.

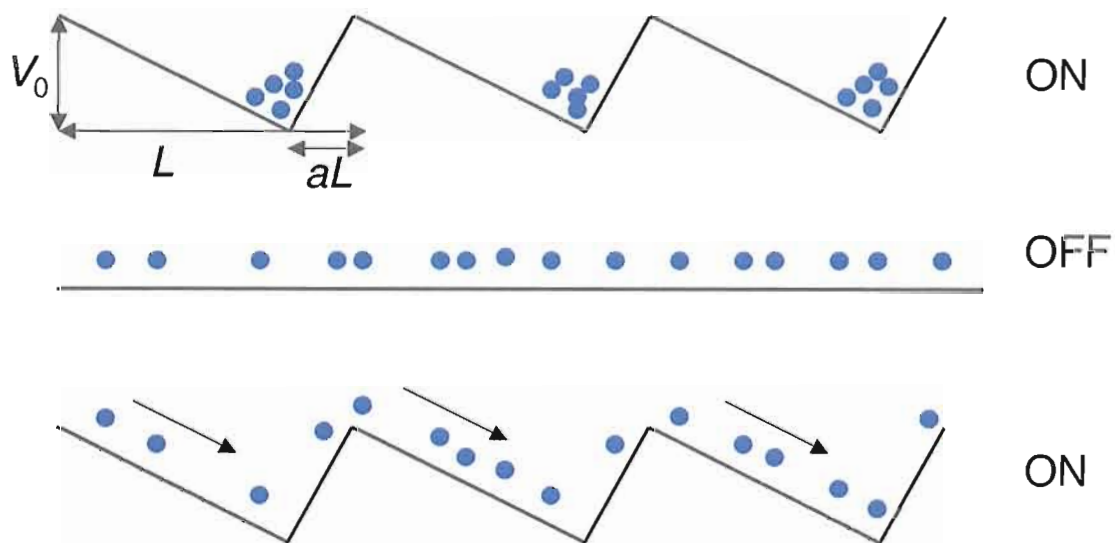


Figure 1.2. Schematic: flashing ratchet. A flashing ratchet is a type of Brownian motor that achieves net transport of diffusive particles by subjecting them to an asymmetric, spatially periodic potential that is turned on and off. When the potential is off, the particles diffuse isotropically. When the potential turns back on, particles move in response to the potential and are localized at the minima of the potential. Due to the asymmetry of the potential, in each temporal cycle the particles are more likely to move to the right by one spatial period than to the left. This produces average particle flux to the right. The piecewise-linear ‘sawtooth’ shape of the potential in this schematic is commonly used for theoretical studies of flashing ratchet transport.

This is an example of a Brownian motor, because the transport mechanism relies on Brownian diffusion. Without diffusion during the off state, particles would never be trapped in a different well than the one they started in, and no net transport would occur. Diffusion in the $+x$ -direction during the off phase is rectified when the potential turns back on, in that particles that have diffused far enough to be trapped in an adjacent well to the right will be pushed forward toward the minimum of that well. Particles that diffuse far enough in the $-x$ -direction will be trapped in an adjacent well to the left, but this happens less often on average because a larger diffusion distance is necessary. The operation of the motor can be described as having two components: (1) a “Brownian ratchet” mechanism in which Brownian diffusion is preferentially rectified for one direction over the other; and (2) a “Power stroke” mechanism in which particles move in response to a large force (in this case, the motion of the particles in response to the potential being turned on).

In general, two features are needed to produce flux in a thermal environment: spatial asymmetry and the input of free energy. Spatial asymmetry is needed to impart motion in a preferred direction. A flashing ratchet accomplishes this with an asymmetrically shaped potential. The input of free energy is needed to bring the system out of thermal equilibrium; If the system is in thermal equilibrium, net transport would violate the Second Law of Thermodynamics [24]. A flashing ratchet is kept out of thermal equilibrium by turning the potential on and off, thus doing work on the particles when the potential turns on. If the potential felt by the particles were

not time-dependent, net transport would not occur: Regardless of the symmetry of the potential, the positional distribution of the particles in thermal equilibrium is time-independent, following the statistics of the Boltzmann distribution: $\rho(x) = e^{-V(x)/kT}$ [25].

The ‘on - off’ flashing ratchet described above can be substantially modified while maintaining the key elements of a Brownian ratchet [22]. For example, net transport in a flashing ratchet occurs for periodic as well as random modulation of the potential [15]. The amplitude of the potential can vary in time, taking on values other than just fully on and fully off [15, 26]. The Brownian ratchet effect also occurs for modified potential shapes, in the presence of inertia [27–30], and when the temperature rather than the potential is modulated [31].

The flashing ratchet is often used as a simple model for cytoskeletal motors such as kinesin and myosin-V, which move along filaments through a series of attachment and detachment as they catalyze ATP hydrolysis. In this analogy, the ratchet potential represents the binding potential along the track, and the time-dependence of the potential reflects changes in a motor’s binding affinity in response to chemical state transitions [8, 9].

Role of Mechanical Coupling in Brownian Motors

The flashing ratchet was first introduced as a mechanism for transporting non-interacting point particles, providing a simple conceptual realization of a thermal motor. However, some recent theoretical studies have considered the transport of objects with internal structure in a flashing ratchet. One motivation is that the directionality of ratchet transport is a consequence of breaking spatial inversion symmetry, and depends sensitively on the parameters of the system [32]; An object with more complicated structure will interact with the potential differently than a point particle, and this can alter the symmetry of the system. In this sense, flashing ratchets (and Brownian motors in general) may provide a route to novel devices for separation of microscopic particles.

A second motivation to study ratchet transport of objects with internal structure is that the structure and internal degrees of freedom of biological molecular motors (i.e., size, flexibility, and the mechanical coordination between different parts of the molecule) are likely to play an essential role in the transport mechanism of these motors. Understanding the role of size, shape and internal degrees of freedom in the operation of a simpler motor system (the flashing ratchet) is not only of fundamental interest, but also could provide insight into how these features are incorporated into the operation of biological molecular motors.

A number of recent theoretical studies have demonstrated qualitatively different behavior for mechanically coupled particles in a flashing ratchet than for non-interacting point particles [33–41]. A few examples include: Two harmonically coupled point particles in a flashing ratchet have slower transport velocity than for uncoupled particles, because the distance the harmonically coupled particles must diffuse to move past a potential barrier is effectively increased [40]. Two harmonically coupled particles can undergo directed transport through a series of conformational changes of the dimer in response to a flashing ratchet potential even in the absence of thermal fluctuations [33, 38], such that the transport is no longer a Brownian motor mechanism that relies on diffusion.

In Downton et al. [41], we present a model for a Brownian motor based on a flexible polymer in a flashing ratchet. In order to test the ability of this motor to do work against an external load, molecular dynamics simulations carried out by Matthew Downton were used to predict the maximum opposing force at which the motor has positive velocity. The force at which the motor has zero velocity is referred to as the stall force. This study demonstrated that when the radius of gyration of the polymer is on the order of several spatial periods of the ratchet potential, the speed and the stall force of the motor are higher than the corresponding values for a bead with the same drag coefficient and a radius much smaller than the ratchet period. In other words, internal degrees of freedom enable the motor to perform more work

against an external load, by making use of advantageous conformational changes in the polymer during the ratchet cycle.

Other theoretical studies of coupled particles in a flashing ratchet focus specifically on course-grained models for biological molecular motors [10, 42–50]. For example, large collections of particles that are harmonically coupled to a rigid backbone and exposed to a flashing ratchet potential undergo spontaneous oscillations [43], which is also observed for myosin-driven muscle contraction. A model for ratchet transport of a particle that is elastically coupled to a cargo much larger than itself demonstrates that the velocity increases with increasing flexibility of the linkage, suggesting a possible transport mechanism of biological molecular motors that do work transporting large cargoes [45].

In chapter III, we present a theoretical investigation of the role of mechanical coupling in a flashing ratchet by considering the simplest form of coupling: point particles held at a fixed distance in a one-dimensional system. A rigid chain of evenly-spaced point particles experiences a different effective potential than an individual point particle, because the net force on the chain is the sum of the forces on individual particles that each sample a different region of the potential. We demonstrate that the velocity of a rigid particle chain in a flashing ratchet can change direction as a function of the separation distance between particles or the temperature of the system, because the symmetry of the effective potential depends on these parameters. Interestingly, establishing a fixed separation distance between particles in a one-dimensional ratchet

is sufficient to alter the symmetry of the system, even though the chains themselves have no inherent directionality.

In an experimental realization of flashing ratchet transport, it is unlikely for the objects being transported to be small enough compared to the spatial period of the ratchet to be considered “points.” If a spherical bead is exposed to an external ‘sawtooth’ potential (fig. 1.2), it will experience an effective potential that is the weighted sum of the potential experienced by each portion of the bead’s volume. At the end of chapter III, we discuss this effect in the context of an experimental flashing ratchet constructed by Ben Lopez in the Linke group [51], which transports colloidal dielectric beads with a flashing ratchet potential realized with a scanning line optical trap [52–55]. The numerical calculation of the effective potential for different bead sizes in a theoretical sawtooth potential is in excellent agreement with experimental characterization of the effective potential experienced by a dielectric bead in the optical ratchet potential.

Feedback Control of Brownian Motors

A flashing ratchet system with a periodically or randomly modulated potential is an example of “open loop” control, in which the control of the system is determined based on some outside criteria rather than the internal state of the system. The flashing ratchet studies discussed in previous sections of this chapter are all examples of open-loop control. If information about the state of the system is used as a criteria

for the control of the system, this is referred to as “closed-loop” control. The use of information in the control of noisy systems is relevant to a variety of systems, such as population dynamics [56], economics [57], collective decision making (such as voting) [58, 59], paradoxical games [59–62], and biochemical signaling networks [63].

Feedback control is also of fundamental interest in thermodynamics, exemplified by the famous “Maxwell’s demon” thought experiment proposed by James Clerk Maxwell in 1867 [64–66]. The thought experiment was originally introduced as a challenge to the Second Law of Thermodynamics, which states that the entropy of an isolated system will never decrease [24]. Consider two thermally isolated particle baths, separated by a trapdoor. Suppose that the door is guarded by a “demon”, described by Maxwell as a “being whose faculties are so sharpened that he can follow every molecule in its course.” If the demon chooses to open and close the door in order to allow hot (fast) particles to pass in one direction and cold (slow) particles to pass in the other direction, eventually there will be a cold bath and a hot bath.

On first inspection, this seems to contradict the Second Law of Thermodynamics, because it decreases the entropy of the two baths by sorting the fast moving particles from the slow moving particles without doing mechanical work on the system. However, several mathematical arguments have demonstrated that when the demon is included as part of the isolated system, the increase in entropy that results from monitoring the particles must be greater than the decrease in entropy due to sorting the particles [66]. Although the demon failed to break the Second Law of Thermodynamics, he

has illustrated the potential usefulness and the fundamental limitations of closed-loop control of thermal systems.

It has since been shown that the Second Law of Thermodynamics, when generalized to include a quantified measure of information, sets an absolute minimum on the amount of energy dissipation required in the open-loop control of a physical system [67]. Using information theory [68], it is further demonstrated that each bit of information gathered for closed-loop control can only serve to decrease the entropy of the system by at most one bit of information compared with the reduction in entropy that could be attained for open loop control [67]. This sets a fundamental limit on the improvement in the control of the system (in terms of entropy reduction) that can be gained through closed-loop control.

The flashing ratchet is a well-established model system for the study of directed transport of particles in a noisy environment, as discussed in the previous section. Several recent studies have considered closed-loop control of a flashing ratchet, with the goal of developing a feedback scheme that optimizes the speed of ratchet transport. The study of feedback control in a flashing ratchet provides a conceptually concrete system that can be used to apply and investigate general mathematical predictions for feedback control of dynamic systems.

A strategy for closed-loop control of an overdamped flashing ratchet was recently introduced [69], in which the potential is turned on only if the net force on the particles (and thus the instantaneous center-of-mass velocity) due to the ratchet potential

would be positive, and is turned off if the net force would be negative. This feedback control policy is referred to as the maximization of instantaneous velocity (MIV) strategy.

Although there are no direct mechanical interactions between the particles in this model, this is nonetheless an example of mechanical coupling of the motion of particles in a flashing ratchet. The state of the ratchet (on or off) is determined based on the positions of all the particles, which means that the force on one particle depends on the positions of the other particles. For this reason, the average velocity of ratchet transport for the ensemble of particles depends on the total number of particles. In contrast, the average velocity of non-interacting particles in a flashing ratchet with open-loop control is independent of the number of particles.

For a single particle ($N = 1$), the MIV strategy maximizes not only the *instantaneous* center-of-mass velocity but also the *time-averaged* center-of-mass velocity (v_{cm}) [69], as demonstrated by Brownian dynamics (BD) simulations [70] and analytical solutions to the corresponding Fokker-Planck equations [71–73]. For relatively small ensembles, $N < 10^2 - 10^3$, the feedback control strategy has higher v_{cm} than a periodically flashing ratchet with optimal period, demonstrating that feedback control can improve the performance of the ratchet when the ensemble is small and thermal fluctuations in the net force are significant.

However, for larger ensembles, v_{cm} falls below the optimal flashing ratchet velocity, v_{opt} . In the limit of large N , v_{cm} goes to zero. This is because the average magnitude of

fluctuations in the ensemble-averaged force on particles, $f(t)$, decreases with increasing N . For large N , the average magnitude of $f(t)$ must be very small for a typical fluctuation in $f(t)$ to trigger a change in the potential. This decreases the average velocity by increasing the amount of time spent waiting for fluctuations. This is illustrated in fig. 1.3(a), which shows simulations of the net force and the center-of-mass position as a function of time for $N = 10^6$ particles in a sawtooth flashing ratchet controlled by the MIV feedback strategy. Dashed lines indicate the extended tails of $f(t)$ for large N , as well as the unproductive, plateaus in the corresponding center-of-mass trajectory.

In order to improve upon the performance of the MIV control strategy for large N , Dinis et al. [74] introduced a modified control strategy that eliminates the unproductive, extended tails in $f(t)$. This is accomplished by imposing a rule that the potential is turned on (off) whenever the ensemble-averaged force increases (decreases) through set thresholds. This strategy takes advantage of the fact that the temporal evolution of the system becomes quasi-deterministic for high N . This predictability can be exploited to choose thresholds that impose periodic modulation of the potential without relying on small fluctuations in $f(t)$ to trigger a change of state (see fig. 1.3(b)). The threshold values can be chosen strategically to optimize v_{cm} .

In Craig et al. [18], we introduce an alternate feedback control protocol that yields higher v_{cm} than either the MIV strategy or the threshold strategy for small $N > 1$. This new protocol works by controlling the state of the potential based on

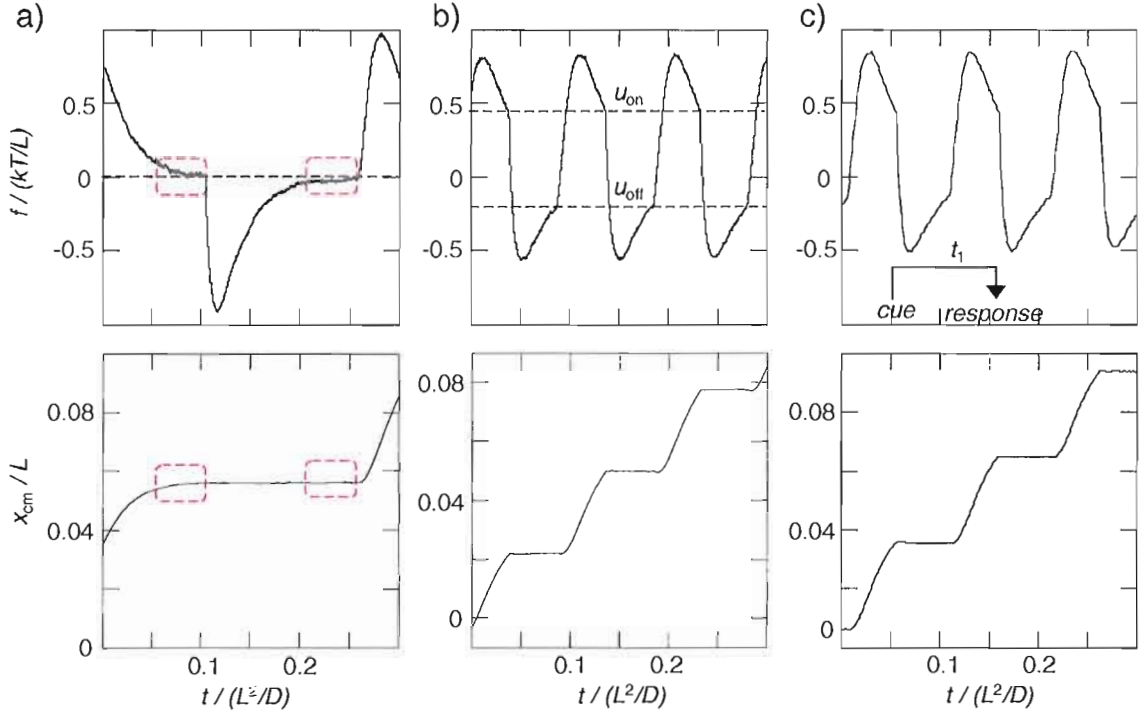


Figure 1.3. Brownian dynamics simulations (appears in Craig et al. [18]). Ensemble-averaged force, f , as a function of time, and the corresponding center-of-mass position, x_{cm} , are displayed to demonstrate the high N ($N = 10^6$) behavior of several feedback control policies for a flashing ratchet with a ‘sawtooth’ potential. Shaded regions indicate when the potential is on, and white regions indicate when the potential is off. (a) Maximization of instantaneous velocity (MIV) strategy [69]. Dashed rectangles indicate the extended tails where unproductive time is spent waiting for a fluctuation in the sign of $f(t)$. (b) Threshold strategy [74]. Dashed lines represent the force thresholds, u_{on} and u_{off} , chosen to optimize the temporal period of oscillation. The potential is turned off whenever the force goes from $f(t) > u_{on}$ to $f(t) < u_{on}$, and is turned on whenever the force goes from $f(t) < u_{off}$ to $f(t) > u_{off}$. (c) MIV strategy with time delayed implementation, which we will discuss in chapter IV.

the complete positional distribution of the particles rather than only the net force on the particles. The goal is to turn the potential on whenever the net displacement of particles is expected to be positive. In the new strategy, which we refer to as the maximization of net displacement (MND) policy, the potential is turned on only for positive values of the estimated displacement, $d(t) = \sum_{i=1}^N (x_i(t) - x_0)$. Here $x_i(t)$ are the particle positions, and x_0 is the estimated average position of particles after equilibrating in the potential. This reference position is chosen in [18] as the mean of a Boltzmann distribution in $V(x)$, and is therefore a function of temperature. Brownian dynamics simulations carried out by Nathan Kuwada demonstrate that the MND strategy produces higher v_{cm} than the MIV strategy for small particle numbers ($N < 4$) in the limit of strong confinement ($V_0 \gg kT$) [18].

The examples above all assume perfect feedback, in which the state of the system is measured with 100% accuracy and feedback control based on this information is implemented instantly. Any real system will not be capable of such idealized implementation of closed-loop control. An experimental realization of feedback control in a flashing ratchet will have inherent limitations such as noise in the measurement and delays due to the finite time required for data collection and processing. Several recent studies have modeled the role of some of these limitations in the performance of the MIV feedback strategy.

For example, Cao et al. [75, 76] modeled feedback control of a flashing ratchet with the MIV strategy, in the case that a “noisy channel” reduces the reliability

of information about the state of the system. By extending the general result that there is a fundamental upper bound on the performance of closed-loop control of dynamical systems [67], they establish that there is an analytical upper bound related to the information content of the channel on the improvement in the power [75] and flux [76] for closed-loop control over open-loop control of a flashing ratchet. This establishes a measure of the performance of the feedback control policy as a function of the information it uses. This result can be used to predict how much improvement in flux and power can be gained by using a closed-loop control policy for an experimental setup if the level of experimental error in tracking the particle positions can be estimated.

In chapter IV, we discuss the MIV feedback control policy in the presence of two experimentally inevitable types of time delay: (1) Implementation delay: A measurement will be implemented after a finite time delay, which arises because of the time required for data processing. (2) Measurement delay: Measurements will be taken at discrete time intervals rather than continuously. This type of delay could be due to the limit in the readout rate of the data acquisition system (for example, a camera that acquires images of the particles). We show that, for a large ensemble, a well-chosen implementation delay increases the average velocity by synchronizing into a quasi-stable periodic mode that takes advantage of the semi-deterministic time evolution of the positional distribution of a large number of particles (fig. 1.3(c)). We study the effect of measurement delay on this synchronized mode. Another recent

study also considers the effect of implementation delay on the MIV feedback policy, producing analytical predictions in agreement with our computational results [77].

Experimental Realization of a Feedback-controlled Flashing Ratchet

The first experimental realization of feedback control of a flashing ratchet has recently been implemented by Benjamin Lopez in the Linke group [51]. A quasi-one-dimensional potential profile is created with a scanning line optical trap [52–55], and tailored potential profiles are created by modulating the intensity of the laser as a function of the position along the scan line. By switching between a sawtooth profile and a flat profile, the steps of a flashing ratchet are realized for a spherical dielectric bead subjected to the optical potential. A total of ten spatial periods of a ratchet potential are created in this experiment, allowing experimental investigation of a small number of beads ($N = 1 - 5$). Feedback control of this system is carried out by switching the potential based on analysis of a photographic image of the bead distribution.

Experimental measurements of flashing ratchet transport confirm several theoretical predictions for a small number of particles: (1) For small N , both the MIV and MND feedback control strategies produce a larger average velocity than a periodic flashing ratchet [18, 69]; (2) The MND strategy, which switches the potential based on estimated net displacement, produces a larger velocity than the MIV strategy for large ratchet potential strength [18].

In chapters III and IV of this dissertation, we make theoretical predictions that are relevant to the performance of this experimental system. In particular, at the end of chapter III, we calculate the effective potential for a finite-sized spherical bead in a one-dimensional sawtooth potential, showing that the asymmetry of the effective potential decreases with bead size. In chapter IV, we theoretically model the role of time delay in feedback control of a flashing ratchet, ending with a discussion of relevant time delays for two distinct experimental systems: the optical trap flashing ratchet described above, and an experimental ratchet system designed to transport a large number of charged particles in a fluid. The theoretical predictions in this dissertation have played a key role in characterizing and discussing the physics of these experimental systems.

Myosin-V: A Biological Molecular Motor

Myosin-V is a biological molecular motor that transports various types of vesicles along actin filaments [78, 79]. In vertebrates, myosin-V transports the endoplasmic reticulum in neurons, and pigment-containing melanosomes in melanocytes. Mutations in myosin-V can cause neurological and pigmentation defects in humans and mice [79].

Myosin-V is a dimeric motor, with two identical motor domains (called “heads”) that each can attach to actin and also serve to hydrolyze ATP hydrolysis (see fig. 1.4). The binding affinity of a head to actin depends on the nucleotide state of the head (in other words, the chemical state corresponding to different stages of the ATP

hydrolysis cycle). A myosin-V head with ADP bound has a high actin affinity, while a head with ATP bound has a low actin affinity, which means that a head will cycle through states of attachment and detachment from actin during the ATP hydrolysis cycle. In order to move significant lengths along a filament, the motor must be able to move forward without completely detaching from actin. Many dimeric motors such as myosin-V, kinesin, and dynein accomplish this by “walking”: The heads take turns detaching from actin while the other head stays attached. Motors that walk in a coordinated manner that allows a long run length before detaching are referred to as “processive.” In contrast, other motors such as muscular myosin II (responsible for muscle contraction) are individually nonprocessive, but work in large assemblies of motors that keep the complex attached to the lattice substrate even when many individual motors have detached [80].

Myosin-V processivity was first demonstrated through optical trap studies [82], in which the motion of actin filaments brought into contact with a myosin-V coated bead was recorded. Shortly thereafter, processive myosin-V transport was also demonstrated through the observation that fluorescently labeled myosin-V molecules can move several microns along an actin filament before detaching [83]. Since then, many research groups have turned their attention to studying myosin-V transport through single molecule mechanical experiments, fluorescent tracking, and other approaches. Its relatively long neck domains ($30nm$ [84, 85]) and large step size ($36nm$, compared with $8nm$ for kinesin) are advantageous for experimental studies that seek high



Figure 1.4. Schematic of mouse myosin-V structure (Source: Sellers et al. [81]). Myosin-V has two motor domains referred to as “heads” (upper, gray) each connected to a neck domain composed of six tandem “IQ motifs” that bind the molecule calmodulin (blue). Two identical monomers (a head and adjacent neck domain) dimerize through a coiled-coil helix. The molecule ends in a globular tail domain (lower, gray) that binds to cargo. The length of each neck domain is approximately $30nm$.

resolution information about the stepping process. For this reason, a great deal of progress has been made in recent years toward characterizing the myosin-V stepping mechanism [86, 87].

Several experimental studies have used total internal reflection fluorescence (TIRF) microscopy to demonstrate the important result that myosin-V walks in a *hand-over-hand* fashion, in which the two heads alternate between the trailing and leading positions (illustrated schematically in fig. 1.5). The first evidence for hand-over-hand stepping came from an experiment by Yildiz et al. [2], in which a myosin-V molecule with a green fluorescent protein (GFP) fused to one of the heads was monitored as it walked along an immobilized actin filament. The motion of the GFP-labeled

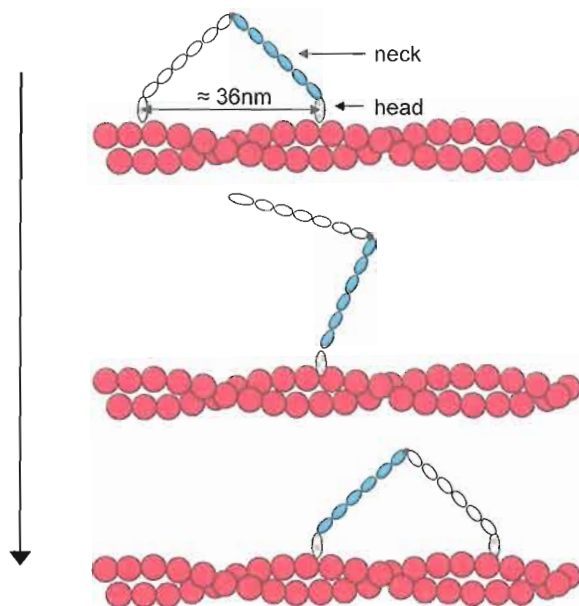


Figure 1.5. Hand-over-hand stepping. Illustrative schematic of the hand-over-hand transport described in the text. Myosin-V walks in a hand-over-hand manner, in which the binding domains (heads) alternate between the trailing and the leading position. The cartoon images of myosin-V in this schematic illustrate a hand-over-hand step, where the progression of images from top to bottom indicates the motion of the molecule with passing time during the step.

head was consistent with hand-over-hand transport in which the trailing head moves forward about 72nm to become the new leading head, and then stays attached while the other heads repeats the cycle, thus producing steps which move the center of the molecule forward by 36nm . Further evidence for hand-over-hand stepping was gained by labeling the two heads of myosin-V with different color fluorophores, which allowed visualization of the alternate stepping [88, 89].

Experimental evidence suggests that myosin-V is likely to walk along one side of the actin filament rather than walking around the filament in a spiral. An experiment in which an actin filament was scanned back and forth past a myosin-V monomer

demonstrated that myosin-V has high binding affinity to actin at $36nm$ intervals along the filament [85], which is equal to the helical pseudo-repeat distance of an actin filament (see fig. 1.5). Myosin-V has long enough neck domains to allow it to bind with a $36nm$ horizontal separation between heads. The small variation in the step size may indicate that there is resistance in the molecule to azimuthal distortion, making it more likely to walk along on one side of the actin filament as illustrated in fig. 1.5. The propensity to walk in a straight line rather than spiraling could prove useful for navigating a crowded cellular environment.

Now that the hand-over-hand stepping mechanism is established, investigation of myosin-V transport is often motivated by the following questions: (1) How does the trailing head become the leading head? In other words, how do micron-sized conformational changes of the heads during the ATP hydrolysis cycle couple to $36nm$ steps? (2) How is the stepping coordinated? In other words, how does the leading head “know” to stay attached until it becomes the trailing head?

Many experiments have addressed these questions, producing pieces of the puzzle that are collectively beginning to form a picture of the myosin-V stepping process. Below, we discuss some key experimental findings:

Question (1): How does the trailing head become the leading head?

As discussed above, Myosin-V walks along actin in a hand-over-hand fashion with a $36nm$ step size [2, 82, 85, 88–96]. The underlying physical mechanism for these steps remains an area of open investigation. Myosin-V spends most of its time with

both heads bound to actin, and a step takes place very quickly, lasting about $10^{-3}s$, compared with about $10^{-1}s$ for the entire cycle [97]. As new measurement techniques are developed, single molecule experimental assays are beginning to produce data with high enough resolution to learn about the dynamics of the short-lived, one-head-bound intermediate.

A number of recent experimental studies have suggested the following hypothetical explanation for the stepping mechanism (illustrated schematically in fig. 1.6): After detachment of the trailing head from actin, relaxation of strain in the leading neck domain produces a new equilibrium conformation such that the center-of-mass position moves forward on average (in the $+x$ -direction in fig. 1.6). The detached head undergoes a tethered diffusional search for a new binding site, which is biased toward sites in the $+x$ -direction with respect to the attached head. The computational model for myosin-V that will be presented in chapter V of this dissertation establishes an approach to quantitatively test the mechanical feasibility of this hypothetical stepping mechanism. Below, we discuss some experimental support for this hypothetical mechanism, which we will refer to as the “biased tethered diffusion” model.

A recent single-molecule experiment by Cappello et al. [98] lends strong support to the biased tethered diffusion model for the myosin-V stepping mechanism. They used a newly-developed optical method called traveling wave packet tracking (TWT) to obtain high resolution information about the motion of a $200nm$ polystyrene bead attached to the cargo domain of a myosin-V molecule as it walked along an actin

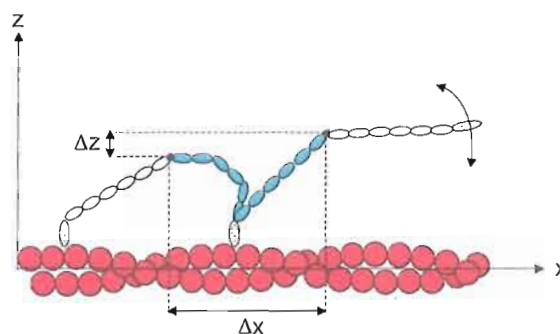


Figure 1.6. Schematic of hypothetical stepping mechanism of myosin-V (see text). Several experimental studies support a “biased diffusional search” model for the mechanics of the myosin-V step. According to this model, relaxation of the leading neck domain after detachment of the trailing head results in a displacement (Δx above) of the equilibrium position of the neck domain juncture parallel to the filament (in the $+x$ -direction in the schematic). The corresponding motion away from the filament (in the z -direction) is labeled as Δz .

filament. In general, TWT can track the motion of a bead in two dimensions through detection of an optically scattered wavepulse [99]. In the experiment by Cappello et al., TWT measurements were used to track the motion of a bead attached to myosin-V in the direction parallel to the actin filament (in the x -direction in fig. 1.6)) and perpendicular to the filament (in the z -axis in fig. 1.6)). They used a classical optical tweezers assay in which a stationary optical trap holds the bead in contact with an actin filament. As the motor walks along the filament away from the focus of the trap, it experiences a load force approximately proportional to its distance from the center of the trap.

Some key observations and results gained from the experiment by Cappello et al. include: **(1) Stall force measurement:** The stall force is defined as the maximum opposing force that can be applied to the motor before it can no longer step forward.

In this experiment, the motor was observed to step processively until the opposing load from the optical trap exceeded approximately $1.5 - 3pN$ (a value that varied for different processive runs), after which the motor stalled. **(2) Large variation in features of individual steps:** A large amount of variation is observed from one step to the next, in terms of the noisiness of the spatial trajectory and the amount of time it takes to complete the step. **(3) Features of the step average support the “biased tethered diffusion” model:** To discern general features, they reduced the signal to noise ratio by averaging about 200 steps together, using a quantitative fitting method to identify and synchronize the steps. The step average for the x-component of the bead’s motion has the following two characteristic phases (see fig. 1.7(a)): a fast ($160\mu s$) phase in which the center-of-mass moves forward $23 - 25nm$, and a slower ($\approx 1ms$) phase in which the center of mass moves the remaining distance parallel to the filament to complete the $36nm$ step. This two-phase step average in the x -direction is consistent with other single-molecule experiments that obtain step averages in the direction along the actin filament [84, 85, 100–102]. The step average for the z -component of the bead’s motion shows a $6nm$ movement away from the filament that takes place at the same time as the first characteristic phase of the step average in the x -direction (fig. 1.7(b)). These characteristic phases of the step average are interpreted in terms of the biased tethered diffusion model illustrated in fig. 1.6, suggesting that the displacement in the equilibrium position of the neck domain juncture after the trailing head detaches is $\Delta x \approx 23 - 25nm$ in the x -direction

and $\Delta z \approx 6nm$ in the z-direction. The slower 11 – 16nm phase of the step average in the x -direction presumably corresponds to the average over the diffusional search and reattachment for widely varying dynamics of individual steps.

The biased diffusional search model is also supported by electron microscopy (EM) images [103] and atomic force microscopy (AFM) measurements [104] that demonstrate that the neck domain of myosin-V has a preferred attachment angle that depends on the nucleotide state of the head. These studies report an average forward rotation of the neck domain when phosphate is released, such that an ADP-bound head attached to actin is likely to have a forward-leaning neck domain with respect to the actin filament in the direction of motility. If intramolecular strain during the two-heads-bound stage of the stepping cycle prevents this forward-leaning conformation from being fully realized for the the leading head, then release of strain following trailing head detachment could account for the average motion observed during the first phase of the step average. A forward tilt of the neck domain during the one-head-bound state would bias the diffusional search of the free head by positioning it near an available binding site in the forward direction.

Further support for the biased diffusional search model is provided by two recent experiments that tracked the motion of the detached head during the one-head-bound intermediate of the myosin-V stepping cycle [100, 105]. Dunn et al. [100] labeled one of the neck domains of myosin-V with a 40nm gold nanoparticle near the head (fig. 1.8(a)). They used sub-millisecond dark-field imaging to measure light scattered

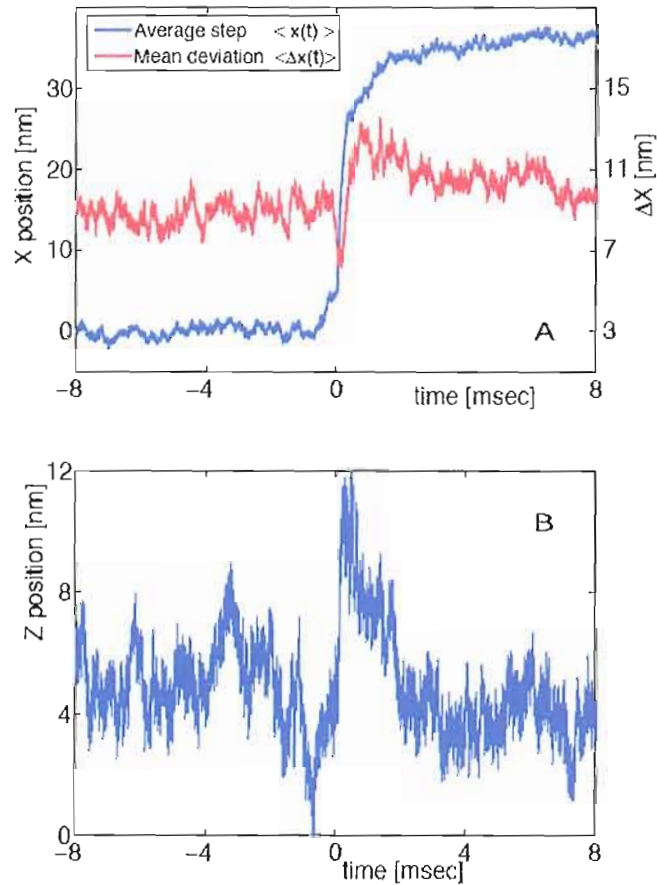


Figure 1.7. Average of experimental step trajectory for myosin-V. Experimental data from Cappello et al. [98], demonstrating a sequence of coupled motion in two directions of a 200nm bead attached to the myosin-V cargo domain, observed through traveling wave tracking (TWT). (a) The average over about 200 steps in the x-direction (parallel to actin), demonstrating a fast $\approx 25\text{nm}$ phase followed by a slower $\approx 5\text{nm}$ phase (see text). (b) The corresponding average motion in the z-direction (perpendicular to the filament), indicating that the bead moves away from the filament on average by about 6nm at the beginning of the step and returns to the original vertical position during the second phase of the step average.

from the nanoparticle in order to track the three-dimensional motion of the head during a processive run. A step-finding algorithm based on the displacement and variance in the data was used to identify the one-head-bound intermediate of the myosin-V cycle. The positional variance during the one-head-bound substeps was consistent with free rotation of the detached head about the junction between neck domains. The authors make the observation that free rotation of the detached head not only agrees with their data, but is a reasonable structural assumption that requires a short, unconstrained peptide linker at the juncture between neck domains to act as a swivel.

A second recent experiment also provides evidence for free rotation of the detached head about the junction between neck domains (Shiroguchi et al. [105]). In this case, a micron-sized fluorescently labeled microtubule segment was attached to one of the neck domains in order to track the motion of the neck (fig. 1.8(b)). By analyzing images of the microtubule during substeps, they conclude that the leading head rotates forward unidirectionally at the beginning of the step, and the detached trailing head undergoes Brownian rotation before reattaching to actin. Additional experimental support for the free rotation of the detached head about the neck domain juncture exists in the form of electron microscopy photos of myosin-V [103], which exhibit a large distribution of rotational angles for the detached neck domain.

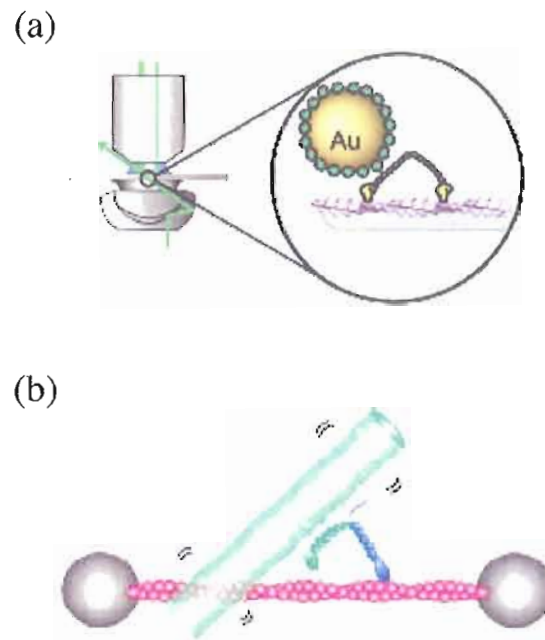


Figure 1.8. Experimental observations of tethered diffusion. Schematics from [100, 105] of experiments that measure the motion of a detached head and neck domain of myosin-V: (a) Dunn et al. [100] tracked the motion of a detached head by measuring light scattered from a gold nanometer particle attached to a known position on the neck domain. (b) Shiroguchi et al. [105] track the motion of the detached neck domain by monitoring a fluorescently labeled microtubule filament that is attached to the neck domain. Both experiments conclude that the motion is consistent with a model in which the detached neck domain rotates freely about the juncture between neck domains.

Question (2): How is myosin-V stepping coordinated?

As mentioned above, another open area of investigation for myosin-V is to determine the mechanism of coordination between the two heads underlying the experimentally observed processive, hand-over-hand transport. Some type of coordination between the detachment cycles of the two heads is needed to explain the large number of steps myosin-V takes along actin before detaching. An individual myosin-V head is estimated to spend approximately 70% of its time strongly attached to actin [106], based on rate constants measured for a single-headed fragment of myosin-V. In Viegel et al. [85], a simple model that treats the biochemical cycle for a head as two states (attached and detached) predicts that if the cycles of the individual heads are independent from each other, and each is attached to actin 70% of the time, myosin-V will take eight steps on average before detaching. However, the average run length observed experimentally is higher (20-60 steps on average) [2, 91–93, 95, 96, 107–109].

Recent experimental evidence supports the idea that the activity of the two myosin-V heads is coordinated through intramolecular strain [85, 109–111]. Because myosin-V spends the majority of its chemical cycle with both heads bound to ADP and actin [106], and ADP release is sensitive to strain applied to the end of the neck domain [85, 110], the prevailing model for coordination of the steps of myosin-V is that strain-dependent ADP release keeps the detachment cycles of the two heads out of phase. Although there is currently no consensus about how myosin-V steps are coordinated, there is a lot of support for the hypothetical explanation that strain-

dependent ADP release makes the trailing head more likely to detach from actin than the leading head through one (or both) of the following two mechanisms [111]: (1) A forward-directed strain on the trailing head increases the rate of ADP release from this head, thus increasing the likelihood for the trailing head to detach first. (2) A rearward strain on the leading head inhibits ADP release from this head, making it less likely to detach. Either of these mechanisms could increase the run length by keeping the heads out of phase from one another, so that they are unlikely to both detach at the same time. Below, we discuss several experimental studies that support the model that stepping is coordinated through strain-dependent gating of ADP release.

The idea that the two heads of myosin-V could “communicate” with each other through intramolecular strain is bolstered by experimental observations that suggest that when both heads are attached to actin, the motor spends much of its time in a strained conformation. Longitudinal strain between the two heads along the direction of actin filaments is evident in EM images of the motor conformation with two heads bound to actin [103, 112]. Furthermore, the discrepancy between measured “stroke length” ($\approx 25nm$) and the myosin-V step size ($36nm$) could indicate that myosin-V spends much of the two-heads-bound phase of the cycle in a strained conformation.

Several experiments in recent years have demonstrated that the rate of ADP release from a head (which is the rate-limiting process in the detachment of the head from actin) can be altered by applying a force to the end of the adjacent

neck domain. Veigel et al. [85] measure a decrease in the ADP release rate from a myosin-V monomer in the presence of rearward force applied to the neck domain, as well as a modest acceleration of ADP release in the presence of a forward directed force. Purcell et al. [110] also measure a slowed rate of ADP release from a myosin-V monomer with rearward load applied to the neck domain, but do not detect a significant force dependence in ADP release rate in the presence of force applied in the forward direction. Further evidence for head-head coordination through asymmetric ADP release rates is provided by an experiment in which ADP release rates were measured from both actin-bound heads of a myosin-V dimer (Rosenfeld et al. [113]). Measurements from this experiment indicated an approximately 50-fold decrease of the ADP release rate from the leading head, and a two- to three-fold increase in the ADP release rate from the trailing head, compared with the ADP release rate measured for a single-headed myosin-V molecule.

Although the bulk of experimental evidence supports the model that the detachment cycles of the heads are coordinated through strain-dependent ADP release, the physical mechanism by which intramolecular strain gives rise to asymmetric ADP release is not well understood. One of the goals of the mechanical model for myosin-V presented in chapter V is to develop an experimentally motivated physical model for how ADP release is affected by the conformation of the molecule. This, in turn, will allow us to make testable predictions about how the mechanical properties of the motor impact the level of coordination.

As summarized above, the study of the myosin-V walking mechanism is a data-rich field, and a general idea of the physical mechanism of stepping is beginning to emerge. Quantitative modeling has the potential to contribute to this understanding by testing proposed mechanisms and making experimentally testable predictions.

CHAPTER II

MOLECULAR DYNAMICS SIMULATION METHODS

Molecular dynamics (MD) is a computational method designed to simulate the time-dependent behavior of a molecular system based on a finite difference approach: Given the positions and velocities of the particles at time t , an approximation is made for these quantities at time $t + \delta t$, where δt is a discrete time interval chosen to be very small compared to the time-scale of the dynamics of interest for the system. Molecular dynamics simulations are based on classical mechanics, traditionally using Newton's second law ($\mathbf{F} = m\mathbf{a}$) to govern the evolution of the system. Several integration algorithms have been developed for updating the position and velocity of particles at discrete time intervals [70]. All of these algorithms assume that the position, velocity, and acceleration can be approximated by Taylor expansions:

$$\mathbf{r}(t + \delta t) = \mathbf{r}(t) + \mathbf{v}(t)\delta t + \frac{1}{2}\mathbf{a}(t)\delta t^2 + \dots \quad (2.1)$$

$$\mathbf{v}(t + \delta t) = \mathbf{v}(t) + \mathbf{a}(t)\delta t + \frac{1}{2}\mathbf{b}(t)\delta t^2 + \dots \quad (2.2)$$

$$\mathbf{a}(t + \delta t) = \mathbf{a}(t) + \mathbf{b}(t)\delta t + \dots \quad (2.3)$$

In this chapter, we will give some general background about molecular dynamics simulation methods. Then, we will discuss molecular dynamics simulations with an implicit solvent, based on the Langevin equation. Finally, we discuss the specific methods used for the simulations presented in each chapter of this dissertation, and present the general layout of the computer programs that were used to carry out these simulations.

Basic Verlet Algorithm

The Verlet algorithm is a common integration method that uses the position and acceleration at time t to calculate the position at time $t + \delta t$. It is derived by considering the following two Taylor expansions about $\mathbf{r}(t)$:

$$\mathbf{r}(t + \delta t) = \mathbf{r}(t) + \mathbf{v}(t)\delta t + \frac{1}{2}\mathbf{a}(t)\delta t^2 \quad (2.4)$$

$$\mathbf{r}(t - \delta t) = \mathbf{r}(t) - \mathbf{v}(t)\delta t + \frac{1}{2}\mathbf{a}(t)\delta t^2 \quad (2.5)$$

Adding equations 2.4 and 2.5 together yields:

$$\mathbf{r}(t + \delta t) = 2\mathbf{r}(t) - \mathbf{r}(t - \delta t) + \mathbf{a}(t)\delta t^2 \quad (2.6)$$

Molecular dynamics simulations can be carried out by updating the position at discrete time intervals using equation 2.6. The advantage of using equation 2.6 instead of equation 2.4 to update the position is that equation 2.6 has error on the order of δt^4 (since terms of order δt^3 would cancel out when the two Taylor expansions are added together), while equation 2.4 has error on the order δt^3 . This algorithm does not explicitly use the velocity of the particles in the calculation, but the velocity at time t can be approximated in the following way:

$$\mathbf{v}(t) = \frac{\mathbf{r}(t + \delta t) - \mathbf{r}(t - \delta t)}{2\delta t} \quad (2.7)$$

This is a popular algorithm because it is straight-forward to program and computationally compact. However, a disadvantage to this algorithm is that it lacks a high level of precision. The position (eq. 2.6) has an error on the order of δt^4 , while the velocity (eq. 2.7) has a larger error on the order of δt^2 .

Leapfrog Algorithm

Several modified algorithms improve upon the accuracy of the basic Verlet algorithm. An example is the Leapfrog algorithm, in which the position at time $t + \delta t$ is calculated based on $\mathbf{r}(t)$, $\mathbf{a}(t)$, and $\mathbf{v}\left(t + \frac{1}{2}\delta t\right)$, as follows:

$$\mathbf{r}(t + \delta t) = \mathbf{r}(t) + \mathbf{v}\left(t + \frac{1}{2}\delta t\right) \delta t \quad (2.8)$$

$$\mathbf{v}\left(t + \frac{1}{2}\delta t\right) = \mathbf{v}\left(t - \frac{1}{2}\delta t\right) + \mathbf{a}(t)\delta t \quad (2.9)$$

This is referred to as a Leapfrog algorithm because the velocity is calculated at time $t + \frac{1}{2}\delta t$ (i.e., the velocity “leaps” ahead of the position), and then $\mathbf{v}\left(t + \frac{1}{2}\delta t\right)$ is used to calculate the position at time $t + \delta t$ (i.e., the position “leaps” ahead of the velocity). The velocity at time t can be calculated as

$$\mathbf{v}(t) = \frac{1}{2} \left[\mathbf{v}\left(t - \frac{1}{2}\delta t\right) + \mathbf{v}\left(t + \frac{1}{2}\delta t\right) \right]. \quad (2.10)$$

It can be demonstrated that this method is algebraically equivalent to the basic Verlet algorithm [70]. A computational advantage to this approach is that values of the velocity are calculated explicitly during the time step (although not for the same time value as the position). The calculated value of $\mathbf{v}(t)$ is more accurate for the Leapfrog algorithm (eq. 2.10) than for the basic Verlet algorithm (eq. 2.7), because eq. 2.7 subtracts two large quantities (the position at discrete times) to obtain a small quantity (the displacement), which introduces computational roundoff error. An accurate estimate of $\mathbf{v}(t)$ is useful for evaluating the kinetic energy of the system at time t .

Langevin Dynamics: Molecular Dynamics With an Implicit Solvent

The Langevin equation is a stochastic differential equation that describes the dynamics of a particle in a viscous solvent. For a coordinate \mathbf{r} , the general form of the Langevin equation is:

$$\mathbf{F}(\mathbf{r}) = m\ddot{\mathbf{r}} = -\gamma\dot{\mathbf{r}} - \nabla U(\mathbf{r}) + \xi(t) \quad (2.11)$$

where $F(\mathbf{r})$ is the total force felt by the particle, m and γ are the mass and drag coefficient of the particle, and $U(\mathbf{r})$ is the potential energy corresponding to internal and external forces. The force on the particle due to collisions with the fluid is represented by a randomly distributed Gaussian white noise term, $\xi(t)$, with zero mean and a standard Gaussian correlation $\langle \xi_i(t)\xi_j(s) \rangle = 2\gamma kT \delta_{ij} \delta(t-s)$, where i and j represent different directional components. Equation 2.11 can be used to simulate the viscous aspects of the solvent, but it does not include hydrodynamic interactions.

Molecular dynamics simulations based on the Langevin equation are often referred to as Brownian dynamics (BD). The position and velocity can be updated according to the following Verlet algorithm variation [114, 115]:

$$\mathbf{r}(t + \delta t) = \mathbf{r}(t) + c_1 \mathbf{v}(t) \delta t + c_2 \mathbf{a}(t) \delta t^2 + \delta \mathbf{r}^G \quad (2.12)$$

$$\mathbf{v}(t + \delta t) = c_0 \mathbf{v}(t) + (c_1 - c_2) \mathbf{a}(t) \delta t + c_2 \mathbf{a}(t + \delta t) \delta t + \delta \mathbf{v}^G \quad (2.13)$$

The coefficients, c_0 , c_1 , and c_2 are defined as:

$$c_0 = e^{-\gamma\delta t} \quad (2.14)$$

$$c_1 = \frac{1 - c_0}{\gamma\delta t} \quad (2.15)$$

$$c_2 = 1 - c_1\gamma\delta t \quad (2.16)$$

The terms $\delta\mathbf{r}^G$ and $\delta\mathbf{v}^G$ in equations 2.12 and 2.13 are random numbers from a Gaussian distribution, with zero mean ($\langle\delta\mathbf{r}^G\rangle = 0$ and $\langle\delta\mathbf{v}^G\rangle = 0$) and correlation $\langle(\delta\mathbf{r}^G)^2\rangle = c_{11}$, $\langle(\delta\mathbf{v}^G)^2\rangle = c_{22}$, and $\langle\delta\mathbf{r}^G\delta\mathbf{v}^G\rangle = c_{12}$. The correlation values, c_{11} , c_{22} and c_{12} are elements of a matrix, \mathbf{C} , for correlated, Gaussian-distributed random numbers, given by:

$$\rho(\mathbf{x}) = \frac{1}{|\mathbf{C}|2\pi} e^{-\frac{\mathbf{x}^T \cdot \mathbf{C}^{-1} \cdot \mathbf{x}}{2}} \quad (2.17)$$

It can be shown [70] that the individual elements of the matrix \mathbf{C} are:

$$c_{11} = \frac{kT(\delta t)^2}{m} \left[2 - \frac{1}{\gamma\delta t} (3 - 4e^{-\gamma\delta t} + e^{-2\gamma\delta t}) \right] \quad (2.18)$$

$$c_{22} = \frac{kT}{m} [1 - e^{2\gamma\delta t}] \quad (2.19)$$

$$c_{12} = \frac{kT}{m\gamma} [1 - e^{-\gamma\delta t}]^2 \quad (2.20)$$

For any particle, each spatial component of $\delta\mathbf{r}^G$ is correlated with the same component of $\delta\mathbf{v}^G$, because they are each related to the same random process over the same time interval. The random variables for separate particles and separate degrees of freedom are sampled independently.

Overdamped Langevin Dynamics

Molecular dynamics simulations that update the position and velocity of particles according to equations 2.12 and 2.13 are accurate over the span of damping regimes, from the ballistic, underdamped regime (high m , low γ), to the overdamped regime (low m , high γ) where inertial forces are negligible on the time scale of interest. However, simulations in the overdamped regime can be considerably simplified. In the overdamped limit ($(\gamma/m)\delta t \rightarrow \infty$), it can be assumed that no acceleration takes place on average. The dynamics of the system can be described by the overdamped Langevin equation:

$$\mathbf{F}(\mathbf{r}) = 0 = -\gamma\dot{\mathbf{r}} - \nabla U(\mathbf{r}) + \xi(t) \quad (2.21)$$

The position of each particle can be integrated according to:

$$\mathbf{r}(t + \delta t) = \mathbf{r}(t) + \mathbf{v}(t)\delta t + \delta\mathbf{r}^G \quad (2.22)$$

where $\mathbf{v}(t) = \mathbf{F}(t)/\gamma$. The position and velocity are not correlated in the overdamped limit, which means that molecular dynamics simulations can be carried out by updating the position at discrete intervals, and a separate calculation for $\mathbf{v}(t + \delta t)$ is no longer necessary.

Organization of Simulation Programs

In chapter III, we simulate the motion of mechanically coupled particles in a flashing ratchet. We integrate the position and velocity for each particle according to equations 2.12 and 2.13, using a computer program in Fortran 77. The use of equations 2.12 and 2.13, which are based on the general Langevin equation (eq. 2.11), means that the program for this model is completely general and could be applied to different damping regimes, although in chapter III the application is for an overdamped system. A single time step of this integration is carried out in the following way:

- Generate correlated random numbers, ξ , for each particle, i , in each direction.

- Update the position for each particle $(x(i), y(i), z(i))$:

$$x(i) = x(i) + c_1 * v_x(i) * dt + c_2 * f_x(i) * (dt)^2 + \xi_x(i), \text{ etc.}$$

- Partially update the velocity of each particle $(v_x(i), v_y(i), v_z(i))$:

$$v_x(i) = c_0 * v_x(i) + (c_1 - c_2) * f_x(i) * dt, \text{ etc.}$$

- Update the force on each particle $(f_x(i), f_y(i), f_z(i))$.

- Finish updating the velocity:

$$v_x(i) = v_x(i) + c_2 * f_x(i) * dt * \xi_{v_x}(i), \text{ etc.}$$

- Update program time.

In chapters IV and V, we simulate models of systems that operate in the overdamped limit. In chapter IV, we study the effect of time delay on a feedback control mechanism for a flashing ratchet in the completely overdamped limit. In chapter V, we present a mechanical model for the walking mechanism of the biomolecular motor, myosin-V. Because of their small molecular mass, biological molecular motors operate in the overdamped limit [9]. The simulations presented in chapters IV and V were calculated by updating the positions of the particles according to equation 2.22. Each time step is carried out in the following way:

- Generate correlated random numbers, ξ , for each particle, i , in each direction.
- Update the position for each particle $(x(i), y(i), z(i))$:

$$x(i) = x(i) + (f_x(i)/\gamma) * dt + \xi_x(i), \text{ etc.}$$

- Update the force on each particle $(f_x(i), f_y(i), f_z(i))$.
- Update program time.

For all simulations, the force is calculated during each time step according to $f_x(i) = -\frac{\partial U(i)}{\partial x}$, $f_y(i) = -\frac{\partial U(i)}{\partial y}$, $f_z(i) = -\frac{\partial U(i)}{\partial z}$, where $f_x(i)$, $f_y(i)$, and $f_z(i)$ are

the x , y , and z components of the force on particle 'i'. The total potential, $U(i)$, experienced by each particle is defined specifically for each model. For example, particles in a flashing ratchet potential, $V(x)$, experience a total potential $U(x, y, z)$ that is the sum of the external ratchet potential and the potentials that define inter-particle interactions. The specific interaction potentials for each model are discussed in the chapter where the model is presented.

CHAPTER III

COUPLED MOTION IN A BROWNIAN RATCHET

Introduction

As discussed in chapter I, the first studies of the flashing ratchet concept demonstrated net transport of point-like particles in a piecewise linear ‘sawtooth’ potential. However, recent interest in ratchet transport of objects that have internal structure has been motivated by the possibility of developing a novel approach to sorting objects with different properties, and the goal of making the analogy between the flashing ratchet and biological molecular motors more realistic.

In this chapter, we investigate the effects of coupled motion in a Brownian ratchet using a rigid chain of evenly spaced particles. The chapter begins with the simplest example of mechanical coupling between particles, considering rigidly connected chains of particles in a completely one-dimensional system. Next, the role of coupled motion for a rigid rod of evenly spaced particles in a three-dimensional system is discussed. Finally, the role of the finite size of non-interacting beads in a ratchet is discussed in the context of an experimental ratchet system that another student has developed to investigate the motion of spherical beads in a quasi-one-dimensional flashing ratchet.

Model

In order to simulate a chain of evenly-spaced particles, a combination of attractive and repulsive forces between adjacent particles is used to establish a fixed separation. Specifically, this is accomplished with a repulsive Lennard-Jones interaction

$$V_{ij}(r_{ij}) = \begin{cases} 4\epsilon \left(\left(\frac{\sigma}{r_{ij}}\right)^{12} - \left(\frac{\sigma}{r_{ij}}\right)^6 \right) + \epsilon & : r_{ij} \leq 2^{\frac{1}{6}}\sigma \\ 0 & : r_{ij} > 2^{\frac{1}{6}}\sigma \end{cases}, \quad (3.1)$$

where r_{ij} is the separation between particles, and a finite extensible nonlinear elastic (FENE) potential between adjacent particles

$$U(r_{ij}) = -\frac{1}{2}k_{\text{F}}R_0^2 \ln \left(1 - \frac{r_{ij}^2}{R_0^2} \right). \quad (3.2)$$

The distance between adjacent particles, d , is determined by the choice of the parameters R_0 and σ .

The ratchet potential is defined as a piecewise linear sawtooth potential (fig. 3.1) with asymmetry, a , potential depth, V_0 , and periodic length, L . The potential alternates between ‘on’ and ‘off’ for time periods t_{on} and t_{off} , respectively.

The motion of each particle is given by the Langevin equation as described in chapter II:

$$m\ddot{\mathbf{r}}_i = -\gamma_b\dot{\mathbf{r}}_i + \xi(t) - \nabla V(\mathbf{r}_i), \quad (3.3)$$

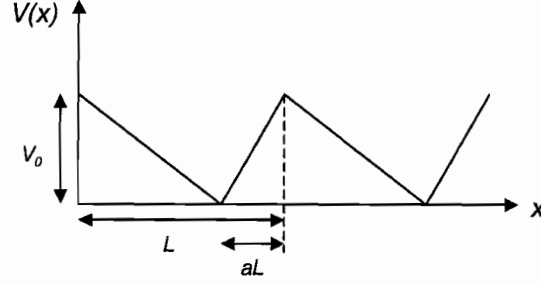


Figure 3.1. Sawtooth ratchet potential. The applied ratchet potential $V(x)$ is characterized by periodic length L , height V_0 , and asymmetry a .

where $\xi(t)$ is a randomly fluctuating Gaussian white noise term with zero mean and correlation $\langle \xi(t)\xi(s) \rangle = 2\gamma_b kT \delta(t-s)$, γ_b is the drag coefficient of a particle, m is the mass of a particle, k is the Boltzmann constant and T is the temperature of the heat bath. The term $\nabla V(\mathbf{r}_i)$ represents the sum of forces on particle ‘i’, including the intramolecular forces resulting from the Lennard-Jones potential (eq. 3.1) and the FENE potential (eq. 3.2), and the external force due to the ratchet potential.

In this chapter, scaled units of length, energy and time, respectively, are defined as: $\sigma = 1$, $\epsilon = 1$, and $\tau = \sqrt{\frac{m\sigma^2}{\epsilon}} = 1$. Unless otherwise noted, the following input parameters are used: $L = 5\sigma$, $kT = \epsilon$, $t_{on} = t_{off} = 20\tau$, and $d = 0.97\sigma$. Different values of the separation distance d are simulated by tuning the FENE parameter R_0 . When kT/ϵ is varied to study temperature dependence, R_0 is re-calibrated for each kT , such that the mean particle separation remains the same.

In order to study the role of the extended geometry of a chain of particles, without compounding this with the effect of varying the total diffusion constant, the total drag coefficient is held constant for all chains. In practice, this is accomplished by setting

the drag coefficient of an individual particle to $\gamma_b = 1/N$, where N is the total number of particles in the chain. Because hydrodynamics effects have not been included, this gives a total drag coefficient: $\gamma_T = N\gamma_b = 1$ [116].

Coupled Motion in Low-temperature Regime

In a one-dimensional system, it is straight-forward to predict the direction of transport of an object in a flashing ratchet based on the geometry of the potential. For instance, in the low temperature limit ($kT \ll V_0$), the mean position for a distribution of non-interacting point particles within a spatial period of a sawtooth potential (fig. 3.1) is the potential minimum: $x_{min} = (1 - a)L$. During the ‘off’ phase of the ratchet cycle, a particle must diffuse at least $\Delta x_+ = aL$ in the +x-direction to be trapped one well forward when the potential turns back on. It must diffuse at least $\Delta x_- = (1 - a)L$ in the -x-direction to be trapped one well backward when the potential turns on. The time-averaged velocity, $\langle \dot{x} \rangle$, for non-interacting point particles in a flashing ratchet will therefore be positive for all $aL < (1 - a)L$, which gives $\langle \dot{x} \rangle > 0$ for all $a < 1/2$.

For a ratchet potential of arbitrary shape, the direction of the average velocity can be determined by the mean of the particle distribution during t_{on} : The average velocity is positive, $\langle \dot{x} \rangle > 0$, for all $\Delta x_+ < \Delta x_-$. The condition $\Delta x_+ = \Delta x_-$ gives a critical point in parameter space about which the direction of velocity will reverse. In general, the critical condition, $\Delta x_+ = \Delta x_-$, depends on the asymmetry of the

potential, the geometry of the object being transported, and the temperature of the bath (because the mean position shifts away from the minimum of an asymmetric potential with increasing temperature). A reversal in the direction of velocity can result from tuning any of these parameters. Because the behavior of the system is antisymmetric about $a = 1/2$, we limit our discussion to the range $0 < a < 1/2$:

For a one-dimensional chain of particles in the low-temperature limit ($kT \ll V_0$), the characteristic diffusion distances, Δx_+ and Δx_- , can be visualized by considering the effective potential, $U(x_{cm})$, given by:

$$U(x_{cm}) = \frac{1}{N} \sum_{i=1}^N V(x_i). \quad (3.4)$$

The simplest case to consider is a dimer (two particles at a fixed distance). If $d < aL$, the dimer will localize with a mean center-of-mass position to the left of the minimum of $V(x)$, so that neither particle resides on the steep slope (fig. 3.2(a)). For this reason, the effective potential has a minimum at $x_{min} = x_{cm} = (1 - a)L - d/2$. During t_{off} intervals, the dimer must diffuse at least far enough that both particles are in the adjacent well in the +x-direction (i.e., $x_{cm} \geq L + d/2$) to be trapped one well forward when the potential turns back on. This gives a characteristic diffusion distance: $\Delta x_+ = aL + d$. On the other hand, a dimer only needs to diffuse far enough that one particle is in the adjacent well in the -x-direction (i.e., $x_{cm} \leq d/2$) for the dimer to be trapped one well backward when the potential turns on. This yields: $\Delta x_- = (1 - a)L - d$. Solving the critical condition, $\Delta x_+ = \Delta x_-$, for a yields the

following expression for the critical asymmetry, a_c , at which the velocity will reverse directions for a given value of d :

$$a_c = \frac{1}{2} - \frac{d}{L}. \quad (3.5)$$

Eq. 3.5 was obtained by assuming that $d < aL$, and therefore is valid for $d/L < a_c = 1/2 - d/L$, or $d/L < 1/4$.

Analytical predictions of the direction of transport are slightly less intuitive when the length of the dimer is greater than the steep slope of $V(x)$ ($d > aL$), because it is also possible for the dimer to localize during t_{on} such that it straddles a potential maximum of $V(x)$ with one particle in each well (fig. 3.2(b)). For this reason, the effective potential has two local minima: $x_{min1} = (1 - a)L - d/L$ and $x_{min2} = (1 - a)L + d/2$. The average localization position is a superposition of these two minima: $\langle x_{min} \rangle = \Phi x_{min1} + (1 - \Phi)x_{min2} = (1 - a)L + (1 - 2\Phi)d/2$, where $\Phi \left(a, \frac{d}{L}, t_{off} \right)$ is the relative probability for the dimer to localize at x_{min1} during t_{on} . The characteristic diffusion distances are $\Delta x_+ = L + d/2 - \langle x_{min} \rangle$ and $\Delta x_- = \langle x_{min} \rangle - d/2$, and the critical condition, $\Delta x_+ = \Delta x_-$, yields

$$a_c = \frac{1}{2} - \Phi \left(a_c, \frac{d}{L}, t_{off} \right) \frac{d}{L}. \quad (3.6)$$

Note that Eq. (3.6) simplifies to Eq. (3.5) for $d < aL$, where $\Phi = 1$. For $d > aL$, a_c is no longer a linear function of d/L , but also depends on the parameter t_{off} ,

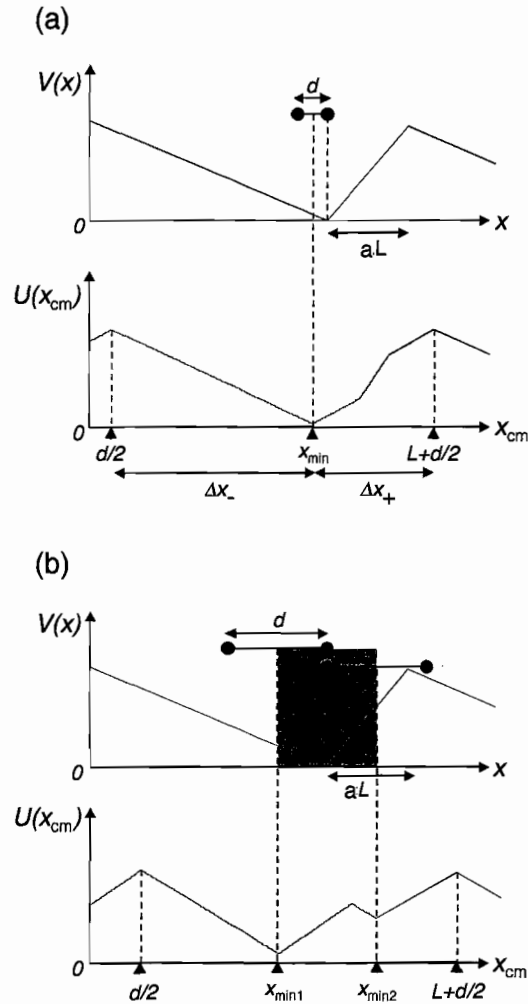


Figure 3.2. Effective potential for dimer in a ratchet potential. (a) Ratchet potential $V(x)$ with $a = 0.25$ (top) and corresponding effective potential $U(x_{cm})$ of a dimer ($d = 0.2L$) in this potential. The effective potential minimum position is $x_{min} = (1 - a)L - d/2$. The minimum diffusion distances for the dimer to be trapped one well forward or one well backward are labeled as Δx_+ and Δx_- respectively. (b) $V(x)$ for $a = 0.25$, and the corresponding $U(x_{cm})$ for a dimer of length $d = 0.33L$. Because $d > aL$, a period of the effective potential has two local minima. The shaded area indicates the region in which the dimer's average center-of-mass position will be found, depending on the relative probabilities for the dimer to localize in either of the two minima (see text).

because the relative likelihood to localize in x_{min1} or x_{min2} during t_{on} depends on the probability distribution at the end of t_{off} .

BD simulations confirm these analytical predictions, demonstrating that the time-averaged velocity of a dimer in a flashing ratchet reverses direction as a function of a , and the critical value, a_c , depends on the dimer length, d/L (fig. 3.3). The simulated a_c decreases linearly with d/L , for $d/L < 1/4$, and is no longer linear with d/L for $d/L > 1/4$ (Eq. (3.6)).

In general, for a chain of N particles with separation d , the number and locations of local minima in the effective potential depend on: (1) Is $a < 1/N$, such that one particle on the steep slope of $V(x)$ would experience a stronger force than $(N - 1)$ particles on the shallow slope? (2) Is $d < aL$, such that each period of $U(x_{cm})$ will have a single minimum with both particles localized in a single well of $V(x)$?

Based on these criteria, the behavior of a trimer (three coupled particles) can be discussed in terms of four qualitative regimes: (I) $a < 1/N = 1/3$ and $d < aL$; (II) $a < 1/N = 1/3$ and $d > aL$; (III) $a > 1/N = 1/3$ and $d < aL$; and (IV) $a > 1/N = 1/3$ and $d > aL$.

Regime I ($a < 1/3$, $d < aL$), illustrated in fig. 3.4(a): Because $a < 1/3$, the force due to $V(x)$ on one particle on the steep slope is larger than the net force on two particles on the shallow slope. This means that the trimer will localize so that none of the particles reside on the steep slope ($x_{min} = (1 - a)L$). Because $d < aL$, such that the trimer can not straddle adjacent wells of $V(x)$, there is only one local

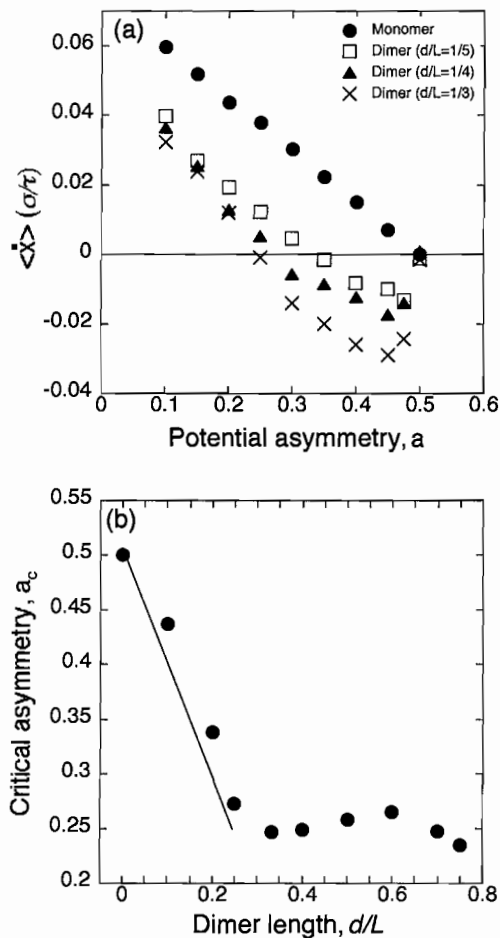


Figure 3.3. Simulations: Reversal of ratchet velocity for dimers of different length. (a) Time-averaged velocity as a function of a for several dimer lengths, for low temperature ($kT/V_0 = 1/50$), and $t_{\text{on}} = t_{\text{off}} = 20\tau$. (b) Critical asymmetry, a_c , as a function of d/L . Data for $d/L < 1/4$ is in qualitative agreement with the analytical prediction of eq. 3.5, $a_c = 1/2 - d/L$ (solid line).

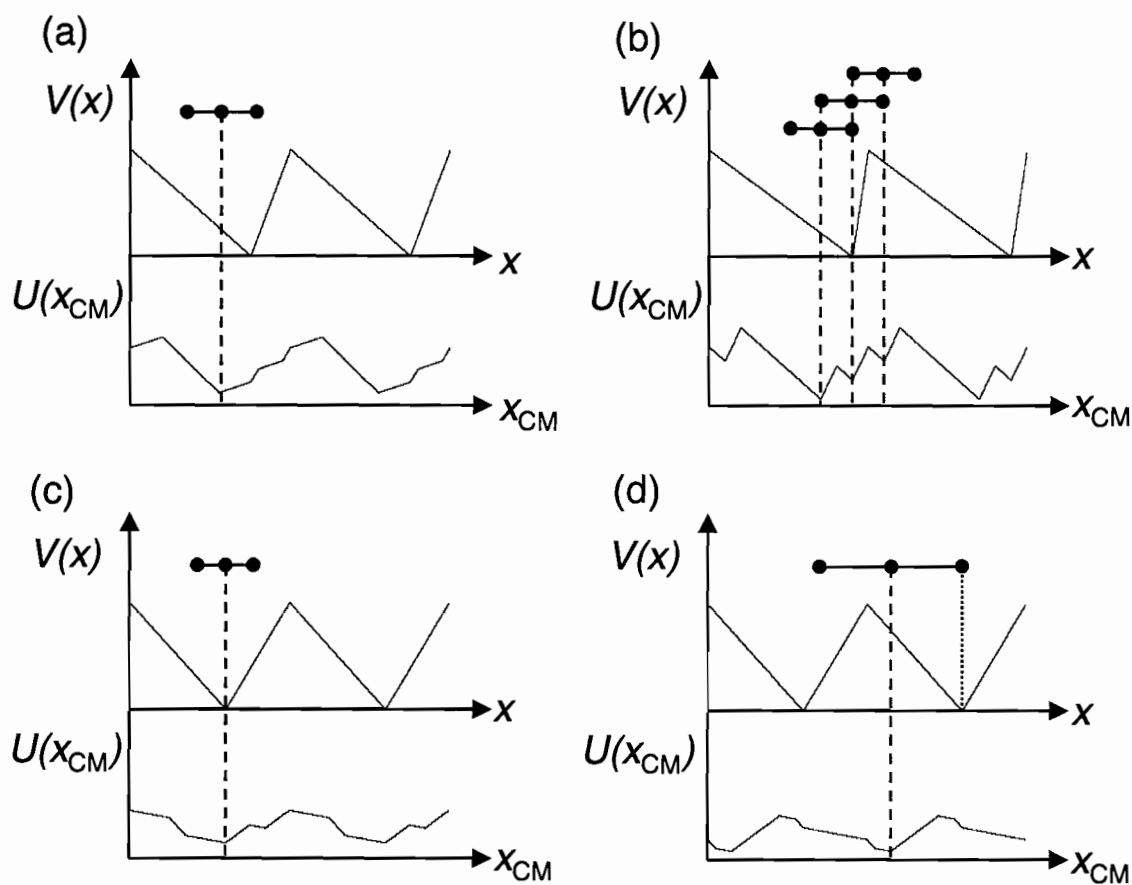


Figure 3.4. Effective potential for trimer in a ratchet potential. Schematic of $V(x)$ and the corresponding $U(x_{cm})$ for a trimer constrained to 1D motion. Localization positions in the limit $kT \ll V_0$ are indicated for the cases: (a) $a < 1/3$ and $d < aL$; (b) $a < 1/3$ and $d > aL$; (c) $a > 1/3$ and $d < aL$; and (d) $a > 1/3$ and $d > aL$.

minimum in a period of $U(x_{cm})$. This gives $\Delta x_+ = L + d - x_{\min} = aL + 2d$ and $\Delta x_- = x_{\min} - d = (1 - a)L - 2d$. The critical condition, $\Delta x_+ = \Delta x_-$, yields

$$a_c = \frac{1}{2} - \frac{2d}{L}. \quad (3.7)$$

Regime II ($a < 1/3$, $d > aL$), illustrated in fig. 3.4(b): Because $d > aL$, the effective potential for the trimer has three local minima. The critical asymmetry, a_c , depends on the relative probability for localization in each of these minima. For $a < 1/2$, the trimer is most likely to localize in the minima furthest to the left ($x_{cm} = (1 - a)L$), assuming an approximately even probability distribution at the end of t_{off} . Therefore, it is likely that $\Delta x_+ > \Delta x_-$ for some $a < 1/2$, yielding $a_c < 1/2$, such that a velocity reversal can occur as a function of d/L .

Regime III ($a > 1/3$, $d < aL$), illustrated in fig. 3.4(c): Because $a > 1/3$, the force on one particle on the steep slope of $V(x)$ is greater than the net force on two particles on the shallow slope. This shifts the localization position in the $+x$ -direction compared with the $a < 1/3$ case, yielding: $x_{\min} = (1 - a)L$. In this case, $\Delta x_+ = L - x_{\min} = aL$ and $\Delta x_- = x_{\min} = (1 - a)L$, such that the effective potential has the same symmetry as the applied potential. This yields $a_c = 1/2$, so the velocity is always positive for $a < 1/2$.

Regime IV ($a > 1/3$, $d > aL$), illustrated in fig. 3.4(d): Because, $d > aL$, the trimer can localize with adjacent particles straddling a maximum of $V(x)$. The lowest energy position for the trimer is to have the leading particle at the minimum of a

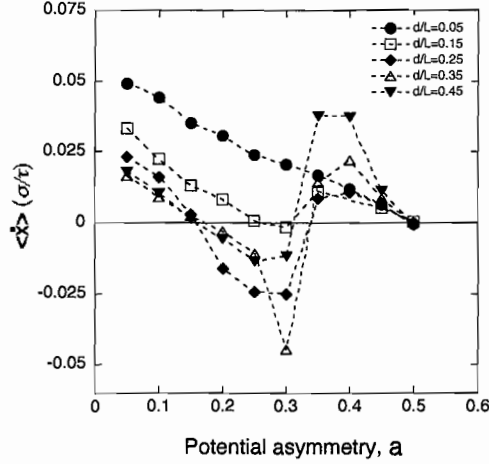


Figure 3.5. Simulations: Reversal of ratchet velocity for trimers of different length. (a) Time-averaged velocity as a function of a for several trimer lengths, for low temperature ($kT/V_0 = 1/50$), and $t_{\text{on}} = t_{\text{off}} = 20\tau$.

period of $V(x)$. In this case, $\Delta x_+ = L + d - x_{\text{min}} = 2d - (1 - a)L$ and $\Delta x_- = x_{\text{min}} - d = (2 - a)L - 2d$, which gives a critical asymmetry $a_c = 3/2 - 2d/L$. Because $d/L > a > 1/3$, this yields: $a_c < 1/6$, which means that the condition for reversal is never met in this regime, and the velocity will always be positive.

These prediction for the ratchet transport of a trimer can be summarized in the following way: The velocity is always positive for $1/3 < a < 1/2$. The critical asymmetry, a_c , increases for decreasing d/L . If $a_c > 1/3$, no velocity reversal is predicted for $a < 1/2$. On the other hand, if d/L is large enough that $a_c < 1/3$, two reversals are predicted as a is increased from zero to $1/2$: from positive to negative at $a = a_c$, and from negative to positive at $a = 1/3$. These predictions are confirmed by BD simulations (fig. 3.5).

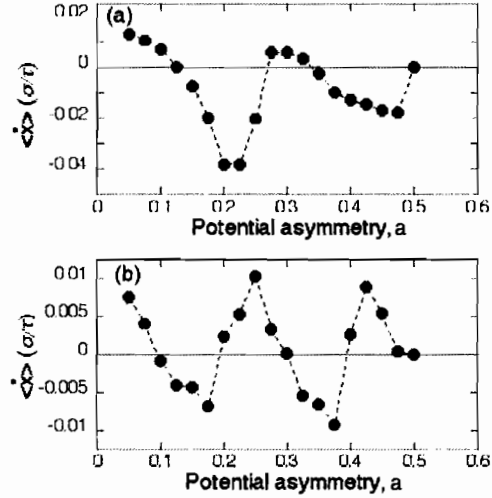


Figure 3.6. Simulations: Multiple reversals for particle chains. (a) Average velocity versus a for a chain of $N = 4$ particles, with $d = 0.2L$, $kT/V_0 = 1/50$, $L = 5\sigma$ and $t_{\text{on}} = t_{\text{off}} = 20\tau$. The dashed line between data points is included as a guide to the eye. (b) Velocity versus a for $N = 5$, with the same parameters as in (a).

In general, because a chain of N particles can have up to N local minima in the effective potential, $N - 1$ reversals in the range $0 < a < 1/2$ are possible for the right choice of parameters. We have specifically predicted, both analytically and numerically, the possibility of one reversal for a dimer and two reversals for a trimer. BD simulations demonstrate that the velocity can reverse three times for a chain of $N = 4$ particles and four times for a chain of $N = 5$ particles (fig. 3.6). Note that, for simplicity, we have considered chains of total length less than the spatial period of the ratchet ($(N - 1)d < L$).

A key result of this section is that the extended geometry of a chain of particles affects the direction of transport in a flashing ratchet. Even though the chain itself has no inherent anisotropy, changing the size of the chain can reverse the symmetry of

the effective potential, thus reversing the direction of transport. This result depends on the discrete spacing of the chain. If the particle separation goes to zero ($d \rightarrow 0$), producing a continuous rod instead of a chain of discrete points, the critical asymmetry is $a_c = 1/2$ for the following reason: The net force is zero if a fraction, a , of the rod experiences the steep slope of the potential. This means that it will localize with a fraction, a , of its length on the steep slope on average during t_{on} . In order to be trapped in an adjacent well after a t_{off} interval, it must diffuse at least far enough that a fraction a of its length is to the left of a $V(x)$ maximum. For a rod with total length m , this gives $\Delta x_+ = aL + (1 - 2a)m$ and $\Delta x_- = (1 - a)L + (2a - 1)m$, yielding $a_c = 1/2$.

Temperature Dependence

As discussed above, the critical condition for velocity reversal, $\Delta x_+ = \Delta x_-$, depends on the potential asymmetry, a , the interparticle separation, d/L , and the temperature, kT/V_0 . In this section, the temperature dependence of ratchet transport of mechanically coupled particles in 1D is compared with that of non-interacting particles.

The temperature of the heat bath affects flashing ratchet velocity in the following ways: (1) The diffusion constant increases linearly with temperature, according to the Einstein-Schmoluchowski relation ($D = kT/\gamma$) [117, 118]. This affects the magnitude (but not the direction) of the velocity. (2) In the low-temperature limit ($kT \ll V_0$), the

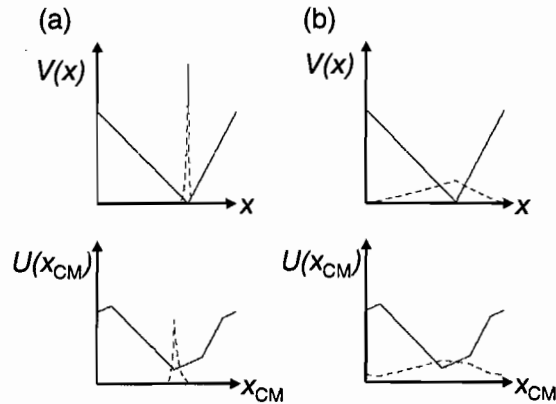


Figure 3.7. Temperature dependence of probability distribution. (a) In the upper panel, a ratchet potential, $V(x)$, with $a = 0.35$ is shown (solid line) with the normalized Boltzmann probability distribution for a point particle exposed to $V(x)$, with $kT/V_0 = 1/50$. In the lower panel, the effective potential, $U(x_{cm})$, corresponding to a dimer of length $d = 0.2L$ exposed to the same potential at the same temperature is shown along with the corresponding probability distribution for the center-of-mass position for the dimer. (b) Same as (a), but for a higher temperature: $kT/V_0 = 2$.

mean position of an object is equal to the minimum of its effective potential $U(x_{cm})$.

As the temperature increases, the Boltzmann probability distribution broadens ($\rho(x_{cm}) \propto \exp(\frac{-U(x_{cm})}{kT})$). If the effective potential is asymmetric near the minimum, the mean of the distribution will shift toward the shallower slope, as illustrated in fig. 3.7.

For non-interacting point particles in $V(x)$, increasing the temperature reduces the magnitude of the effective asymmetry of the system, by shifting the mean in the $-x$ direction (fig. 3.7). However, it does not change the direction, because the mean is never less than $L/2$ in a sawtooth potential with $a < 1/2$. One-dimensional particle chains, which experience a more complicated effective potential, will sample regions of the effective potential with different slopes for increasing temperature (fig. 3.7). Depending on the relative slopes of the regions of the effective potential, increasing

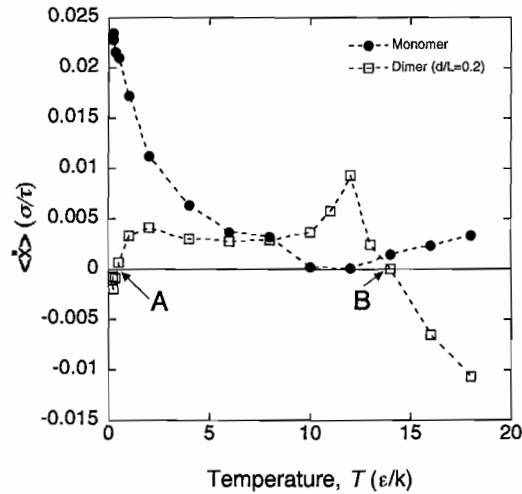


Figure 3.8. Simulations: Reversal of dimer velocity as a function of temperature. Time-averaged velocity as a function of temperature for a point particle and for a dimer of length $d = 0.2L$, using $L = 5.6\sigma$, $V_0 = 5$, $a = 0.35$, and $t_{on} = t_{off} = 20\tau$. The dashed line between data points is included as a guide to the eye. For the dimer, the direction of velocity reverses twice as a function of temperature (points labeled A and B).

the temperature can reverse the symmetry of the probability distribution, producing a reversal in the average velocity. Because a period of $U(x_{cm})$ has several regions of different slope, it is possible for more than one reversal to occur as a function of temperature for a chain of two or more particles.

In fig. 3.8, BD simulations demonstrate that the time-averaged velocity for a dimer reverses direction twice as a function of temperature: from negative to positive, and from positive back to negative. These simulations are for a choice of d/L that yields $a_c < 1/2$ in the low-temperature limit, as discussed in the previous section. In contrast, a point particle always has positive velocity under the same conditions.

Coupled Motion in Three Dimensions

In the previous sections, a purely one-dimensional system was considered. What happens if the particle chain is allowed to move in three dimensions? For a freely rotating dimer exposed to the same 1D external potential, $V(x)$, the effective potential, $U(x_{cm})$, depends on both the center-of-mass position and the rotational orientation of the dimer. The critical condition, $\Delta x_+ = \Delta x_-$, for velocity reversal can be determined in the $kT \ll V_0$ limit by making the following observations (illustrated in fig. 3.9): (1) During t_{on} , the dimer will localize with both particles at a minimum of $V(x)$, such that $x_{cm} = (1 - a)L$ with respect to the beginning (maximum) of that period of $V(x)$. (2) During t_{off} , the probability distribution for the particles is a spherical shell of diameter d centered at the dimer's center of mass.

When the potential is turned on, the dimer will be trapped one well forward if at least a fraction $(1 - a)$ of the charge distribution is in the adjacent well in the $+x$ direction. The probability distribution of a freely rotating dimer meets this criteria when $x_{cm} > L + d/2 - ad$, where $x_{cm} = 0$ indicates the beginning of the original well of $V(x)$. Likewise, if $x_{cm} < d/2 - ad$ when the potential turns on, the dimer will on average be trapped one well backward. Thus, $\Delta x_+ = L + d/2 - ad - x_{min} = aL + d/2 - ad$ and $\Delta x_- = x_{min} - (d/2 - ad) = (1 - a)L - d/2 + ad$. The condition, $\Delta x_+ = \Delta x_-$, yields $a_c = 1/2$, which means that the velocity reversals predicted in the previous section do not hold for a freely rotating dimer. This applies to chains of

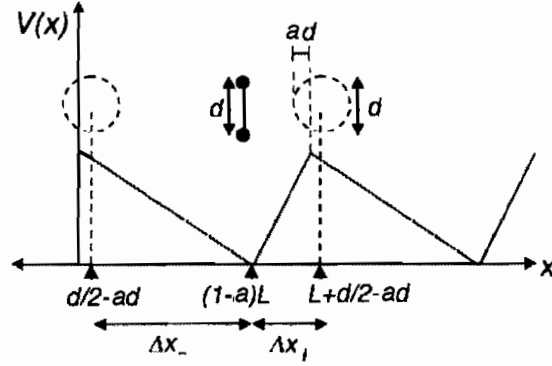


Figure 3.9. Schematic: 3D dimer. A freely rotating dimer with $d < aL$ experiences on average no net linear force in the instant when the potential turns on if the center-of-mass position is: $x_{cm} = L + d/2 - ad$ or $x_{cm} = d/2 - ad$. The dashed line circles above indicate the spherical positional probability distribution about these center-of-mass positions before the potential turns on, which can be used to predict the likelihood for the dimer to localize in either of the two adjacent wells (see text). Assuming that the dimer localizes with $x_{cm} = (1 - a)L$ during t_{on} , the average diffusion distances during t_{off} that are necessary to localize in an adjacent well are Δx_- and Δx_+ .

arbitrary N , because the probability distribution for the particles during t_{off} can be described as a set of concentric spherical shells, and therefore the symmetry arguments made here for a dimer also hold for $N > 2$.

In fig. 3.10, BD simulations confirm that the velocity of a freely rotating dimer matches that of a point particle, in contrast to the velocity reversal that occurs for a dimer constrained to 1D motion.

Finite-sized Spherical Bead in a Quasi-one-dimensional Ratchet

Previous sections of this chapter have addressed size effects that arise in flashing ratchet transport of mechanically coupled point particles. Here, we discuss the transport of a finite size spherical bead in a flashing ratchet. Fig. 3.11(a) illustrates

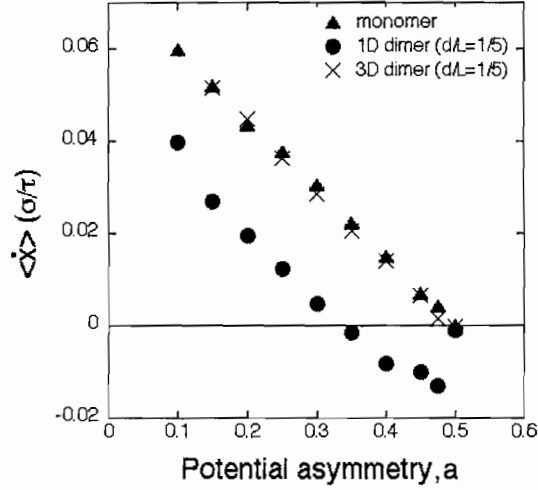


Figure 3.10. Simulations: Velocity of a freely-rotating dimer in a flashing ratchet. Time-averaged center-of-mass velocity as a function of a for a dimer in a three-dimensional system exposed to a ratchet potential $V(x)$, with $kT/V_0 = 1/50$, $L = 5.6\sigma$, $d = 0.2L$, and $t_{on} = t_{off} = 20\tau$. Data from fig. 3.3(a) for a dimer constrained to one-dimensional motion and for a monomer are included here for comparison.

the positions that define the minimum and maximum of the effective potential of a bead of radius r in a potential of spatial period L .

The characteristic diffusion distances, Δx_+ and Δx_- , for a finite bead can be determined by calculating the center-of-mass position at which the net force on the bead is zero. The force on any particle in the region to the right of a potential maximum is $f_+ = \frac{V_0}{1-a}$, and the force on a particle to the left of a potential maximum is $f_- = \frac{-V_0}{a}$. Because a rigid object can be considered to be a collection of particles held at fixed distances to one another, the total force exerted on the bead is

$$f_{tot} = \frac{V_0 W(h)}{1-a} - \frac{V_0 (W_{tot} - W(h))}{a}, \quad (3.8)$$

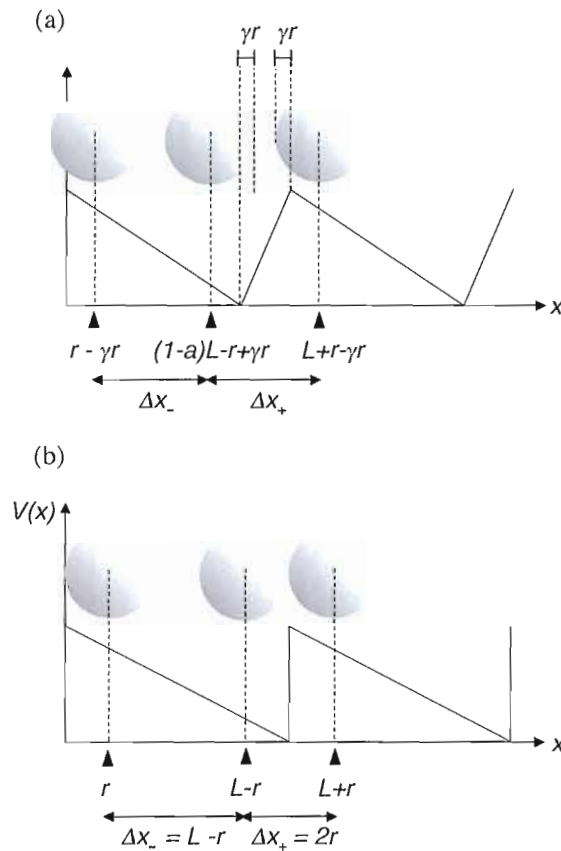


Figure 3.11. Schematic: finite-sized bead. A spherical bead of diameter $d = 2r$ in a sawtooth potential, $V(x)$, experiences zero net force if a fraction, γ , of the bead's radius resides on the steep side of the potential, where γ depends on the potential asymmetry, a , as defined in equation 3.11. By determining $\gamma(a)$, it is possible to calculate the critical distances, Δx_+ and Δx_- , that the bead must diffuse during t_{off} in order to be trapped in an adjacent well at the beginning of t_{on} . (b) A spherical bead in a sawtooth potential of asymmetry $a = 0$ has $a_{\text{eff}} = \Delta x_+/L = d/L$, as illustrated.

where $W(h)$ is the volume of a cap of height h that resides to the right of a potential maximum, and $W_{tot} = \frac{4\pi r^3}{3}$ is the total volume of the sphere. For a sphere of radius r , a cap of height h has volume:

$$W(h) = \frac{\pi h^2}{3}(3r - h). \quad (3.9)$$

We define a parameter γ as the fraction of the bead radius that must reside on a steep slope of the sawtooth potential in order for the net force on the bead to be zero. In terms of this parameter, the condition for zero net force in a sawtooth potential with asymmetry a is:

$$\frac{W(\gamma r)}{a} = \frac{W_{tot} - W(\gamma r)}{1 - a}, \quad (3.10)$$

Equation 3.10 yields

$$3\gamma^2 - \gamma^3 = 4a. \quad (3.11)$$

Because Δx_+ depends on the bead's equilibrium positions within the ratchet potential (in other words, on γ), eq. 3.11 allows us to numerically determine Δx_+ in terms of a , as follows (see fig. 3.11(a)): The center-of-mass position that minimizes the effective potential within a period of the ratchet is: $x_{min} = (1 - a)L - r + \gamma r$. In the low temperature limit, the mean of the bead distribution is equal to this position in equilibrium with the potential on. In this case, the minimum distance the bead would need to diffuse on average while the potential is off in order to be trapped

one well forward when the potential turns back on is $\Delta x_+ = L + (1 - \gamma)r - x_{min} = aL + 2r(1 - \gamma)$. The minimum diffusion distance to be trapped one well backward is: $\Delta x_- = x_{min} - (1 - \gamma)r = (1 - a)L - 2r(1 - \gamma)$. In this case, the effective asymmetry of the potential depends on bead diameter, $d = 2r$, as follows:

$$a_{eff} = \frac{\Delta x_+}{L} = a + \frac{d}{L}(1 - \gamma). \quad (3.12)$$

Fig. 3.12(a) shows the effective asymmetry, a_{eff} , as a function of the actual asymmetry, a , for several bead sizes, based on a numerical solution to equations 3.11 and 3.12. For $a = 0$, the effective asymmetry depends only on the bead size: $a_{eff} = d/L$. This situation is illustrated in fig. 3.11(b): In the limit that the steep slope has an infinitely strong force, the mean position of the bead is such that none of its volume resides on the steep slope ($\gamma = 0$), yielding $\Delta x_+ = d$. As a increases from 0 to 1/2, γ increases from 0 to 1, which means that the second term of equation 3.12 decreases with a . Initially, this produces a decrease in a_{eff} with a , followed by an increase in a_{eff} with a for higher a . As a approaches 1/2, the second term of equation 3.12 goes to zero, meaning that $a_{eff} = 1/2$ when $a = 1/2$.

From this calculation, we can conclude that in the limit of strong localization, $V_0 \gg kT$, the value of a_{eff} increases with bead size, which would decrease the average velocity of flashing ratchet transport. For beads larger than $d = L/2$, the effective asymmetry is greater than 1/2 for very small a , which would reverse the direction of flashing ratchet transport. This suggests that for a highly asymmetric (small a)

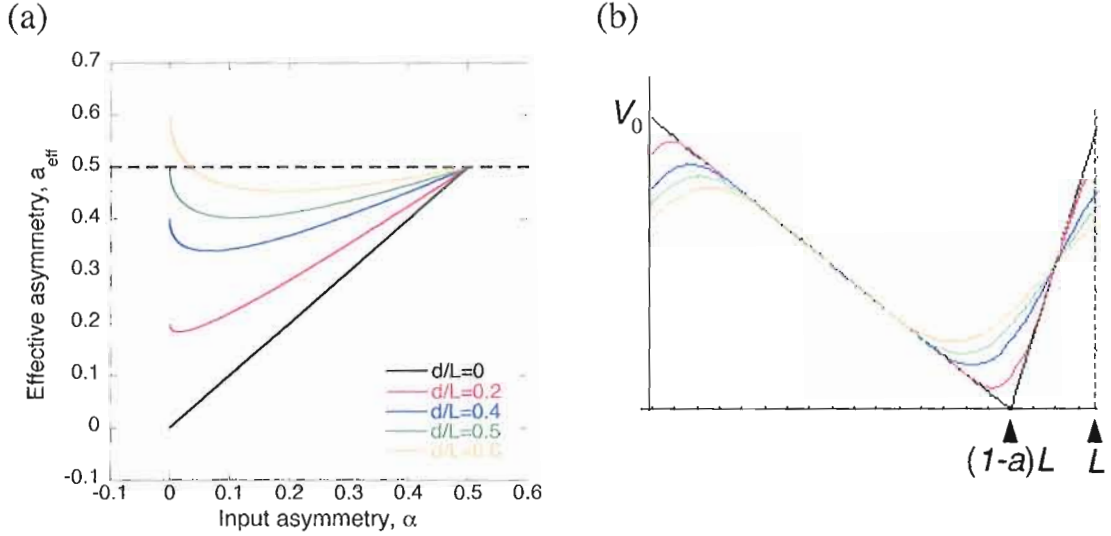


Figure 3.12. Effective potential for finite-sized bead in a ratchet. (a) a_{eff} , as a function of sawtooth asymmetry, a , for several bead sizes, d/L , based on a numerical solution to equations 3.11 and 3.12. (b) The effective potential, $U_{eff}(x_{cm})$, calculated with equation 3.13 for several bead sizes, with a sawtooth asymmetry $a = 0.2$. Colors of lines in (b) correspond to the same values of d/L as in the legend of (a).

potential with high trapping strength, beads of diameter smaller than $L/2$ would be transported in the $+x$ -direction on average, and larger beads would be transported in the opposite direction.

To predict the behavior of a finite sized bead in a flashing ratchet for different values of V_0/kT , we must consider the shape (rather than simply the position of the minimum) of the bead's effective potential, given by the normalized integral over the volume of a sphere centered at x_{cm} weighted by the potential $V(x)$:

$$U_{eff}(x_{cm}) = \frac{3}{4\pi r^3} \int_{x_{cm}=0}^{x_{cm}=L} \int_{x=x_{cm}-r}^{x=x_{cm}+r} V(x) S_V(x, x_{cm}) dx_{cm} dx, \quad (3.13)$$

where $S_V(x, x_{cm})dx$ is the volume of a slice at position x of a sphere centered at position x_{cm} .

Fig. 3.12(b) shows $U_{eff}(x_{cm})$ for several choices of d/L . The slope of the left side of the effective potential well (plus-directed force) is equal to the slope of the left side of the original potential, $V(x)$, while the slope of the right side of the effective potential decreases with increasing bead size. As discussed earlier in this chapter, increasing kT/V_0 broadens the positional distribution and shifts the mean toward the shallower slope. For smaller beads, the left slope is shallower, and the mean of the distribution will shift to the left ($-x$ -direction) with increasing kT , thus increasing the apparent value of a . For larger beads, such that the right slope is shallower, increasing kT/V_0 will shift the mean in the $+x$ -direction, decreasing the apparent value of a .

This is especially relevant to an experimental ratchet system designed in the Linke group, in which dielectric beads are exposed to a quasi-one-dimensional flashing ratchet potential created with a scanning line optical trap (Lopez et al., [51]). About ten spatial periods of length $L = 1.8\mu m$ (with input $a = 0.2$) are realized with this setup, and experimental studies are being carried out with a bead of diameter $d = 0.9\mu m$, such that $d = L/2$.

The effective potential for a bead in the optical ratchet potential closely matches the effective potential predicted by equation 3.13 (fig. 3.13). The following two approaches are used to characterize the experimental effective potential: (1) Population method: The measured positional distribution of the bead while the potential is

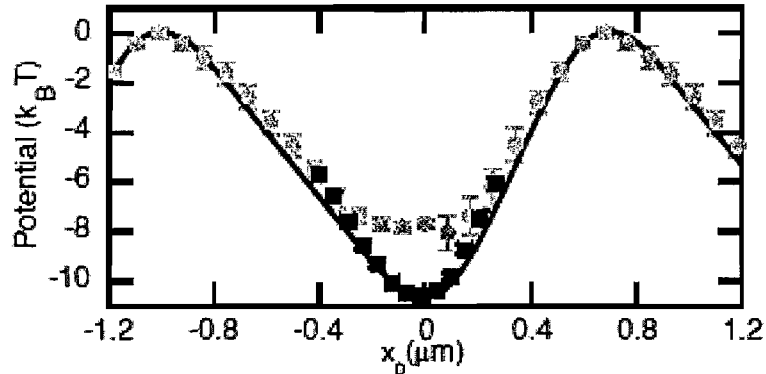


Figure 3.13. Experimental and theoretical effective potential for a finite-sized bead in a ratchet potential (to appear in Lopez et al. [51]): The theoretically calculated effective potential based on equation 3.13 (solid line) is displayed with the experimental effective potential characterized by the population method (black squares) and the velocity method (gray circles) described in the text.

on is used to extrapolate the effective potential from Boltzmann's law: $U(x) = -kT \ln \left(\frac{N(x)}{N_{total}} \right)$. (2) Velocity method: The effective potential can be extrapolated through measurement of the velocity after turning on the potential, based on the position in successive frames. In this case, the potential is calculated as: $U(x) = -\gamma \int_0^x v(x') dx'$. The population gives a good estimate of the potential near the minima, but provides little data near the maxima because the bead spends little time there. The velocity method gives good results near the maxima of the potential, but is less accurate near the minima where the bead is more strongly influenced by noise for which this method does not account. The combination of the two methods in fig. 3.13 demonstrates the close agreement between theory and experiment.

For increasing temperature, we expect the average position of the bead to shift away from the effective potential minimum in the direction of whichever slope is

shallower near the minimum. The effective potential is nonlinear for finite bead sizes, but in the region closest to the minimum for $d = L/2$, the slope is shallower to the right of the minimum (fig. 3.12(b)). For this reason, we expect the average bead position to shift to the right as kT/V_0 increases from zero, which would result in a smaller value of the measured asymmetry parameter a (i.e. a more asymmetric measured potential). In agreement with this theoretical prediction, the experimentally measured value of a decreases with decreased trapping strength. For a trapping potential estimated as $V_0 \approx 60kT$, the measured asymmetry is $a_{meas} \approx 0.4$. This is consistent with the prediction (fig. 3.12(a)) that the measured asymmetry is $a_{meas} \approx a_{eff} = 0.427$ for $d/L = 1/2$ in the high V_0/kT limit. For decreased trapping strength, the measured value of a decreases ($a_{meas} \approx 0.35$, for $V_0 \approx 10kT$).

CHAPTER IV

DELAYED FEEDBACK CONTROL OF FLASHING RATCHETS

Introduction

Most studies of particle transport in a flashing ratchet have been examples of ‘open-loop’ control, in which the control of the system (in other words, the switching of the potential on and off) is enacted independently of the internal state of the system. However, as discussed in chapter I, several recent models have considered ‘closed-loop’ control of a flashing ratchet, in which the potential is switched in response to information about the internal state of the system determined by the particle distribution. These studies have been motivated by an effort to determine a scheme that can produce the highest possible transport velocity in a flashing ratchet, as well as by fundamental interest in a physical system that can test thermodynamic limitations on control of a noisy system (i.e., a concrete application of the famous “Maxwell’s demon” thought experiment).

The first recent studies of closed-loop control of a flashing ratchet assumed an idealized feedback system in which measurements of the particle distribution were taken instantaneously with complete accuracy, and implemented without delay. Motivated by the possibility of experimentally realizing a feedback-controlled flashing ratchet, in

this chapter the impact of experimentally inevitable sources of time delay in feedback are modeled.

Model

Cao et al. [69] recently introduced the following scheme for closed-loop control of particles in a flashing ratchet: Consider an ensemble of N non-interacting, overdamped particles in a one-dimensional flashing ratchet system with periodic potential $V(x)$ (fig. 3.1). The motion of the particles is described by overdamped Langevin equations

$$\gamma \dot{x}_i(t) = \alpha(t)F(x_i(t)) + \xi_i(t); \quad i = 1, \dots, N \quad (4.1)$$

where $x_i(t)$ is the position of particle i , γ is the drag coefficient of a particle, and $\xi_i(t)$ is a randomly fluctuating Gaussian white noise term with zero mean and correlation $\langle \xi_i(t)\xi_j(t') \rangle = 2\gamma kT\delta_{ij}\delta(t-t')$. The external force is given by $F(x) = -V'(x)$, and $\alpha(t)$ is a control parameter that can take the value of 1 or 0, thus switching the external potential on or off.

In order to compare open-loop versus closed-loop control of a flashing ratchet, the following two strategies are considered:

(1) Periodic switching: $\alpha(t+\tau) = \alpha(t)$, with $\alpha(t) = 1$ for $t \in [0, \tau/2)$, and $\alpha(t) = 0$ for $t \in [\tau/2, \tau)$. (A number of studies have investigated this open-loop control strategy for a flashing ratchet system. In the previous chapter, coupling effects in a periodic flashing ratchet are discussed.)

(2) Controlled switching (maximization of the instantaneous velocity (MIV)):

$$\alpha(t) = \Theta(f(t)), \quad (4.2)$$

where

$$f(t) = \frac{1}{N} \sum_i^N F(x_i) \quad (4.3)$$

is the ensemble average of the force the particles would feel if the potential were on, and $\Theta(y)$ is the Heaviside function, $\Theta(y) = 1$ if $y \geq 0$ and 0 otherwise.

In this chapter, two types of experimentally relevant time delay in feedback control are considered (fig. 4.1):

(1) Implementation time, t_1 : If a measurement is taken at time t , any feedback based on this measurement will be implemented at time $t + t_1$. This type of delay arises experimentally because of the time required for data processing.

(2) Measurement interval, t_2 : If a measurement is taken at time t , the next measurement will be taken at time $t + t_2$. This type of delay is related to the speed of the acquisition system in an experiment. For example, the measurement interval would be limited by the readout rate of a camera that acquires images of the particle distribution.

Brownian dynamics (BD) simulations are used here to demonstrate the role of these types of time delay on the MIV control strategy (eq. 4.2). The particle dynamics

in the presence of time delay can be described by

$$\gamma \dot{x}_i(t) = \beta(t)F(x_i(t)) + \xi_i(t); \quad i = 1, \dots, N \quad (4.4)$$

where $\beta(t)$ is the actual state of the system based on a delayed response to the cue $\alpha(t)$. The simulations in this chapter used the following input parameters: $kT = 1$, $kT/\gamma = D = 1$, $L = 1$, and $a = 1/3$, which provides continuity with previous analysis of this control scheme in the absence of delay [69]. In this case, the program time unit can be expressed as $L^2/D = 1$. Unless otherwise noted, $V_0 = 5kT$. It is important to note that the finite time step dt in a Brownian dynamics simulation introduces an inherent measurement delay, t_2 , to the calculation. The behavior of the system in the $t_2 = 0$ limit can be studied by choosing a time step that is very small compared to the characteristic times for diffusion over the length of relevant features of the system (for example, we use $dt = 10^{-6}L^2/D$ for $N = 1$). The performance of each control strategy is evaluated by calculating the time-averaged, center-of-mass velocity, $v_{cm} = \langle \dot{x}_{cm} \rangle$, for the ensemble. This quantity does not depend on the initial distribution of the ensemble when averaged over a sufficient amount of time (several temporal periods).

Implementation Delay

An experimental feedback system with fast data acquisition, but slow information processing, can be approximated as having zero measurement interval ($t_2 = 0$) and

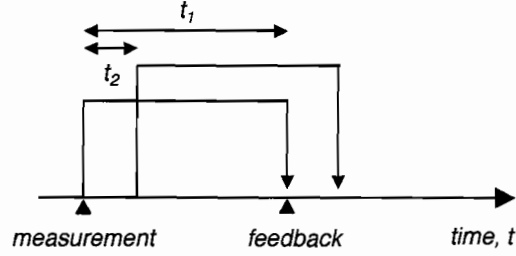


Figure 4.1. Schematic: Two possible types of time delay in feedback control are illustrated above: (1) Implementation delay, t_1 : If a measurement is taken at time t , the implementation of feedback based on this measurement will occur at time $t + t_1$. (2) Measurement interval, t_2 : If a measurement is taken at time t , the next measurement will be taken at time $t + t_2$.

finite implementation delay ($t_1 > 0$). Simulations of this scenario demonstrate that the impact of implementation delay on feedback control depends on the ensemble size in the following way:

Small N : For $N = 1$ in the absence of implementation delay, $t_1 = 0$, the feedback control strategy (eq. 4.2) yields $v_{cm} = 4.27 D/L$, an order of magnitude faster than the optimal velocity, $v_{opt} \approx 0.284D/L$, for a periodic flashing ratchet under the same conditions with optimized temporal period $\tau = \tau_{opt} \approx 0.1L^2/D$. However, the velocity falls off with t_1 on a time scale comparable to the mean time to diffuse the length of the ratchet's critical length scale aL ($t \approx (aL)^2/2D \approx 0.05L^2/D$). BD simulations demonstrate that v_{cm} drops below v_{opt} for delay greater than $t_1 \approx 0.03 - 0.05L^2/D$ (fig. 4.2). For small N , the feedback strategy loses effectiveness when the implementation delay is comparable to or larger than the time it takes for measured and actual particle positions to become uncorrelated in terms of position with respect to features of $V(x)$.

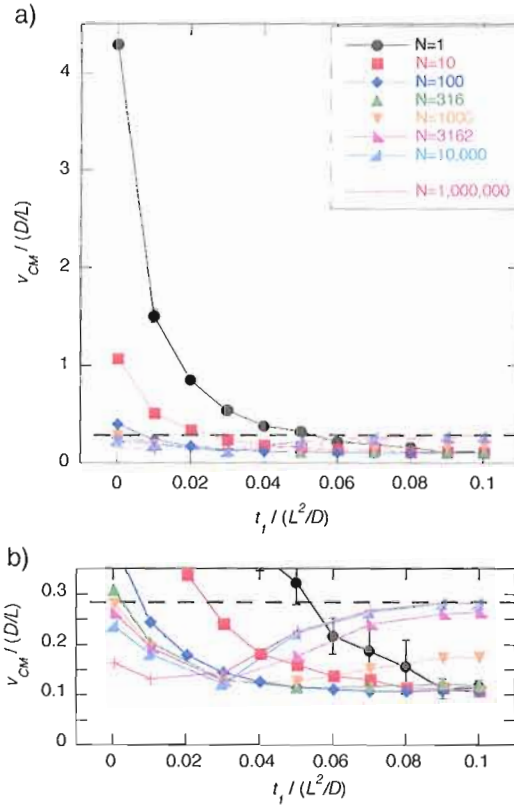


Figure 4.2. Simulations: Implementation delay in a feedback-controlled ratchet. (a) Time-averaged velocity as a function of implementation delay, t_1 , in the absence of measurement delay ($t_2 = 0$) for different ensemble sizes. The lines between data points are included as a guide to the eye. The dashed line indicates the time-averaged velocity for non-interacting particles in a periodically flashing ratchet with optimal temporal period $\tau_{opt} = 0.1 L^2/D$. (b) An enlarged view of (a) for small velocities. Error bars are included for $N = 1$. For $N \geq 10$, the error is smaller than 0.1% of the magnitude of the velocity.

Large N ; small t_1 : As the number of particles increases, the mean amplitude of the center-of-mass fluctuations in $f(t)$ decreases, making the time-evolution of the system more deterministic. For large N , the role of a small implementation delay, t_1 , can be understood by considering the characteristics of $f(t)$ (demonstrated for $N = 10^6$ in fig. 4.3(a)). The simulation starts with the potential on ($\alpha = 1$) and particles equilibrated in the potential, such that $f \approx 0$. A fluctuation yielding $f(t) < 0$ produces a cue to turn the potential off ($\alpha \rightarrow 0$), which is implemented after a delay t_1 ($\beta(t) = \alpha(t - t_1)$ for $t_2 = 0$). When the potential turns off, $f(t)$ rapidly decreases because the particles diffuse evenly in each direction, such that about half the ensemble moves into a region with a large negative force when the potential is on. Rapid shifts in $f(t)$ are observed for a duration of about t_1 , indicative of the delayed response to cues that were triggered during the time delay between the initial cue to turn off and the implementation of that cue. The ensemble equilibrates in the ‘off’ state ($\beta = 0$), such that the average force again approaches $f(t) \approx 0$. Once a center-of-mass fluctuation yields $f(t) > 0$, a cue to turn the potential on ($\alpha \rightarrow 1$) is implemented after a delay t_1 . After the potential turns back on, particles on the steep slope quickly localize near the minimum of $V(x)$, while particles on the shallow slope take longer to reach the minimum, resulting in an increase in $f(t)$ before the ensemble equilibrates to $f(t) \approx 0$. Again, $f(t)$ fluctuates in response to previous cues for a time interval of about t_1 . In summary, a small implementation delay, t_1 ,

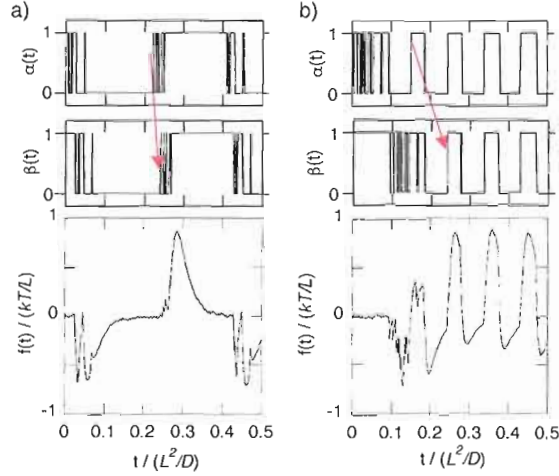


Figure 4.3. Simulations: Average force in a time-delayed feedback ratchet. (a) Ensemble-averaged force $f(t)$ for $N = 10^6$, $t_1 = 0.02L^2/D$, and $t_2 = 0$. The measured state (‘cue’), $\alpha(t)$, and the implemented state (‘response’), $\beta(t)$, are shown above. Arrows indicate the time delay between the a cue and the response to that cue. Initially, particles are equilibrated in the ‘on’ state. (b) Same, except $t_1 = 0.09L^2/D$.

decreases the velocity by delaying the modulation of the potential and by introducing unproductive fluctuations in $f(t)$ after the potential is switched.

Large N ; large t_1 : For large N , it is possible for an implementation delay to *improve* the performance of the feedback control policy, producing a higher velocity than in the absence of time delay. This somewhat counter-intuitive result arises for a range of implementation delays that allow the system to synchronize into a stable mode of oscillation in which the state switches when the system is away from equilibrium, avoiding the unproductive intervals of $f(t) \approx 0$ seen for smaller t_1 . As shown in fig. 4.3(b), for $t_1 = 0.09L^2/D$, after a small number of initial cycles, a cue created in one cycle of the potential correctly triggers a switching event in the *next* cycle. This mode of oscillation is stable when t_1 is large enough for $f(t)$ to reach its

maximum $|f|$ before a subsequent cue is triggered, thus avoiding rapid fluctuations of the sign of $f(t)$ and allowing time for the ensemble center of mass to evolve. For the simulations shown in fig. 4.3(b), the initial transient toward maximum $|f|$ is approximately $0.03L^2/D$, consistent with the result that v_{cm} increases with t_1 for $N > 10^3$ when $t_1 > 0.03L^2/D$ (fig. 4.2).

To illustrate the synchronization of cues that produces the $\tau = t_1$ periodic mode, fig. 4.3(b) shows simulations of the cue, $\alpha(t)$, and the response, $\beta(t)$, for $N = 10^6$ particles in a feedback-controlled flashing ratchet with $t_1 = 0.1L^2/D$ and $t_2 = 0$. Fig. 4.7(a) is a corresponding schematic that illustrates the timing of the mode-locking for this example: At $t = t_0$, the potential turns on ($\beta \rightarrow 1$) in response to a previous cue ($\alpha \rightarrow 1$) that was triggered at $t = t_0 - t_1$. Because there is no measurement delay, when the potential turns on at $t = t_0$, this triggers a new ‘on’ cue ($\alpha \rightarrow 1$). At $t_0 + 0.5t_1$, the potential turns off ($\beta \rightarrow 0$) in response to an ‘off’ cue at $t_0 - 0.5t_1$. This triggers a new ‘off’ cue ($\alpha \rightarrow 0$) because $f(t)$ has become negative. The resulting oscillatory mode has a period $\tau = t_1 = t_{on} + t_{off}$, and is synchronized in a way that the cue and response are in phase with each other ($\alpha(t) = \beta(t)$). The potential spends equal time on and off ($t_{on} = t_{off}$).

In summary, for large N and $t_1 > 0.03L^2/D$, the system can synchronize into a mode of oscillation in which a cue in one cycle is implemented in the next cycle, producing a temporal period of about $\tau = t_1$ (fig. 4.4). This mode has a larger velocity than a flashing ratchet with instantaneous feedback control, because it does not rely

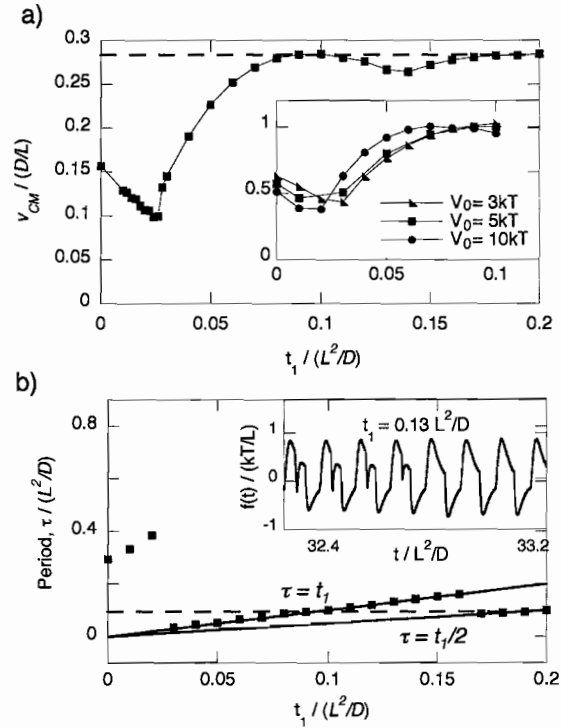


Figure 4.4. Simulations: Time-delayed feedback control of a large ensemble ($N = 10^6$ data from fig. 4.2). (a) Time-averaged velocity as a function of implementation delay, t_1 , for $t_2 = 0$ and $N = 10^6$. The lines between data points are included as a guide to the eye. The dashed line shows the average velocity, v_{opt} , for a periodically flashing ratchet with optimal period. Inset: Average velocity as a function of t_1 for several values of V_0 , each normalized by the velocity v_{opt} for optimal periodic switching corresponding to that V_0 and $\alpha = 1/3$. (b) Average temporal period of the stable periodic mode of the system, based on the same simulation data as in (a). The solid lines indicate the following two modes of quasiperiodic, stable oscillation: (1) $\tau = t_1$, such that a cue in one cycle is implemented in the following cycle; and (2) $\tau = t_1/2$, such that a cue in one cycle is triggered after two cycles. Inset: Example of a transition from a metastable to a more stable mode of oscillation.

on fluctuations in $f(t)$ to trigger a change in the potential. For $t_1 \approx \tau_{opt} = 0.1L^2/D$, the velocity is equal to the optimal velocity, v_{opt} , for a periodically flashing ratchet. This key result is independent of V_0 , as illustrated in the inset of fig. 4.4(a), which shows the ratio v_{cm}/v_{opt} (noting that v_{opt} is a function of V_0). For increasing V_0 , the velocity is optimized for smaller t_1 , because particles localize in the potential more quickly and, therefore, $v_{cm} = v_{opt}(V_0)$ is achieved for smaller t_1 .

Interestingly, for even larger t_1 , modes are observed in which a cue is implemented multiple periods later. The system takes longer to synchronize into these modes, sometimes taking hundreds of oscillations before the modulation of $f(t)$ stabilizes into a periodic mode. For implementation delay above $t_1 \approx 0.16L^2/D$, simulations demonstrate synchronization into a mode in which a cue is implemented two cycles later. In this case the stable period is $\tau \approx t_1/2$. Near the boundary between the $\tau = t_1$ mode and the $\tau = t_1/2$ mode, the system demonstrates quasi-stability in either mode, and is sometimes observed to become metastably synchronized in one mode for hundreds of cycles before locking into the other mode (for example, see the inset to fig. 4.4(b)). In general, these modes display stability for at least 10^4 cycles. One can expect these synchronized, periodic modes to remain stable indefinitely in the high N limit, as the dynamics of the system become increasingly deterministic.

Measurement Delay

Many experimental setups require significant time for data collection as well as information processing. Feedback control of such a system will be affected by implementation delay, t_1 , and measurement delay, t_2 . Here we discuss feedback control of a flashing ratchet in the presence of both of these types of delay ($t_1 > 0$ and $t_2 > 0$).

Small N : The average velocity, v_{cm} , decreases with t_1 for all t_2 , but the steepness of the falloff depends on t_2/t_1 (fig. 4.5(b)). The velocity decreases with t_1 fastest when $t_2 > t_1$, because the large measurement delay introduces idle time in each cycle after a cue has been implemented and before a new cue is triggered. However, the decrease of v_{cm} is less steep for $0 < t_2 < t_1$ than for $t_2 = 0$, because a finite measurement interval allows some diffusion between measurements, such that fewer cues are triggered while $f \approx 0$. This reduces the amount of unproductive fluctuations in response to these cues.

Large N : In the previous section, it was demonstrated that for $t_2 = 0$, a well-chosen implementation delay t_1 allows the system to synchronize into a mode of oscillation that reproduces that of an optimal periodic flashing ratchet. Here, the impact of measurement delay, t_2 , is discussed by considering several regimes of t_2/t_1 . Fig. 4.6 shows simulations of the characteristic oscillatory modes that arise for different values of t_2/t_1 , for optimal choice of t_1 . Fig. 4.7 provides a schematic illustrating the cue-response synchronization that gives rise to each of these modes.

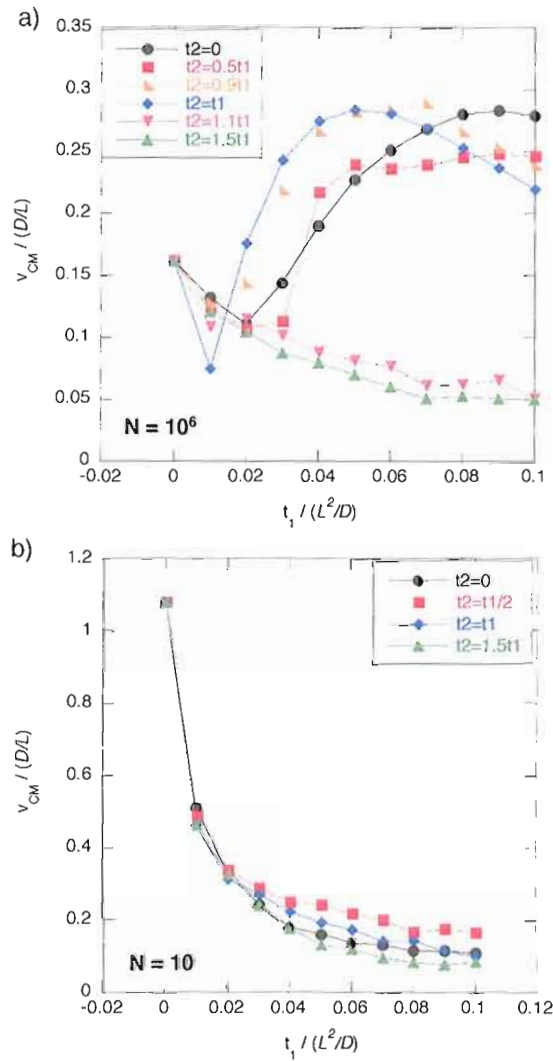


Figure 4.5. Simulations: Impact of implementation delay and measurement delay. (a) Time-averaged velocity as a function of implementation delay, t_1 , for $N = 10$ and several regimes of measurement delay relative to the implementation delay (t_2/t_1). The behavior is qualitatively different for $t_2 < t_1$ and $t_2 > t_1$, as discussed in the text. (b) Same as (a), except for $N = 10$. The lines between data points are included as a guide to the eye.

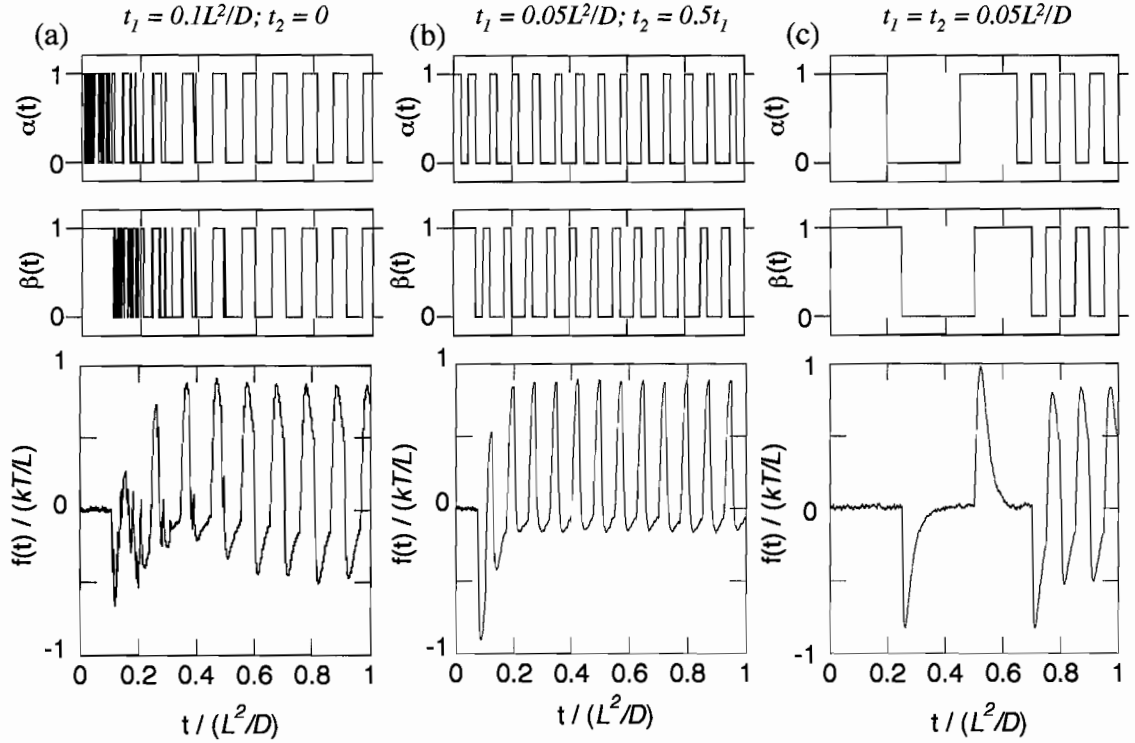


Figure 4.6. Simulations of mode-locking for a large ensemble ($N = 10^6$) in a flashing ratchet with time-delayed feedback. The measured state ('cue'), $\alpha(t)$, and the implemented state ('response'), $\beta(t)$, are shown above. At time $t = 0$, the potential is on and the particles are equilibrated in the potential. Several values of implementation delay, t_1 , and measurement interval, t_2 , are shown: (a) $t_1 = 0.1L^2/D$ and $t_2 = 0$; (b) $t_1 = 0.05L^2/D$ and $t_2 = 0.5t_1 = 0.025L^2/D$; (c) $t_1 = t_2 = 0.05L^2/D$.

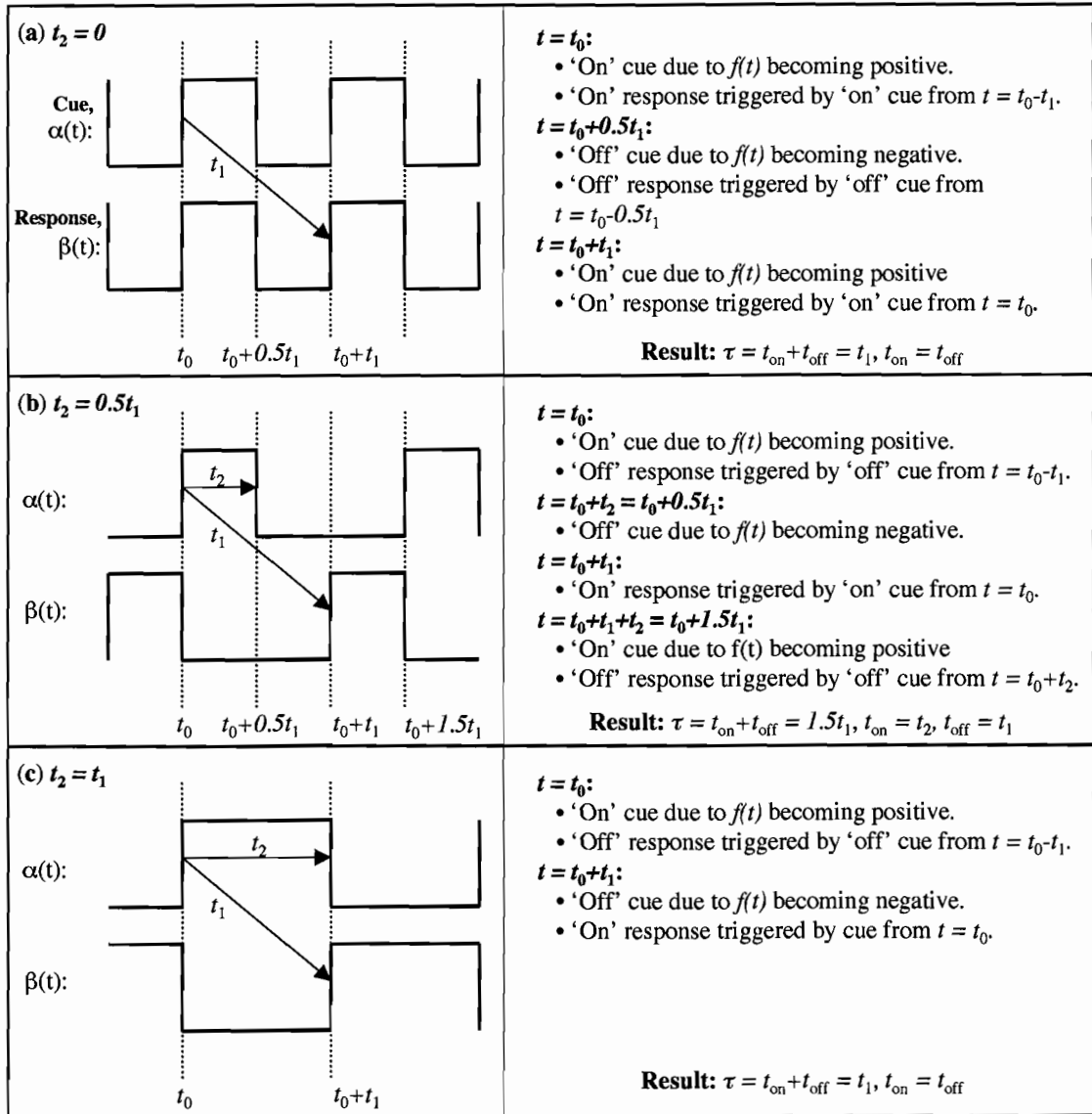


Figure 4.7. Schematic: Mode-locking with measurement and implementation delays. The synchronized modes of oscillation for high N (based on the simulation data in fig. 4.6) are illustrated in the schematic above for: (a) $t_2 = 0$; (b) $t_2 = 0.5t_1$; and (c) $t_2 = t_1$.

In a feedback system with $t_2 \geq t_1$, a new measurement is only taken after the previous measurement has been implemented. This is analogous to a Maxwell's demon (see chapter I) that does not “multi-task”: the task of opening and shutting the gate must be completed before the demon can go back to monitoring the particle bath. This could arise experimentally if: (1) the same software is responsible for data acquisition and data processing; or (2) there are limitations on how much information can be stored at one time.

In particular, if $t_2 = t_1$, a new measurement is taken at the same instant that the previous measurement is implemented. If a cue to turn on (off) is triggered at time t_0 , it will be implemented at time $t_0 + t_1$. The next measurement (cue) is taken at the same instant ($t = t_0 + t_1 = t_0 + t_2$), before $f(t)$ has time to change signs in response to the potential being turned on (off). This triggers a new cue of opposite sign to the previous cue. The resulting oscillatory mode has $\tau = 2t_1$ and $t_{on} = t_{off} = t_1 = t_2$ (figs. 4.6(c) and 4.7(c)). The cue and the response are out of phase with each other, such that $\alpha(t) = 1$ whenever $\beta(t) = 0$ and vice versa. The average velocity as a function of implementation delay, t_1 , is essentially the same as in the $t_2 = 0$ case, except that now the dependence on t_1 is compressed to smaller t_1 values, because $\tau = 2t_1$ instead of $\tau = t_1$. In this case the velocity is optimized for $t_1 = 0.5\tau_{\text{opt}}$ (see fig. 4.5(a)).

If $t_2 > t_1$, the synchronization-induced increase in velocity discussed above does not occur, for the following reason: If the potential turns on (off) at time $t_0 + t_1$ in

response to a cue at time t_0 , the next cue is triggered at time $t_0 + t_2 > t_0 + t_1$, after $f(t)$ has changed signs in response to the change in potential at $t_0 + t_1$. Thus, the cue triggered at $t_0 + t_2$ will be the same sign as the cue triggered at t_0 . A new cue of the opposite sign will not occur until the ensemble has equilibrated ($f(t) \approx 0$), and a fluctuation in the sign of $f(t)$ coincides with a time when a measurement is taken. The velocity decreases with increasing t_1 , due to increased time spent waiting for fluctuations in $f(t)$ (fig. 4.5(a)).

In a feedback system with $t_2 < t_1$, a new measurement is taken before the previous measurement has been implemented. This is analogous to a Maxwell's demon that "multi-tasks", continuing to pay attention to the particle bath at the same time as opening and shutting the gate. This could be accomplished in an experiment by collecting information about the system with one set of software and passing this information to a different program for information processing, allowing the data acquisition system to continue taking new measurements.

In a feedback-controlled ratchet with $0 < t_2 < t_1$, the stable oscillatory mode for the system depends on whether t_1 is an integer multiple of t_2 . In general, if a cue at t_0 is implemented at $t_0 + t_1$, the next measurement (taken at $t_0 + t_2$) will be implemented at $t_0 + t_1 + t_2$, possibly reversing the implementation of the cue from t_0 . After $t_0 + t_1$, the next measurement occurs at time $t_0 + t_1 + t_2 - t_1 \text{mod}(t_2)$. If $t_1 \text{mod}(t_2) \neq 0$, this measurement takes place *before* the implementation of the measurement from $t_0 + t_2$, and will be based on the state of the system after the implementation of the cue from

t_0 . The oscillatory mode, and resulting velocity, depend sensitively on how $t_1 \bmod(t_2)$ compares with the characteristic time development of $f(t)$ in the ‘on’ and ‘off’ states.

On the other hand, if $t_1 \bmod(t_2) = 0$, the first measurement taken after $t_0 + t_1$ occurs at $t_0 + t_1 + t_2$. The implementation of a measurement taken at $t_0 + t_2$ also takes place at $t_0 + t_1 + t_2$. This interferes with the advantageous synchronization induced by implementation delay in the absence of measurement delay, effectively slowing the period of oscillation. Consider, for example, the case $t_2 = 0.5t_1$: Every other measurement results in a cue to change the potential, yielding an oscillatory mode with $t_{on} = 0.5t_1$ and $t_{off} = t_1$ (shown for $t_1 = 0.05L^2/D$ in figs. 4.6(b) and 4.7(b)). For this mode, a value of t_1 can be chosen that produces higher velocity than in the absence of delay, but this velocity falls short of the optimal velocity, v_{opt} , for a periodic flashing ratchet with $t_{on} = t_{off}$ (fig. 4.5(a)).

Experimental Feasibility

Two experimental Brownian ratchet systems have been constructed by Brian Long and Benjamin Lopez in the Linke laboratory, which could be used to experimentally test the role of time delay in feedback control. Detailed discussions of the experimental design and implementation will be presented elsewhere [51, 119]. Below is a discussion of the sources of time delay in each experiment, and the relevant time scales for experimentally testing the computational results discussed in this chapter. These comparisons between theory and experiment were developed collaboratively in group

discussions, and technical information about the experiments was provided by Brian and Ben.

Experimental feedback ratchet for many particles:

An experimental system based on the flashing ratchet concept has been constructed by Brian Long with the goal of realizing and testing ratchet transport for charged, colloidal particles in a fluid. A periodic, asymmetric potential is generated using an interdigitated electrode array. The potential can be turned on and off using a function generator, either supplying a periodic input function for open-loop control, or using measured bead distributions to implement closed-loop control (feedback). Feedback control of this system would require: (1) acquisition of an image of the bead distribution using a CCD camera; (2) determination of bead locations using image analysis software that detects bright regions in the image; (3) decision whether to switch the potential; and (4) implementation of the decision to switch the potential (i.e. change in applied voltage). In this case, the implementation delay, t_1 , is equal to the total time needed for steps (1)-(4). The measurement delay, t_2 , roughly corresponds to the camera exposure time (step (1)), although in practice the particle positions are averaged over the exposure time rather than collected instantaneously as in the computational study.

Feedback schemes using a similar setup to control the position of a single fluorescent particle have been implemented with frequencies as high as 300 Hz [120]. This suggests that an implementation delay on the order of $t_1 = 10ms$ is realistic for small N .

This yields $t_1 < 0.01L^2/D$ when $L > 1.2\mu m$ for beads of diameter $d = 300nm$ (where $D = kT/3\pi\eta d$, and $\eta = 10^{-3}Pa \cdot s$). Fluorescent beads of this diameter can be tracked with a CCD camera, and electrode arrays with a spatial period of $L \approx 1\mu m$ can be fabricated using standard lithography techniques. In the previous section, simulations demonstrate that a feedback-controlled ratchet performs better than a periodic ratchet for a small number of particles and $t_1 < 0.03L^2/D$. Enhanced velocity due to feedback control of a small ensemble could in principle be achieved with this system.

For a larger number of particles, a larger image (more pixels) would need to be analyzed. The exposure and readout time (step (1), above) for a high-sensitivity CCD camera is estimated to be on the order of $30ms$ for an image containing $N \approx 10^2 - 10^3$ particles. If information processing (steps (2)-(4), above) are performed while the next image is collected by the camera, total delays of order $t_1 = 2t_2 \approx 60ms$ are realistic. Based on this lower bound for the implementation delay, it is possible to tune t_1 in the range $0.01 - 0.1L^2/D$ by using approximately $300nm$ beads and an electrode array with a spatial period of about $L = 3\mu m$.

The time scale L^2/D can be easily tuned in the experiment by using beads of different diameter, to explore the behavior of the system on different relative time scales. In water, the $300nm$ polystyrene beads used in this experiment have a charge $q \approx 10^5e$, which means that an electrostatic potential in the $100mV$ range could create a potential depth much larger than kT . In principle, the computational results

presented in this chapter could be tested using this experimental setup. In practice, electrostatic screening and motion of the fluid create a more complicated system, and analysis of these effects is needed to establish the exact relationship between this experiment and simulations of a much simpler flashing ratchet system (B. R. Long, dissertation [119]).

Experimental feedback ratchet for a few particles:

An advantage of the experimental system described above is that it enables transport and tracking of a large number of particles. However, a disadvantage is that the complicated nature of electrostatics in a fluid make this a difficult system to analyze. An alternative experimental ratchet system has recently been constructed by Ben Lopez, and the first experimental realization of feedback control in a flashing ratchet has been performed [51]. In this case, a ratchet system for small particle numbers is achieved using a scanning line optical trap [52–55]. By using an acousto-optic deflector (AOD) to quickly scan an optical tweezer in one dimension, a quasi-one-dimensional linear trap is created in which a particle feels a time-averaged potential in the direction of scanning and strong trapping forces in the other two dimensions. If the light intensity and the scan speed are kept constant, this creates a “flat” potential in which the bead diffuses freely along the scan line. Tailored potential profiles, such as a sawtooth ratchet potential, can be created by varying the light intensity during the scan. Feedback control can be implemented by switching between potential profiles based on measurements of the beads’ positions. With 1W of output laser power, it is

possible to create a stable line trap up to $40\mu m$ for a $1\mu m$ silica bead [18]. With this setup, it is possible to create up to about ten spatial periods of a ratchet potential, which allows experimental implementation of a feedback-controlled ratchet for a small number of particles.

The minimum implementation delay, t_1 , for this experiment is limited by the time it takes for image analysis software to determine the particle positions and the time for the function generator to switch waveforms, and a delay of at least $t_1 = 4ms$ is estimated. The frame rate of the camera limits the minimum measurement delay to at least $t_2 = 10ms$. For a dielectric bead with diameter $d = 0.9\mu m$ in a potential with spatial period $L = 2\mu m$, the inherent time delays are small enough that the computational results in this chapter can be tested experimentally by tuning the implementation delay over the range $t_1 = 0.01 - 0.1L^2/D$.

This experiment confirms the theoretically predicted increase in velocity for feedback control of one to four particles, compared with the performance of a periodic flashing ratchet. A sample of Ben's experimental data is shown in fig. 4.8 (which will appear in [51]), demonstrating that the velocity of a single particle in this experimental ratchet matches the theoretical predictions for both closed- and open-loop control. The slightly smaller velocity for experimental closed-loop control compared with the theoretical prediction (based on $t_1 = t_2 = 0$) may be the result of a small implementation time delay in the experiment.

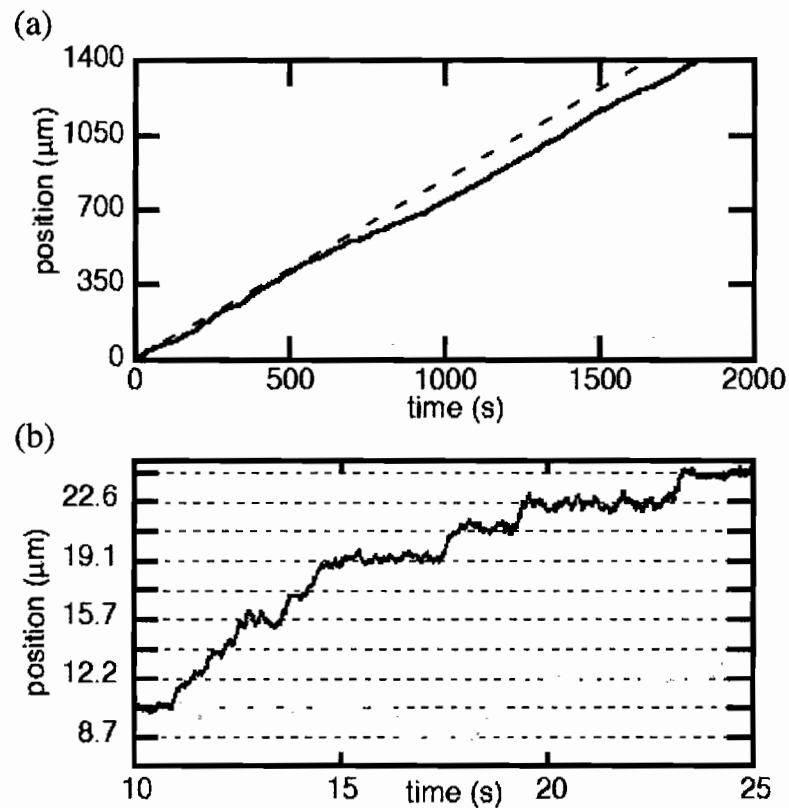


Figure 4.8. Feedback control: comparison between theory and experiment. Sample data for one bead in a feedback-controlled optical flashing ratchet (to appear in Lopez et al.[51]): (a) An example of optimal periodic (gray) and feedback-controlled (black) ratcheting trajectories. The dashed line indicates the theoretical prediction for feedback control. (b) A sample of a shorter time series from the data in (a) is shown. Dashed horizontal lines indicate spatial periods of the ratchet potential.

In this dissertation, theoretical and computational predictions have been used to model two factors that modify the performance of an experimental ratchet system: the decrease in asymmetry due to the finite size of the bead (discussed in chapter III), and inherent time delay in feedback control. We find that the velocity of the experimental feedback-controlled ratchet can be significantly increased by taking these factors into account in order to optimize the feedback protocol. An optimization strategy is discussed in detail in Lopez et al. [51].

Concluding Remarks

In this chapter, we have investigated the role of time delay in feedback control of a flashing ratchet. Two types of time delay were considered: implementation delay and measurement delay. For small particle numbers, we show that the increase in velocity through closed-loop control falls off as a function of implementation delay. The improvement gained from feedback control is lost if the delay is longer than approximately the time it takes for a particle to diffuse the length of the shorter segment of the ratchet potential on average. This is related to the prediction that there is a fundamental upper bound on the increase in flux due to feedback control, which is limited by the accuracy of the information available for feedback [76]. For large particle numbers, we find the somewhat counter-intuitive result that a finite time delay can increase the velocity of a feedback controlled ratchet. This works by allowing the system to synchronize into a quasi-stable periodic mode that matches

the behavior of a periodic flashing ratchet or a feedback controlled ratchet with thresholds [74] (discussed in chapter I, see fig. 1.3). We discuss the sources of time delay in two experimental flashing ratchet systems, and conclude that it is realistic to experimentally observe the theoretically predicted increase in velocity for closed-loop control. Theoretical predictions about the role of time delay in feedback control have proven essential to analyzing results from the scanning line optical trap ratchet discussed above.

CHAPTER V

MECHANICAL MODEL FOR MYOSIN-V WALKING MECHANISM

Introduction

Myosin-V is a biological molecular motor that transports various cargoes through eukaryotic cells. Experiments that track the motion of one or both neck domains have demonstrated that myosin-V walks along actin filaments in a ‘hand-over-hand’ mechanism, in which the binding domains (heads) alternate between the trailing and leading positions [2, 88, 89]. In chapter I, an overview of the experimental investigation of the myosin-V walking mechanism is given in terms of progress toward answering the following two mechanistic questions: (1) How does the trailing head become the leading head? (2) How is the stepping coordinated? Although the answers to these questions are not understood in detail, a variety of experimental studies support the following qualitative model: Two heads bound to actin are coordinated through intramolecular strain that makes the trailing head more likely to detach. When the trailing head detaches, the leading neck domain relaxes from a strained conformation to an unstrained conformation, which leads to an average motion in the direction of motility that biases the position of the detached head toward a “forward”

binding site. The detached head undergoes biased tethered diffusion until it reattaches to a binding site along actin.

Here, we present a mechanical model for myosin-V in order to establish a detailed quantitative test of this proposed mechanism. We develop a coarse-grained mechanical description of the motor's structure intended to capture the essential physical features of its behavior. We constrain the mechanical input parameters by comparing the equilibrium conformation of the motor in distinct mechano-chemical states with information from experiments. Then, we propose an experimentally motivated and testable model for how intramolecular strain may lead to a kinetic asymmetry in the binding affinities of the two heads. Experiments that could test this proposed mechanism are discussed. We study the dynamics of the biased tethered diffusion of the detached head over a range of mechanical parameters, and test the ability of the motor to step forward when a load force is applied to the end of the attached neck domain. Stepping behavior of the motor is modeled with Brownian dynamics simulations of the motion of the motor as each head cycles stochastically through a predominant chemical pathway (based on biochemical experimental studies of myosin-V). The model provides a tool that can help interpret the results of single molecule experiments, and possibilities for ongoing research with this model are discussed in chapter VI.

The model presented here builds on the insights of some previous models for myosin-V. For example, Kolomeisky et al. [121] have developed a kinetic model for the chemical cycle of myosin-V that incorporates force-dependent transition rates in

order to study strain-dependent coordination of the steps. In this model, the motor heads are treated as points that undergo stochastic transitions between chemical states that couple to discrete steps along the one-dimensional track. Quantities such as the average velocity of the motor are determined by obtaining steady state solutions to the discrete master equations that describe the probability to find the motor in any mechano-chemical state at a given time [122]. Force dependent transition rates are modeled phenomenologically in the form: $k = k_0 \exp(-QFd/kT)$, where F is the applied force, d is a characteristic distance over which the force is applied, and Q is a “load distribution factor” that implicitly contains mechanical properties of the motor that determine how a load at the end of a neck domain translates into a change in the biochemical transition rates at the motor head. These types of discrete, kinetic models provide valuable insight into the chemical cycle of the motor, and have been useful for interpreting measured force-velocity curves by fitting the model parameters to the experimental curves.

In contrast to simpler kinetic models, our study explicitly considers the mechanical properties of the motor, in order to learn about how specific mechanical features of the molecule impact the dynamics of the mechano-chemical cycle. For example, instead of including a parameter Q to encompass assumptions about how the applied force at the end of a neck domain couples to the biochemical transition rates of the head, we simulate the mechanics of how load applied in one part of the motor changes the local conformation elsewhere. We propose a coordination mechanism in which the

ADP release rate from the head depends on the angle of attachment between the head and the adjacent neck domain. The instantaneous conformation of the motor, and the resulting ADP release rate from each head, are outputs rather than inputs of the model.

Two other recent models have treated the neck domains of myosin-V as elastic filaments [123, 124]. A model presented by Andrej Vilfan [123] treats the neck domains as continuous elastic rods with fixed attachment angles that depend on the chemical state of the head. He calculates the elastic strain for different conformations of the motor to demonstrate certain constraints on the stepping properties of the motor, for example concluding that there is a high energy cost and therefore a low probability for a detached head to reattach as the leading head before the other head undergoes a power stroke. By contrast, our model does not assume fixed attachment angles between the head and neck domains, and instead treats the head-neck junctures as semi-flexible joints with an elastic energy cost to bending away from a state dependent preferred angle. This allows us to model the role of thermal motion in the transitions between mechanical conformations of the motor in response to chemical transitions. In this sense, whether the attachment angle of the neck domain is tightly or loosely coupled to the chemical state of the head is an output rather than an input of our model.

Lan et al. [124] treat the neck domains as semi-flexible filaments with state-dependent preferred angles for the head-neck junctures. They calculate conformation-

dependent elastic energies to predict binding and unbinding probabilities for the motor. Following the example of Lan et al., we choose to treat the neck domains as semi-flexible filaments. However, their study excludes dissociation events and adds an energy term to prevent the motor from binding with the head domains closer than the experimentally observed separation of $\approx 36nm$. In contrast, dissociation events are an important output of our model that allow us to determine how the mechanical properties of the motor impact the number of steps it takes on average before detaching. At present, we impose a $36nm$ step size by providing discretely-spaced binding sites in one direction, but the model could be generalized in the future to allow binding at other positions. In this case the step size distribution would be an output of the model that would depend on the neck domains length, and the stiffness of neck domains and the head-neck junctures.

Predominant Mechanochemical Cycle

Each head of myosin-V has a binding site for a nucleotide and a site for binding to actin, which means there are eight possible states for the head (**Actin:** attached or detached; **Nucleotide:** ATP , ADP , $ADP \cdot Pi$, or empty) and 64 possible states for a dimer. We restrict our theoretical treatment of the myosin-V cycle to the relatively long-lasting states on the time scale of experimental observations of motor transport, and allow each head to cycle stochastically through the following six kinetic states (fig. 5.1): (1) ATP bound, and attached to actin; (2) ATP bound, and detached from

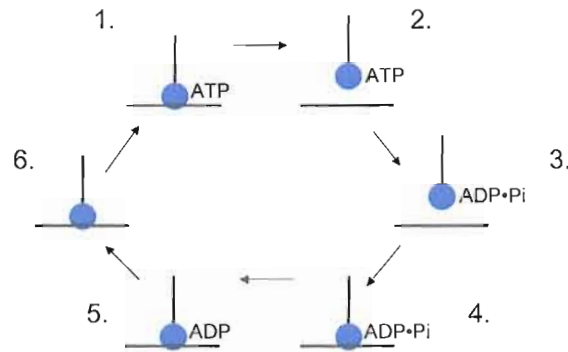


Figure 5.1. Schematic: predominant mechano-chemical cycle for a myosin-V monomer. We restrict our theoretical treatment of the mechano-chemical cycle for a myosin-V monomer to relatively long-lasting states, based on biochemical measurements [97].

actin; (3) ADP ·Pi bound, and detached from actin; (4) ADP·Pi bound, and attached to actin; (5) ADP bound, and attached to actin; and (6) No nucleotide bound, and attached to actin. The transition rates for this cycle are summarized in table 5.1.

In fig. 5.2, we summarize a qualitative model for the dominant kinetic path for a myosin-V dimer, which is presented by Rief et. al. [90] based on a compilation of experimental observations of the mechano-chemical cycle of the dimeric motor. Beginning in the top left corner of the figure, both heads are attached to actin with ADP bound (i.e., in monomeric kinetic state 5). The leading head stays in state 5, while the trailing head dissociates ADP, binds ATP, detaches from actin, and reattaches as the new leading head after hydrolyzing ATP. Although we do not explicitly enforce this mechano-chemical cycle for the dimer in our theoretical model, this cycle for the dimer is an outcome of the predominant cycle for a monomer (fig. 5.1) if certain mechanical requirements are met: (1) The leading head is more likely to

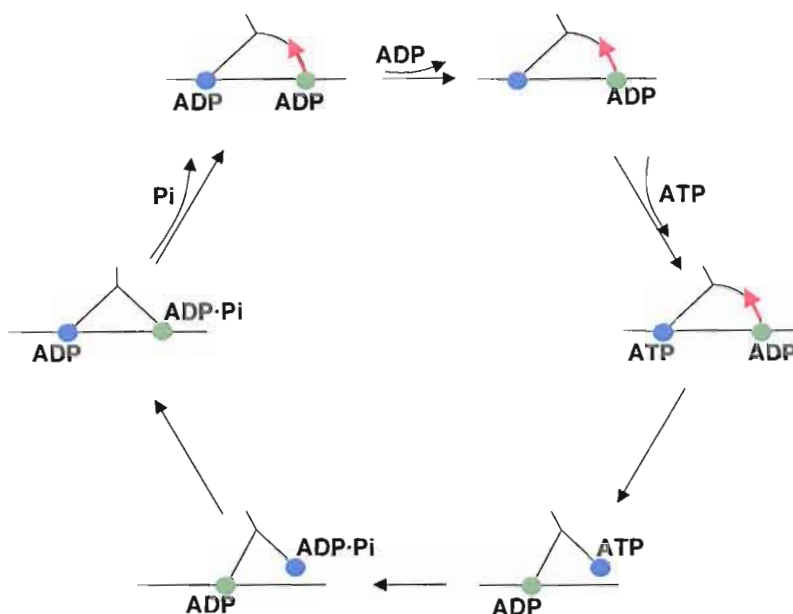


Figure 5.2. Schematic: predominant mechano-chemical cycle for a myosin-V dimer, according to model proposed in Rief et al. [90]

dissociate ADP than the trailing head; and (2) When a head detaches, it is most likely to reattach as the leading head. It is widely thought that ADP release is either slowed from the leading head or accelerated from the trailing head through coordination via intramolecular strain, although there is not a consensus about the exact mechanism. The motion of a detached head to become the new leading head is thought to occur either through a conformational change, biased diffusion, or some combination of the two.

The next section outlines structural assumptions we will make in order to develop a minimal mechanical model for myosin-V. Simulations of this mechanical model in the context of the predominant kinetic pathway for a monomer will be used to study how the mechanical properties of each mechanical state will impact the underlying

kinetic cycle for the dimer. We will specifically address the questions of how the trailing head becomes the leading head, and how the kinetic cycles of the two heads are kept out of phase.

Table 5.1. Kinetic Rates for the Chemical Transitions of a Myosin-V Head

Rate	Value used	Source
k_{12}	Faster than experimental temporal resolution. For simulations: dt^{-1} .	De La Cruz, 2000 [97]
k_{23}	$700s^{-1}$	De La Cruz, 2000 [97]
k_{34}	Diffusion limited: not an input parameter	
k_{45}	$200s^{-1}$	Baker, 2004 [109]; De La Cruz, 2000 [97], (measured for monomer)
k_{56}	$12 - 16s^{-1}$	De La Cruz, 1999, [106]; Purcell, 2005 [110]
k_{61}	$0.9 - 1.6\mu M^{-1}s^{-1}$	De La Cruz, 1999 [106], Yengo, 2002 [125]; Yengo, 2004 [126]

Structural Assumptions for Minimal Mechanical Model

The neck domain of myosin-V consists of a protein chain called the heavy chain which is made up of six tandem elements called IQ motifs [81, 127–130]. These motifs provide binding sites for smaller protein chains called light chains, which bind in compact configurations to the IQ motifs, adding rigidity to the neck domain. A model of the neck domain based on the crystal structure, combined with fluorescence resonance energy transfer (FRET) measurements of distances between IQ complexes,

suggests that the neck domain can be thought of as three pairs of strongly interacting IQ motifs, with minimal interaction between adjacent pairs, allowing bending primarily at these junctures (Terrak et al., 2005 [129]). Based on this structural model, we treat each neck domain as a filament made of three rigid segments with bending allowed at their junctures (fig. 5.3(a)).

Based on electron microscopy images [103, 112], we treat the juncture between each head and the adjacent neck domain (points 2 and 8 in fig. 5.3(a)) as a semi-flexible joint with a preferred angle that depends on the chemical state of the head. We assume that a forward rotation in the preferred angle (from θ_A to θ_B) between head and neck is tightly coupled to phosphate release from the head (fig. 5.3(b)).

Electron microscopy (EM) photos [103] and observations of the motion of the detached neck domain by tracking an attached gold nanoparticle [100] or a microtubule filament [105] support a model in which a detached head and its adjacent neck domain undergo tethered diffusion about the juncture between neck domains, with free rotation about this joint (point 5 in fig. 5.3(a)).

We make the simplification of treating the actin filament as a one-dimensional array of evenly-spaced binding sites with separation $L = 36nm$. This is a reasonable simplification because the measured step size distribution for myosin-V suggests that it walks along one side of an actin filament, binding at discrete positions, as discussed in chapter I. Later, the model could be extended to include a more realistic three-

dimensional actin filament in order to simulate the stepping behavior of myosin-V with different neck lengths (see outlook discussion in chapter VI).

We simulate attachment of a head to actin by assuming that if it is in a chemical state with high actin affinity and diffuses close enough to a binding site to interact with it electrostatically, it will attach to this site. In the simulations, this is implemented through a rule that if the head is in kinetic state 3 (fig. 5.1), and comes within a distance R_{screen} of a binding site, the position of the head is fixed at the location of the binding site and the kinetic state of the head is changed to state 4 (bound to actin and $ADP \cdot Pi$). For the input parameter R_{screen} , we choose the Debye length for electrostatic screening in water, $R_{screen} = R_{Debye} \approx 0.6nm$ [131], which sets the realistic upper bound for the distance at which electrostatic interactions can occur in a fluid.

Semi-flexible Polymer Model for Myosin-V Neck Domains

Based on the structural assumptions discussed above, a quantitative formalism for describing a coarse-grained model for the structure of myosin-V is introduced in this section. This coarse-grained model is intended to capture the essential physics of the mechanical behavior of myosin-V by incorporating the key observations described in the previous section, namely: The neck domains are semi-flexible filaments with bending allowed primarily at two joints along each neck domain; the joint between the two neck domains can be treated as a free swivel; and the preferred attachment

angle between a head and an adjacent neck domain depends on the nucleotide state of the head.

The neck domains are treated as semi-flexible filaments based on the following model for the statistical behavior of an elastic polymer [70], in which the filaments are treated as a chain of evenly-spaced points with semi-flexible rotation about each point (fig. 5.3(a)). The potential energy of the molecule due to conformational strain is given by

$$U = \frac{1}{2} \sum_{i=2}^8 V_i \left(\cos \phi_i(t) - \cos \phi_i^{pref} \right)^2 \quad (5.1)$$

where ϕ_i is the angle between filament segments that meet at point ‘i’. This is the sum of elastic energy for rotation away from a preferred angle for each point (excluding the end-points). These elastic energy terms can be referred to as three-body interactions, because they involve an interaction of three points: For example, the elastic energy associated with the point 4 in figure 5.3(a) will result in a force on points 3, 4, and 5 (see Appendix A).

The stiffness, V_i , and the preferred angle, ϕ_i^{pref} , for each joint are model input parameters based on experimental observations. For the junctures between adjacent neck domain segments (points 3, 4, 6, and 7 in fig. 5.3(a)), the preferred angle is $\phi_i^{pref} = \pi$, meaning that the potential energy of the neck domain is minimized when the filament is straight. The stiffness, $V_i = V_{NN}$, of the joints in the neck domain is related to the polymer persistence length l_p by $V_i = 2l_p kT / L_N$, where L_N is the length

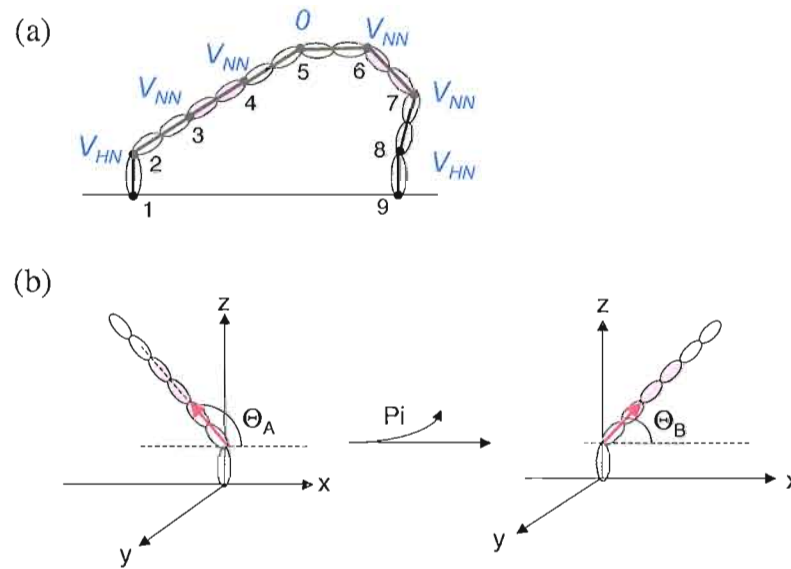


Figure 5.3. Schematic of mechanical model for myosin-V. (a) The myosin-V molecule is modeled as a semiflexible polymer with elastic potential energy associated with rotation away from a preferred angle for each joint. The points, labeled 1 – 9, will experience forces due to the internal elastic potential energy defined by equation 5.1. The segments 1 – 2 and 8 – 9 represent the head domains. The segments 2 – 5 and 5 – 8 each represent a neck domain. Point 5 represents the neck domain juncture. The stiffness parameter V_i for each joint is based on the structural assumptions about myosin-V discussed in the text. (b) The preferred attachment angle of the head-neck junctures (points 2 and 8 in part (a)) is defined with respect to the x-axis in the $y = 0$ plane. The preferred angle before phosphate release is θ_A , and the preferred angle after phosphate release is θ_B .

of each rigid segment. The persistence length of a polymer is defined as the distance along its contour length at which the direction is no longer correlated [116, 132].

As mentioned in the previous section, we assume that each head-neck juncture has a preferred angle with respect to the x-axis (i.e., the actin filament) when the head is attached to actin, and that there is an elastic energy associated with rotation away from this preferred angle in any direction. In other words, there is elastic resistance at this joint to bending out of the $y = 0$ plane, as well as elastic resistance to bending away from a preferred angle in the $y = 0$ plane. We introduce the parameters θ_A and θ_B for the preferred angles before and after phosphate release, respectively (fig. 5.3(b)). The stiffness associated with the elastic energy for bending away from the preferred angle at a head-neck juncture is called $V_i = V_{HN}$. Note the difference in notation: θ_A and θ_B are defined with respect to the x-axis, rather than with respect to the previous segment of the chain. For a more detailed description of how the force on each point is calculated for this mechanical model, please see Appendix A.

Combined Mechano-chemical Simulations

In this study, we use Brownian dynamics (BD) simulations to investigate a combined mechano-chemical model, in which the internal forces are based on the polymer model above (equation 5.1), and the chemical state of each head cycles stochastically through the predominant chemical cycle illustrated in fig. 5.1. The chemical transitions are enacted in the simulations by allowing the heads to transition from one state to the

next probabilistically. For example, if a head is in kinetic state 1, in each time step of the program it will have a probability $k_{12}dt$ to transition from state 1 to state 2, where dt is the magnitude of the time step and k_{12} is rate of the transition. The time step dt must be selected such that $k_{12}dt \leq 1$. The decision to change states is made in each time step by comparing a randomly selected number with the pre-defined switching probability. The transition rate from kinetic state 3 to state 4, however, is diffusion-limited: We assume a head in state 3 will reattach to actin (i.e., switch to state 4) when it is within binding range ($R < R_{screen}$) of a binding site, as described above in the “Structural assumptions” section.

When a head is in one of the ‘attached’ kinetic states (1, 4, 5, and 6), we hold the position of the head fixed at the point of attachment along the actin filament, with the head oriented perpendicular to the filament. When a head is in one of the ‘detached’ kinetic states (2 and 3), it is allowed to undergo tethered diffusion. Kinetic state 4 (attached with $ADP \cdot Pi$ bound) has a preferred head-neck angle θ_A . After phosphate release (kinetic states 5, 6, and 1), the preferred attachment angle is θ_B .

An outcome of the mechano-chemical model is that the dimeric motor typically cycles through three distinct *mechanical* states as each head undergoes kinetic state transitions. The mechanical states, illustrated in fig. 5.4, are: (I) Both heads attached; trailing head with θ_B , leading head with θ_A ; (II) Both heads attached with θ_B ; (III) One head attached with θ_B . It is also possible to find the motor in a state with both heads attached to actin with preferred angle θ_A , but this happens rarely since the

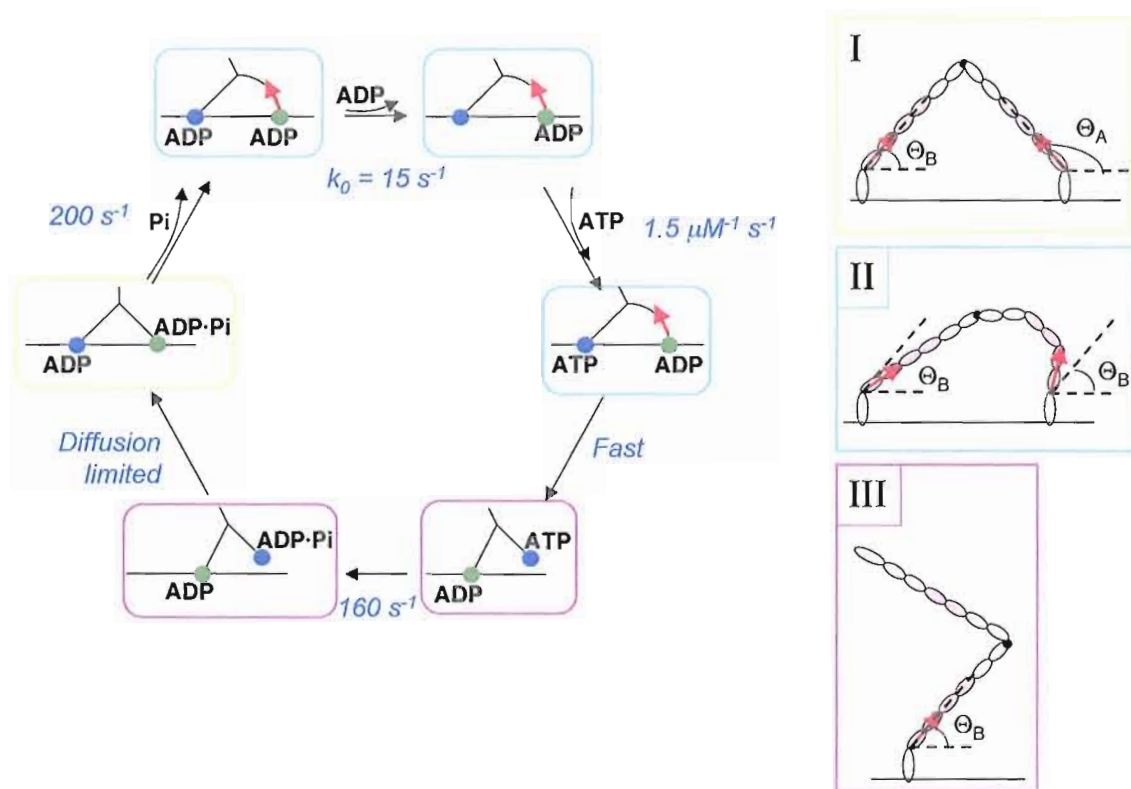


Figure 5.4. Mechanical states for a myosin-V dimer. A myosin-V dimer typically cycles through three distinct mechanical states (within the framework of our model) as each head undergoes kinetic state transitions: The schematic above illustrates these *mechanical* states (right), and the corresponding *kinetic* states (left). Color-coded boxes indicate the correspondence between mechanical states and kinetic states.

attached head has usually released phosphate (thus, transitioning $\theta_A \rightarrow \theta_B$) by the time a detached head reattaches.

Choice of Input Parameters

In the previous sections, a mechano-chemical model for myosin-V is introduced based on the predominant chemical cycle observed for each head (fig. 5.1) and experimentally motivated structural assumptions about the mechanical properties of the motor. In the previous section, the approach to simulating this mechano-chemical model is described. Most of the mechanical input parameters can be fixed based on experimental values, which are summarized in table 2. Several less-constrained parameters that may have an important role in the stepping mechanism will be varied in order to test their impact on performance features of the model. These parameters are discussed in this section.

The input parameters, θ_B , V_{NN} , and V_{HN} are not tightly constrained by experimental measurements, and they impact several important performance features of the mechanical model. In this study, all other parameters are fixed according to experimental estimates (table 5.2), and these three parameters are varied in order to evaluate their impact on the following performance features: the average motion of the motor during a step, the stall force, the coordination of stepping, the run length before detachment, and the velocity. Table 5.3 summarizes experimental measurements of

these performance features. Below, we discuss what can be inferred about the stiffness and preferred angle parameters from experimental measurements.

Neck domain stiffness, V_{NN} : For the junctures between adjacent neck domain segments (points 3, 4, 6, and 7 in fig. 5.3(a)), the preferred angle is $\phi_i^{pref} = \pi$, meaning that the potential energy of the neck domain is minimized when the filament is straight. Estimates of the persistence length of myosin-V neck domains in the literature vary over a wide range ($l_p = 100nm - 400nm$, corresponding to $V_{NN} = 20kT - 80kT$ for $L_N = 10nm$) depending on the experimental method [123]. Although the experimentally supported range is quite broad, all of the estimates indicate that the persistence length is higher than the total length of a neck domain ($30nm$). In this regime, a polymer is fairly rigid and its conformation does not fluctuate a lot in response to thermal noise. For example, for a myosin-V neck domain with $l_p = 100nm$, which corresponds to $V_{NN} = 20kT$, bending a joint away from its preferred angle by $\pi/2$ increases the potential energy stored in strain by $10kT$ (eq. 5.1). This will happen on occasion in response to thermal fluctuations, but not frequently. We vary V_{NN} to examine the role of neck domain stiffness in the myosin-V walking mechanism.

Preferred angle of attachment after phosphate release, θ_B : Several performance features of the motor that involve mechanical states II and III are likely to depend on θ_B , including the stall force and the dynamics of the step after a head detaches. Below, we test the dependence of these performance features on θ_B in order to constrain this

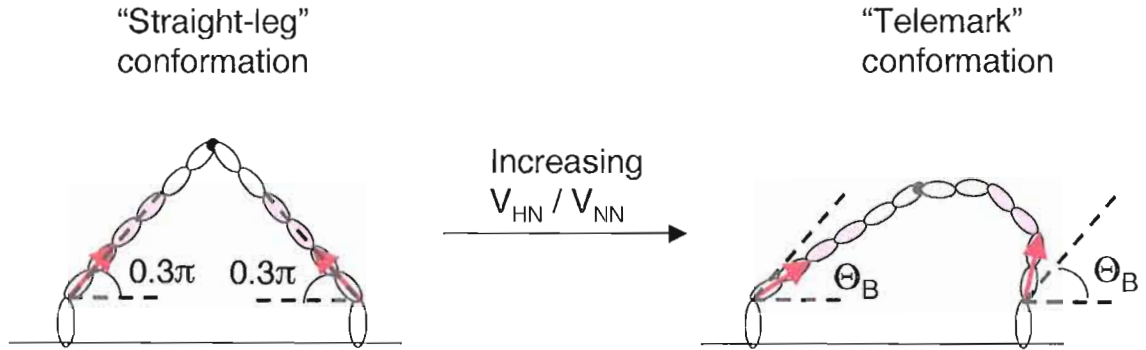


Figure 5.5. Schematic: dependence of conformation on filament stiffness. The ‘straight-leg’ and ‘telemark’ conformations for the motor in mechanical state II are illustrated above, as described in the text. The motor is likely to have a ‘straight-leg’ conformation for high V_{NN}/V_{HN} , where the elastic potential energy for bending the neck domains is substantial. For high V_{HN}/V_{NN} , such that the elastic energy for rotation of the head-neck junction is most significant, the motor is likely to have a ‘telemark’ conformation.

parameter and to study how the average conformations sampled by the motor impact its progression through the mechano-chemical stepping cycle.

Head-neck junction stiffness, V_{HN} : This parameter has not been measured experimentally for myosin-V, and would be difficult to test directly because this would require decoupling the stiffness of the head-neck region from that of other parts of the protein in analyzing the response of myosin-V to an external force. In the next section, we will vary this parameter to test its impact on performance features of the model.

The ratio V_{NN}/V_{HN} determines the conformation that minimizes the potential energy (eq. 5.1) for fixed values of the attachment angles. In mechanical state II, for a large value of V_{HN}/V_{NN} , the motor has an average forward-leaning ‘telemark’ conformation with $\langle \theta_{trail} \rangle \approx \langle \theta_{lead} \rangle \approx \theta_B$ (fig. 5.5), where θ_{trail} and θ_{lead} denote

the attachment angles of the trailing and leading neck domains respectively. In the high V_{NN}/V_{HN} limit, the motor has on average a ‘straight-leg’ conformation with $\langle\theta_{trail}\rangle \approx 0.3\pi$ and $\langle\theta_{lead}\rangle \approx 0.7\pi$, such that the neck domains are not bent (fig. 5.5). As we will discuss in the following sections, the average conformation in state II can impact mechanical behavior important to the stepping function of the motor, such as the average motion after a head detaches and the manner in which the detachment cycles of the two heads are coordinated.

Average Motion During a Step: Comparison with Experiments

Although many of the mechanical and kinetic parameters of the model are well-constrained by experiments, the values of several important mechanical parameters are not known, as discussed in the previous section. In this section, we attempt to constrain the parameters θ_B , V_{NN} , and V_{HN} by comparing the equilibrium conformation of the motor in distinct mechano-chemical states with information from experiments. Specifically, we calculate the average movement of the juncture between neck domains (point 5 in fig. 5.3(a)) when the motor changes from mechanical state II to mechanical state III (fig. 5.4), allowing the leading neck domain to relax from a strained conformation. This predicted motion is compared with the first characteristic phase of experimentally measured two-phase step averages, often interpreted as the movement due to the relaxation of the leading neck domain after the trailing head detaches.

Table 5.2. Mechanical Parameters

Parameter	Definition	Value used	Source
θ_A	Preferred angle before P_i release	0.72π	Forkey, 2003 [108]
θ_B	Preferred angle after P_i release	Varied to test performance	Estimates in Forkey, 2003 [108]; Burgess, 2002 [103]
V_{NN}	Neck domain stiffness	Varied to test performance	Estimated range: Vilfan, 2005 [123]
V_{HN}	Stiffness of head-neck junctures	Varied to test performance	
V_5	Stiffness of juncture between neck domains	$0kT$	Dunn, 2007 [100]; Shiroguchi, 2007 [105]
L_H	Head domain length	$5nm$	Approximation based on Liu, 2006 [133]
L_N	Length of neck domain segments (two IQ motifs)	$10nm$	Moore, 2001 [84], Veigel, 2002 [85]
L	Distance between binding sites	$36nm$	[2, 82, 90, 112]
γ_H	Drag coefficient of a head domain (assigned to points 1 and 9)	$6.2 \times 10^{-8} pNs/nm$	Stoke's Law, assuming head is a sphere with diameter L_H
γ_N	Drag coefficient assigned to points along neck domains (points 2-8)	$4.1 \times 10^{-8} pNs/nm$	Calculated [1] assuming each neck domain is a cylinder of length $30nm$ and diameter $2nm$ [133]
R_{screen}	Reattachment occurs for head within R_{screen} of binding site.	$R_{screen} = R_{Debye} = 0.6nm$	Cordova, 1992 [131]

Table 5.3. Performance Features

Performance feature	Definition	Experimental measurement	Source
Velocity	Average velocity of a walking myosin-V	$550nm/s \pm 40nm$ for $[ATP]=1mM$ under approximately physiological conditions	Baker, 2004 [109]
Run length	Number of steps before detaching from actin	20-60 steps on average	[2, 91-93, 95, 96, 107-109]
Stall force	Load force above which the motor does not take a forward step	$1.6pN$	Capello, 2008 [98] (add other references)
“Working stroke” distance, $x_{III} - x_{II}$	Characteristic phases of step average interpreted as the motion corresponding to relaxation of the leading neck domain after the trailing head detaches	$\approx 25nm$	[84, 85, 93, 98, 100-103, 112]
“Working stroke” movement away from filament, $z_{III} - z_{II}$	Motion away from (or toward) the filament corresponding to relaxation of the leading neck domain after the trailing head detaches	$\approx 6nm$	Cappello, 2008 [98]
Kinetic asymmetry, λ	Characterizes the relative likelihood of trailing head detachment	This model prediction could be tested in future experiments.	N/A

As we will discuss in more detail below, we find that the average lateral motion is strongly dependent on the attachment angle θ_B and only weakly dependent on the stiffness parameters V_{NN} and V_{HN} . The model reproduces the experimentally measured relaxation distance parallel to the filament for $\theta_B \approx 0.4\pi$. For this attachment angle, the model also reproduces an experimentally observed average motion away from the filament during this mechanical transition if the neck domain is relatively stiff ($V_{NN} > 100kT$). Further investigation of the synchronization of motion parallel and perpendicular to the actin filament through systematic comparison between computational and experimental step averages will be necessary to constrain V_{NN} and V_{HN} with more certainty (outlook discussed in chapter VI). Below, we describe the comparison between experimental measurements and model predictions for the average motion of the motor after detachment of the trailing head. Based on the results of this section, simulations in the remainder of the chapter will use $\theta_B = 0.4\pi$ unless otherwise noted.

As discussed in chapter I, several experiments demonstrate that the average step profile of myosin-V is consistent with a two-phase model in which the cargo quickly moves about $25nm$ in the $+x$ direction after detachment, followed by a slower $11nm$ motion to complete the step [84, 85, 98, 100–102]. Also, Capello et al. [98] measure an apparent $6nm$ average motion of the cargo away from the filament ($+z$ -direction) aligned with the onset of the $25nm$ motion in the $+x$ direction. They suggest the following interpretation: When the trailing head detaches from actin, the leading

neck domain relaxes, which moves the cargo forward (+x-direction) and away from the filament (+z-direction). The motor is biased in a forward-leaning conformation, and the detached head diffuses until it reaches a binding site and reattaches to actin, completing the step.

The average motion of the cargo following detachment of the trailing head depends on the parameters θ_B , V_{NN} , and V_{HN} , as well as the length and stiffness of the tether between the cargo and the motor. For simplicity, we initially assume a stiff coupling between cargo and motor, such that the motion of the juncture between neck domains (point 5 in fig. 5.3(a)) corresponds approximately to the motion of the cargo. For the sake of comparison with the experimental measurements of Cappello et al. [98], this seems to be a reasonable simplification, because they report that the relaxation time of this linkage in their experiment is very fast compared to the time scale of the step phases.

We define the “relaxation distance” as the average displacement of the neck domain juncture due to the relaxation of the leading neck domain after the trailing head detaches. (This motion is also often referred to as the “power stroke”, the “working stroke” or the “lever arm rotation” of the motor. We choose to use the term “relaxation distance” because the dynamics of the relaxation of the motor in a new chemical state will depend on model parameters such as the neck domain stiffness. We wish to use a term that is neutral with regard to the role of this conformational change in the stepping process.) In our mechanical model, the relaxation distances

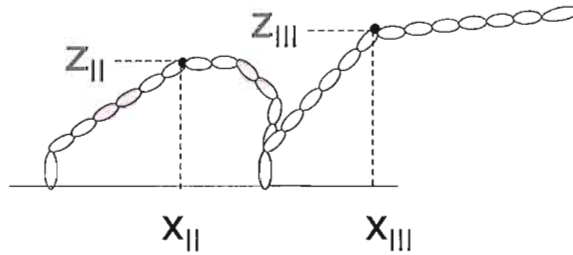


Figure 5.6. Schematic: Myosin-V “relaxation distance” after trailing head detachment, defined as the distance between the equilibrium position of the neck domain juncture in mechanical state II and mechanical state III. The x - and z -components of the relaxation distance ($x_{III} - x_{II}$ and $z_{III} - z_{II}$, respectively) may correspond to the first characteristic phase of the myosin-V step average (see text).

in the x and z directions are given by the differences in the average position of point 5 from mechanical state II to state III: $\langle x_5 \rangle_{III} - \langle x_5 \rangle_{II} \equiv x_{III} - x_{II}$, and $\langle z_5 \rangle_{III} - \langle z_5 \rangle_{II} \equiv z_{III} - z_{II}$ (see fig. 5.6).

In mechanical state III, in which the two neck domains do not exert strain on one another, the neck domains will have a straight conformation on average. Based on experimental estimates that the persistence length of a neck domain is greater than the neck domain length, it is expected that thermal fluctuations will not cause the neck domains to bend much during this state. In the absence of external load, the average position of the neck domain juncture (point 5 in fig. 5.3(a)) in mechanical state III is given with respect to the attached head as: $x_{III} = 3L_N \cos\theta_B$, $y_{III} = 0$, and $z_{III} = L_H + 3L_N \sin\theta_B$, where L_N is the length of a neck domain segment and L_H is the length of a head domain (fig. 5.7(a)).

In the simplifying limit $V_{NN} \gg V_{HN}$, the relaxation distances can be calculated based on the geometry of the ‘straight-leg’ conformation for mechanical state II (fig. 5.5), and do not depend on the parameters θ_B , V_{NN} and V_{HN} . In this case, the working stroke distances are: $x_{III} - x_{II} = 18nm + 30nm\cos\theta_B$ and $z_{III} - z_{II} = 30nm\sin\theta_B - 24nm$ (fig. 5.7(a)). For $\theta_B < 0.3\pi$, the average attachment angle rotates more than $\pi/2$ from state II to state III. This produces a large average forward motion ($x_{III} - x_{II} > 36nm$) accompanied by a movement toward the actin filament ($z_{III} - z_{II} < 0$) (fig. 5.7(b)). On the other hand, for $\theta_B > 0.3\pi$, a shorter forward movement ($x_{III} - x_{II} < 36nm$) is accompanied by a movement away from the actin filament ($z_{III} - z_{II} > 0$) (fig. 5.7(b)).

The average position of the head-neck juncture during state II is a function of θ_B , V_{NN} , and V_{HN} . As discussed above, the motor takes on a ‘straight-leg’ conformation for high V_{NN}/V_{HN} and a ‘telemark’ conformation for high V_{HN}/V_{NN} (fig. 5.5). For increasing V_{NN}/V_{HN} , x_{II} decreases and z_{II} increases, thus increasing the x-component of the relaxation distance, $x_{III} - x_{III}$, while decreasing the z-component, $z_{III} - z_{II}$.

For any choice of θ_B , the conformation that minimizes the potential energy due to strain (eq. 5.1) in mechanical state II depends on the ratio V_{NN}/V_{HN} as described above. For a given ratio V_{NN}/V_{HN} , decreasing the absolute value of V_{NN} or V_{HN} relative to kT will increase the level of conformational variation, and can shift the mean of the probability distribution away from the minimum of the potential energy landscape. The mean position, z_{II} , will decrease with increasing kT , because additional

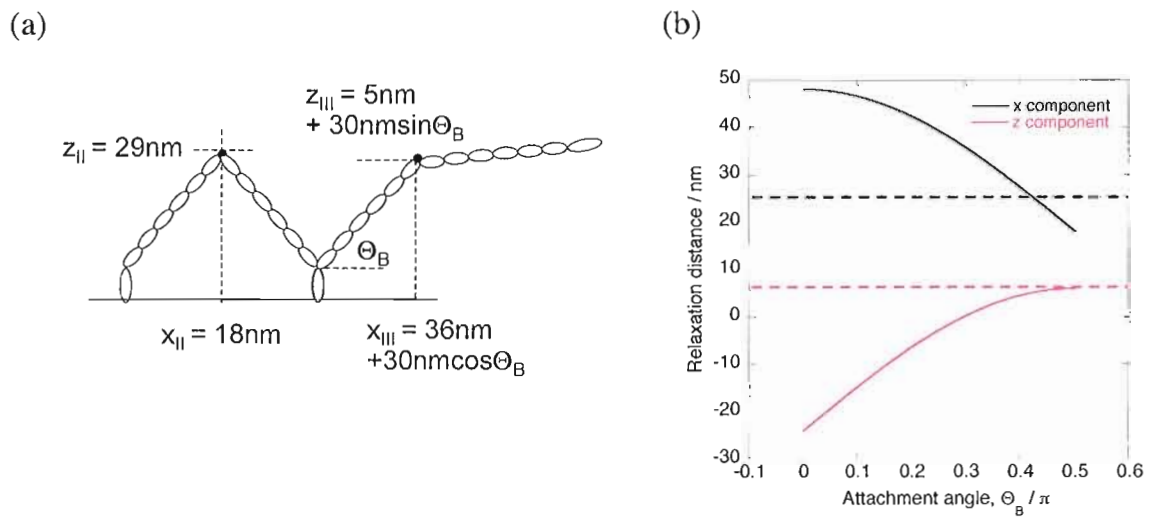


Figure 5.7. Relaxation distance in the limit of rigid neck domains ($V_{NN} \gg V_{HN}$): (a) If the neck domain stiffness, V_{NN} , is much higher than the head-neck junction stiffness, V_{HN} , then the motor has an average ‘straight leg’ conformation in state II. In this limit, the average position of the head-neck junction in state II, x_{II} , depends on the length of the neck domains and the spacing between binding sites, but does not depend on θ_B , V_{NN} , and V_{HN} . The position of the head-neck junction in state III depends on the attachment angle, θ_B . (b) The x- and z-components of the relaxation distance as a function of θ_B . Dashed lines indicate expected values based on the characteristics of experimental step averages.

fluctuations in the conformation increase the probability to find the neck domain juncture closer to the filament (lower z -position), while the finite length of the neck domains put a sharp limit on fluctuations in the $+z$ direction. However, the mean x -position of the head-neck juncture, x_{II} , is likely to depend less strongly on the absolute values of V_{NN} and V_{HN} , because fluctuations in $x(5)$ do not have such a large inherent asymmetry.

Figs. 5.8(a) and 5.8(b) show the x and z components, respectively, of the relaxation distance as a function of V_{NN}/V_{HN} for $V_{NN} = 100kT$. The average head-neck juncture positions, $x_{II}(\theta_B, V_{NN}, V_{HN})$ and $z_{II}(\theta_B, V_{NN}, V_{HN})$, are obtained from simulations of the motor in state II. As V_{NN}/V_{HN} increases from 0 to 1, $x_{III} - x_{II}$ increases by a few nm , and then the dependence starts to level off (once the neck domain stiffness is high enough to realize the ‘straight-leg’ conformation on average). The distance $x_{III} - x_{II}$ depends most strongly on θ_B . The experimentally observed $x_{III} - x_{II} \approx 25nm$ [84, 85, 98, 100–102] is predicted for $\theta_B \approx 0.4\pi$.

The corresponding distance $z_{III} - z_{II}$ decreases with V_{NN}/V_{HN} and also begins to level off around $V_{NN}/V_{HN} = 1$ (fig. 5.8(b)). It is interesting to note that for the angles that produce a longer x -direction relaxation distance (i.e., $\theta_B < 0.3\pi$), $V_{NN} < V_{HN}$ is needed to produce $z_{III} - z_{II} \approx 6nm$. On the other hand, when $x_{III} - x_{II} \approx 25nm$ as observed experimentally (and predicted here for $\theta_B \approx 0.4\pi$), an approximately $6nm$ movement away from the actin filament occurs only for $V_{NN} \geq V_{HN}$. The variation

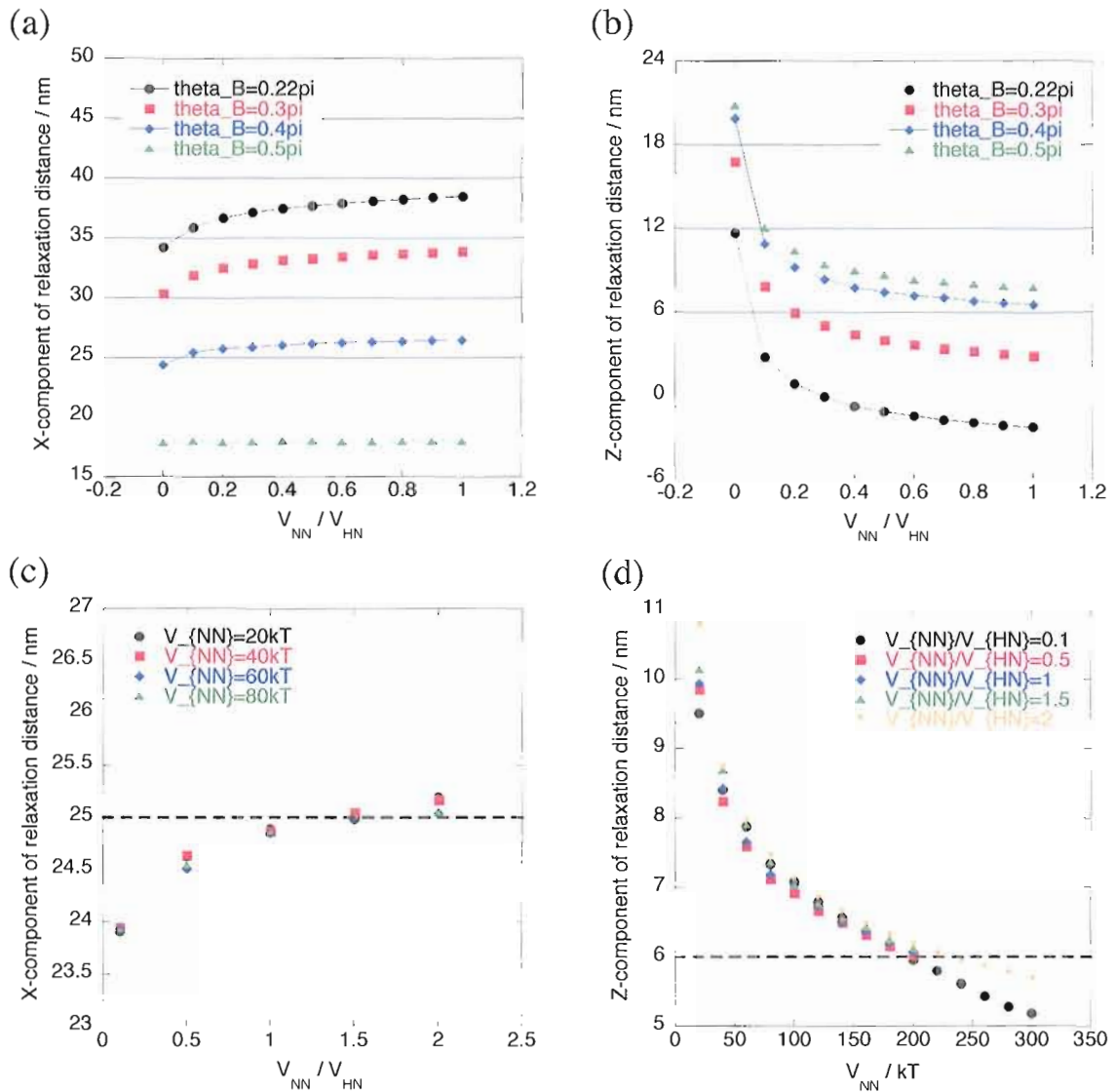


Figure 5.8. Simulations: relaxation distance as a function of mechanical parameters. (a) Relaxation distance in x-direction as a function of V_{NN}/V_{HN} for several values of θ_B . (b) Relaxation distance in z-direction based on the same simulations as in (a). (c) Relaxation distance in the x-direction as a function of V_{NN}/V_{HN} for several values of V_{NN}/kT with $\theta_B = 0.42\pi$, which yields $x_{III} - x_{II} \approx 25nm$ independent of the value of V_{NN}/kT . (d) Relaxation distance in the z-direction as a function of V_{NN}/kT for various V_{NN}/V_{HN} with $\theta_B = 0.42\pi$, based on the same set of simulations as in (c). The z-component depends more strongly on V_{NN}/kT than on V_{NN}/V_{HN} .

in $x_{III} - x_{II}$ with V_{NN}/V_{HN} for $\theta_B \approx 0.4\pi$ is about $1nm$, less than the margin of error in the experimental estimation of the working stroke distance.

Fig. 5.8(c) shows that $x_{III} - x_{II}$ approaches $25nm$ with increasing V_{NN}/V_{HN} for $\theta_B = 0.42\pi$, and is relatively independent of the absolute values of V_{NN}/kT and V_{HN}/kT . The corresponding values of $z_{III} - z_{II}$ depend more strongly on V_{NN} (fig. 5.8(d)), because increasing the flexibility of the neck domains decreases z_{II} , as discussed above. For $V_{NN} > 100kT$, $z_{III} - z_{II} = 6nm \pm 1nm$, in agreement with experimental measurements.

In summary, the x-component of the relaxation distance of the motor depends most strongly on the attachment angle θ_B . For $\theta_B \approx 0.4\pi$, the model reproduces the $25nm$ average forward movement accompanied by an average movement away from the filament measured by Cappello et al. [98]. Unless otherwise noted, we will use $\theta_B = 0.4\pi$ for the remainder of this chapter. The amplitude of the average z-direction motion away from the filament depends on V_{NN} and V_{HN} , which could in principle be used to constrain these parameters. However, before we can say with confidence how well the predicted difference between the equilibrium conformations in mechanical states II and III correspond to the movement away from the filament measured by Cappello et al. [98], an ongoing investigation will include using the same step-finding algorithm that was used for the experiment in order to directly compare theoretical and experimental step averages for different model parameters (see chapter VI). For the remainder of this chapter, we will continue to treat V_{NN} and

V_{HN} as free parameters, which we will vary to demonstrate their impact on specific model predictions.

Coordination of Stepping: Strain-dependent Internal Feedback

As discussed in chapter I, myosin-V walks along actin in a coordinated manner, with the detachment cycles of the two heads out of phase, so that about 20–60 hand-over-hand steps are taken before the motor detaches from actin [2, 91–93, 95, 96, 107–109]. The gating mechanism that prevents premature detachment of the leading head is an area of ongoing investigation [111].

Because ADP release is the slowest step in the myosin-V mechanochemical cycle [97], and ADP release from a head is sensitive to force applied to the adjacent neck domain [85, 92, 102, 110, 113], strain dependence of ADP release provides a plausible communication mechanism between the two heads. As mentioned in chapter I, this communication could be mediated in one (or both) of the following ways: (1) A forward-directed strain on the trailing head increases the rate of ADP release from this head, thus increasing the likelihood for the trailing head to detach first. (2) A rearward strain on the leading head inhibits ADP release from this head, making it less likely to detach than the trailing head.

Experimental support for the second mechanism is provided by Purcell et al. [110], in which a myosin-V monomer (i.e., a single head and neck domain) attached to actin is subjected to external forces of various directions and magnitudes applied to the end

of the neck domain. They use a feedback-controlled piezo-electric stage to move a dual bead optical trap in order to exert a force on a myosin-V monomer that is bound to a trapped actin dumbbell. They measure an ADP release rate of about $k_{56}^0 \approx 15s^{-1}$ in the absence of load. The measured ADP release rate is relatively unaffected by external forces applied in the direction of motility ($+x$ -direction). They measure a reduced ADP release rate in the presence of an external force in the $-x$ -direction. In particular, for a $2pN$ rearward force, the measured ADP release rate is decreased by about a factor of ten ($k_{56} \approx 1.5s^{-1}$). Interestingly, for truncated neck domains, they observe a decrease in this effect: For a truncated neck domain of total length $20nm$, slightly less reduction in the ADP release rate is observed than in the case of a full $30nm$ neck domain. For a short $10nm$ neck domain, the ADP release rate in the presence of a $2pN$ rearward force is almost as high as the original ADP release rate in the absence of an external force on the motor.

The measurements by Purcell et al. [110] could be explained by a gating mechanism in which the ADP release rate is affected by the torque exerted on the neck domains. The authors suggest that the neck domain acts as a lever that amplifies the effect of a force on the end of a neck domain. We test this idea by proposing that the rate of ADP release from a head is related to the amount of conformational energy stored in the head-neck juncture due to the rotation of the neck domain with respect to the head ($\propto \cos\theta_i(t) - \cos\theta_B$, from equation 5.1). We express the ADP release rate as

$$k_{56}(t) = \begin{cases} k_{56}^0 \exp((\cos\theta_i(t) - \cos\theta_B) \xi/kT) & : \cos\theta_i(t) - \cos\theta_B < 0 \\ k_{56}^0 & : \cos\theta_i(t) - \cos\theta_{pref}(i) \geq 0 \end{cases} \quad (5.2)$$

Here, the parameter ξ (in units of kT) characterizes the sensitivity of k_{56} to angular displacement from the preferred head-neck juncture angle, θ_B . In this model, the ADP release rate decreases with rearward rotation of the neck domain, but is unaffected for $\theta_i < \theta_B$. The functional form of equation 5.2 is a choice intended to represent the hypothetical mechanism that the ADP release rate is reduced by neck domain rotation in response to rearward torque. Other functional forms, such as exponential dependence on $\theta_i(t)$ rather than $\cos\theta_i(t)$, could also be used. Because experimental data does not provide a detailed account of the ADP release rate as a function of attachment angle, we choose a function that is consistent with the potential energy framework of the polymer model used here (eq. 5.1) and calibrate the free parameter, ξ , to existing experimental measurements (as described later in this section). In the remainder of this section, BD simulations are used to test the effectiveness of a torque-dependent kinetic gating mechanism (eq. 5.2) in reproducing the experimentally observed level of coordination in myosin-V steps.

Simulations of the conformation of the motor in state II illustrate how eq. 5.2 results in a smaller ADP release rate for the leading head than for the trailing head (fig. 5.9(a)). Fig. 5.9(b) shows $\langle \cos\theta \rangle$ for each head-neck juncture in state II as a function of V_{NN}/V_{HN} for $\theta_B = 0.4\pi$. The motor has $\langle \cos\theta_{lead} \rangle < \cos\theta_B$ and

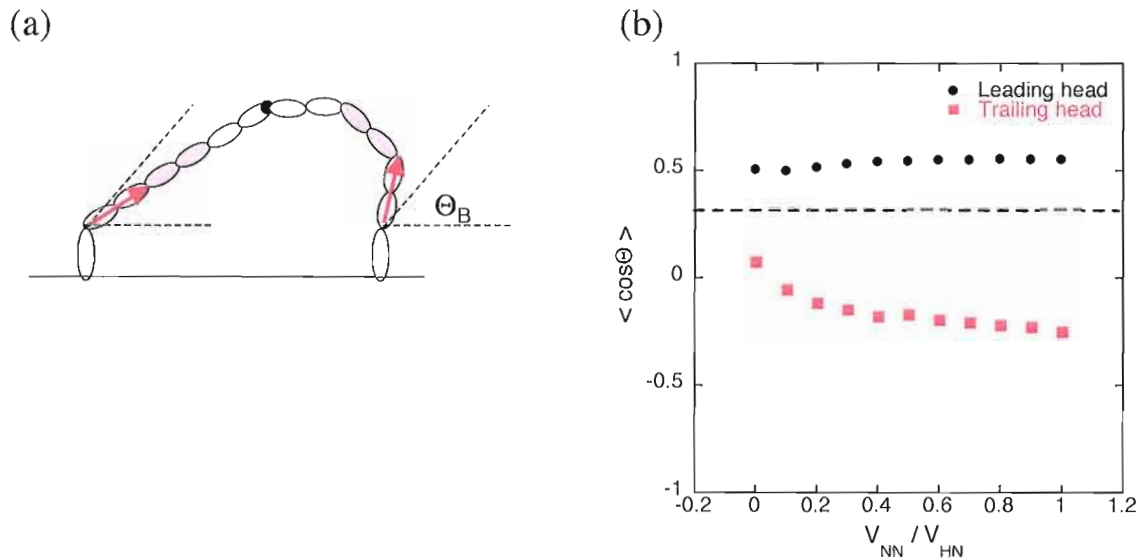


Figure 5.9. Angular displacement of neck domains in state II. (a) Schematic of the angular displacement of neck domains from the preferred attachment angle θ_B in mechanical state II. The average angles (which minimize the intramolecular strain according to equation 5.1) depend on θ_B and V_{NN}/V_{HN} . (b) Brownian dynamics simulations of $\langle \cos \theta_i \rangle$ in mechanical state II for each head-neck juncture as a function of V_{NN}/V_{HN} for $\theta_B = 0.4\pi$. Over the range of V_{NN}/V_{HN} , $\langle \cos \theta_{lead} \rangle < \cos \theta_B$ and $\langle \cos \theta_{trail} \rangle > \cos \theta_B$, which yields $\langle k_{56} \rangle < k_{56}^0$ for the leading head and $k_{56} \approx k_{56}^0$ for the trailing head according to the hypothetical gating mechanism for ADP release (equation 5.2).

$\langle \cos \theta_{trail} \rangle > \cos \theta_B$, such that the leading head will have $\langle k_{56} \rangle < k_{56}^0$ and the trailing head will have $\langle k_{56} \rangle = k_{56}^0$. While the specific values of $\langle \cos \theta \rangle$ for the leading and trailing heads depends on the preferred angle, θ_B , the qualitative observation that $\langle \cos \theta_{trail} \rangle > \langle \cos \theta_{lead} \rangle$ holds for all $0 < \theta_B < 0.5\pi$, because the leading neck domain pulls the trailing neck domain forward and vice versa (fig. 5.9(a)). This establishes a kinetic asymmetry that makes it likely for the trailing head to proceed through the chemical cycle and detach from actin before the leading head.

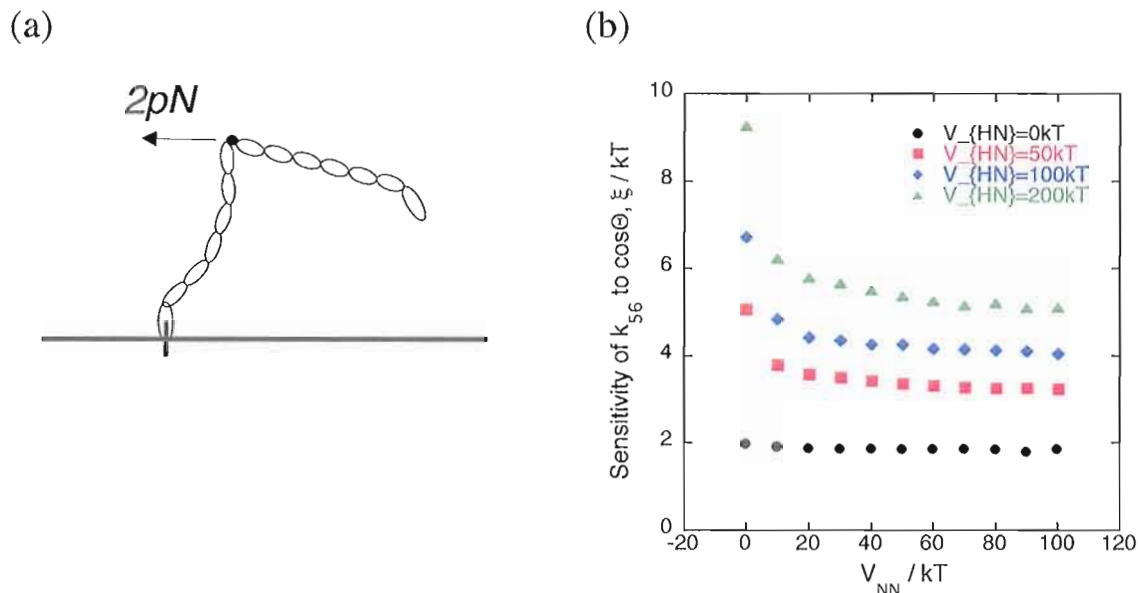


Figure 5.10. Simulations: Angular sensitivity calibration. (a) Schematic of computational “pulling experiment”, in which a $2pN$ rearward force is applied to the juncture between neck domains for the motor in mechanical state III. The resulting value of $\langle \cos\theta_i \rangle$ is recorded. This is used to calculate the angular sensitivity parameter ξ in equation 5.2 by inserting the simulated value of $\langle \cos\theta_i \rangle$ and setting $k_{56}/k_{56}^0 = 0.1$ based on results from an experimental pulling experiment [110]. (b) Calibrated values of ξ as a function of V_{NN} for several values of V_{HN} with $\theta_B = 0.4\pi$.

In order to predict the ADP release rate from each head based on eq. 5.2, a value for the sensitivity parameter, ξ , must be chosen such that the simulated values of k_{56} are consistent with the measured values in Purcell et al. [110]. The experimentally measured k_{56} decreases by a factor of ten in the presence of a $2pN$ rearward force. The angular rotation of the head-neck juncture was not measured in this experiment, but ξ can be calibrated by simulating the motor in state III with a $2pN$ load force applied at the end of the attached neck domain (fig. 5.10(a)). Simulated values of $\langle \cos\theta_i \rangle$ for the attached head-neck juncture can be inserted into eq. 5.2, setting $k_{56}/k_{56}^0 = 0.1$ (equal

to the experimentally observed value), to solve for ξ . Fig. 5.10(b) shows the resulting ξ as a function of V_{NN} and V_{HN} with $\theta = 0.4\pi$. This can serve as a calibration for the model, so that the dependence of k_{56} on the conformation of the motor is expected to be consistent with experimental measurements.

To assess the effectiveness of this angle-dependent gating mechanism (eq. 5.2), we define “kinetic asymmetry”, λ , as the relative probability for ADP dissociation from the trailing head:

$$\lambda(t) = \frac{k_{56}^{trail}(\theta_{trail}(t))}{k_{56}^{trail}(\theta_{trail}(t)) + k_{56}^{lead}(\theta_{lead}(t))} \quad (5.3)$$

The kinetic asymmetry, $\lambda(t)$, depends on the instantaneous conformation of the motor, and is highest when the leading neck domain is rotated in the rearward direction with respect to the preferred angle, θ_B . If $k_{56}^{trail} = k_{56}^{lead}$, the kinetic asymmetry is $\lambda = 0.5$, and either head is equally likely to unbind from actin. In the limit that $k_{56}^{trail} \gg k_{56}^{lead}$, then $\lambda \rightarrow 1$, and the likelihood of leading head detachment goes to zero.

To calculate the time-averaged kinetic asymmetry, $\langle \lambda \rangle$, for different choices of V_{NN} and V_{HN} , the motor is simulated in state II with $\theta_B = 0.4\pi$, producing $\theta(t)$ for each head-neck juncture. The kinetic asymmetry, $\lambda(t)$, is calculated at discrete time intervals throughout the simulation with eqs. 5.2 and 5.3, using the calibrated values of $\xi(V_{NN}, V_{HN})$ in fig. 5.10(b). The average kinetic asymmetry, $\langle \lambda \rangle$, increases with increasing V_{NN} , because the rearward rotation of the leading neck domain increases

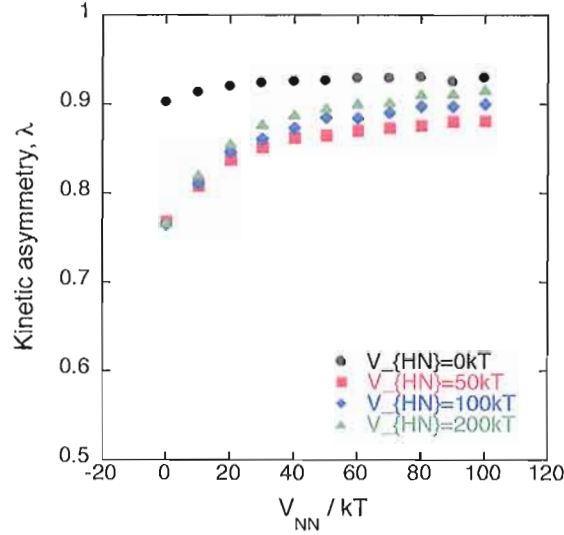


Figure 5.11. Simulations: Kinetic asymmetry. The kinetic asymmetry, λ , is defined as the relative probability for ADP release from the trailing head when both heads are in kinetic state 5 (attached to actin with ADP bound). ADP release is the rate-limiting step for detachment from actin, and thus a high kinetic asymmetry $\lambda \approx 1$ indicates that the leading head is very unlikely to detach from actin, while $\lambda \approx 0.5$ indicates that the leading and trailing head have equal probabilities to detach from actin. Simulated values of $\langle \lambda \rangle$ increase with neck domain stiffness, because this increases the rearward rotational displacement of the leading head, thus decreasing ADP release rate for this head according to the proposed gating mechanism in equation 5.2.

as the neck domains become stiffer (fig. 5.11). Also, a slight increase in $\langle \lambda \rangle$ with V_{HN} is observed, presumably because of the higher calibrated values of the sensitivity parameter, ξ , for higher V_{HN} (fig. 5.10(b)). For $\theta_B = 0.4\pi$, $\langle \lambda \rangle > 0.75$ for all V_{NN} and V_{HN} , meaning that leading head detachment is predicted to occur less than 25% of the time. For higher values of the neck domain stiffness, $\langle \lambda \rangle \rightarrow 0.9$, such that leading head detachments are expected for fewer than 10% of the detachment events.

Samples of simulated stepping data are shown for two cases (with parameters $\theta_B = 0.4\pi$ and $V_{NN} = V_{HN} = 100kT$): without angle-dependent gating, such

that the ADP release for either head is $k_{56} = k_{56}^0 = 15s^{-1}$ (fig. 5.12(a)), and with angle-dependent gating based on equation 5.2 (fig. 5.12(b)). Without gating, the kinetic asymmetry is by definition $\lambda = 1/2$, and either head has equal probability to detach first. In fig. 5.12(a), there are frequent “spikes” in between steps in which the center-of-mass position temporarily decreases. These correspond to times when the leading head detaches and then reattaches in its original site. Even without kinetic asymmetry, the motor still walks hand-over-hand in a preferred direction for the mechanical parameters in fig. 5.12, because the diffusional search of a detached head is biased by the forward-leaning preferred angle, θ_B , of the attached head-neck juncture. The stepping data from simulations with angle-dependent gating also (less frequently) show some spikes corresponding to leading head detachments (fig. 5.12(b)). Also, the data occasionally display spikes in between steps that temporarily increase the center-of-mass position, which correspond to failed step attempts in which a trailing head detaches, but reattaches in its original site. The frequency of these events depends on θ_B , V_{NN} , and V_{HN} , which determine the effectiveness of the mechanical bias in a detached head’s diffusional search. Similar events are detected in the experimental data of Cappello et al. [98], and a systematic comparison between these features in their data and our simulations could help interpret the experimental observations.

For both cases (with and without angle-dependent gating), the average velocity is on the same order, and is limited by the average amount of time it takes for the trailing head to detach (k_{56}^{-1}). However, simulations with angle-dependent gating have

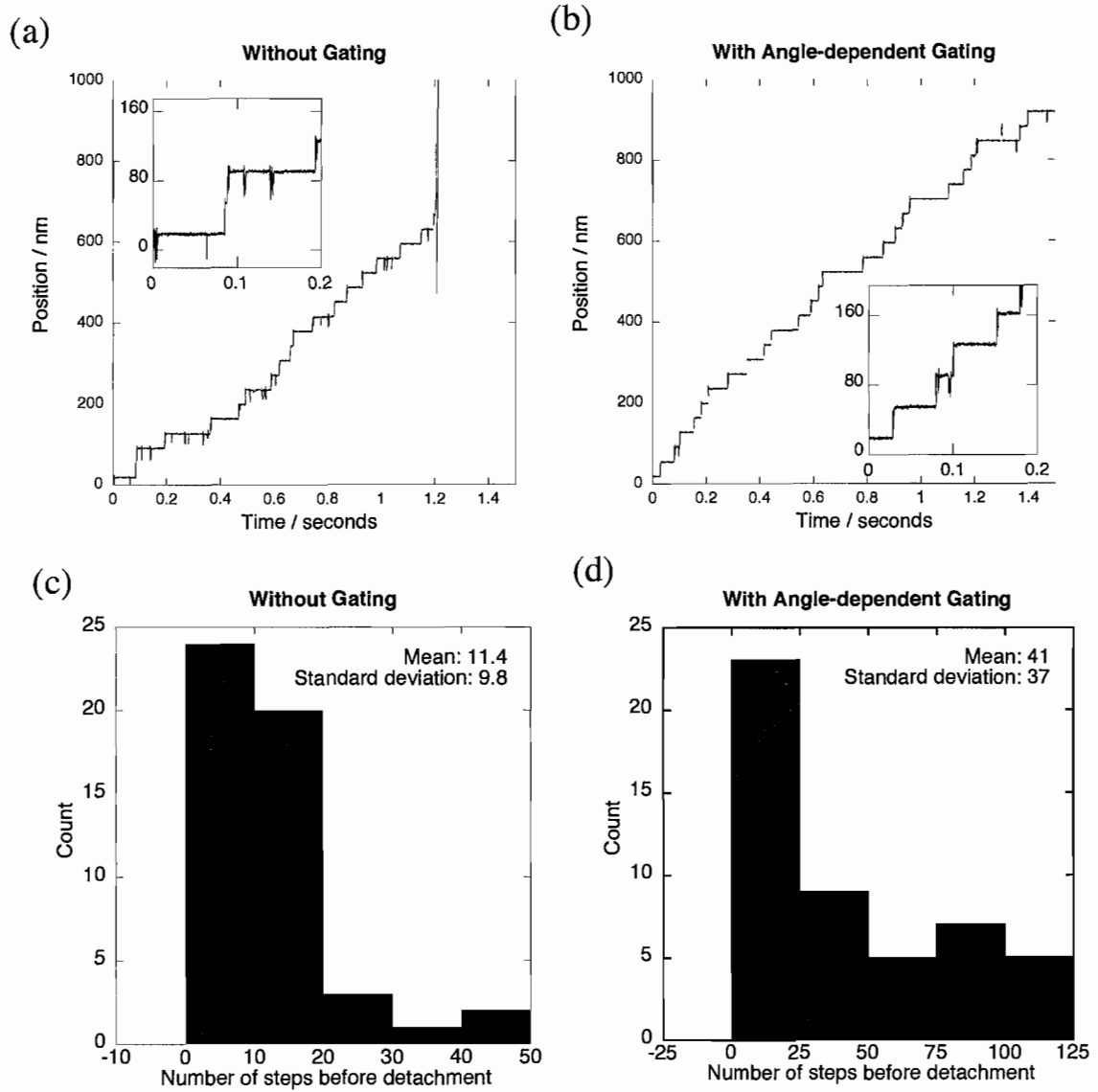


Figure 5.12. Brownian dynamics simulations of walking, with mechanical parameters $\theta_B = 0.4\pi$ and $V_{NN} = V_{HN} = 100kT$. (a) Sample of simulated stepping data without any coordination between heads. In this case $\xi = 0$ in equation 5.2, such that $k_{56} = k_{56}^0$ and $\lambda = 1/2$ regardless of the conformation. (b) Sample of simulated stepping data for same mechanical parameters as (a) with coordination between heads based on equation 5.2 with $\xi = 4.046kT$ based on the calibrated value in fig. 5.11(b). (c) Histogram of run length (number of steps before detachment) for about 50 individual walking simulations with uncoordinated steps ($\xi = 0$). (d) Histogram of run length for 50 individual walking simulations with coordinated stepping ($\xi = 4.046kT$). Average run length is significantly higher with angle-dependent coordination of the ADP release.

significantly longer run lengths on average. The average run length is approximately 11 steps without gating (fig. 5.12(c)), and approximately 41 steps with gating (fig. 5.12(d)). In both cases, the run length distribution for about 50 individual processive runs (i.e., walking data until the motor detaches) is exponentially distributed, with a larger spread in the distribution for processive runs with gating. The run length histogram for the angle-dependent gating model (fig. 5.12(d)) is consistent with the experimentally observed run lengths of 20–60 steps. The angle-dependent gating mechanism introduced here increases the run length by decreasing the likelihood for leading head detachment. When the leading head detaches, this introduces an opportunity for the trailing head to also detach, thus ending the processive run. This gating model, in which we assume that ADP release is biased based on the rotation of the neck domain away from a preferred angle, is successful in explaining the experimentally observed increase in run length compared with what is expected for uncoordinated walking.

Tethered Diffusion of the Detached Head in the One-head-bound State

As mentioned in chapter I, the increasingly high spatial and temporal resolution of single molecule experiments has allowed several recent experiments to access details of the short-lived intermediate in which one head is attached to actin and the other is detached. Several experiments support a model in which the detached head undergoes a diffusional search for an available binding site [100, 105]. For example, Dunn et

al. [100] elucidate some of the dynamics of this tethered diffusion through direct observation of a gold nanoparticle attached to one of the neck domains. They find that the detached head rotates freely about the neck domain junction, and that the reattachment rate is sensitive to the rate of ATP hydrolysis (which can be altered through modification of the proteins in the IQ motif closed to the head domain [97]). Simulations of the tethered diffusion of a detached head (mechanical state III) can complement these experimental measurements by addressing questions such as: (1) Which is the rate-limiting part of reattachment; ATP hydrolysis (k_{23}), diffusion, or both? (2) How does this change in the presence of a load force? These questions have important physiological implications, in that the dynamics of the reattachment process will determine the likelihood for the motor to completely detach before the step is completed.

Simulations of the “first passage time” (i.e., the average time it takes for a detached head to find a new binding site (see Appendix A)) demonstrate that the diffusional search happens much faster than the rate of ATP hydrolysis, suggesting that the reattachment process is not diffusion-limited. Fig. 5.13(a-c) shows the reciprocal of the first passage time (which we will call the “tethered diffusion rate”) as a function of external load for several choices of the attachment angle in the range $0 < \theta_B < 0.5\pi$ and for various choices of $V_{NN} = V_{HN}$. (Non-uniform stiffness, $V_{NN} \neq V_{HN}$, has not been ruled out, but we initially consider the simplest case in order to begin testing

the load dependence of the tethered diffusion for different levels of overall stiffness of the molecule.)

In general for the values of θ_B tested, the tethered diffusion rate is about an order of magnitude higher than the rate of ATP hydrolysis ($k_{23} = 700s^{-1}$) under zero load conditions (fig. 5.13(d)). As a result, the detached head is likely to ‘tap’ an available binding site a number of times before actually reattaching. This means that in the absence of load, the reattachment rate is not limited by the tethered diffusion of the detached head and is therefore not highly sensitive to the mechanical parameters of the model in the range considered for these calculations. A longer first passage time is expected for very flexible neck domains ($V_{NN} < 10kT$), because increased flexibility increases the conformational entropy of the polymer. However, this level of flexibility is well outside the experimentally supported range.

Under rearward load, the attached neck domain is pulled backward, counteracting the usual bias of the diffusional search toward a “forward” binding site. For this reason, the tethered diffusion rate decreases with load, and eventually goes to zero (which means that the head is unlikely to reattach as the leading head, but has an increased chance of reattaching as the trailing head). The decrease in the tethered diffusion rate is more gradual for higher values of $V_{NN} = V_{HN}$, since it requires more force to bend a stiffer neck domain. The decrease in the tethered diffusion rate is also more gradual for smaller attachment angles, because a small value of θ_B means that the motor can be pulled further away from the preferred attachment angle while still

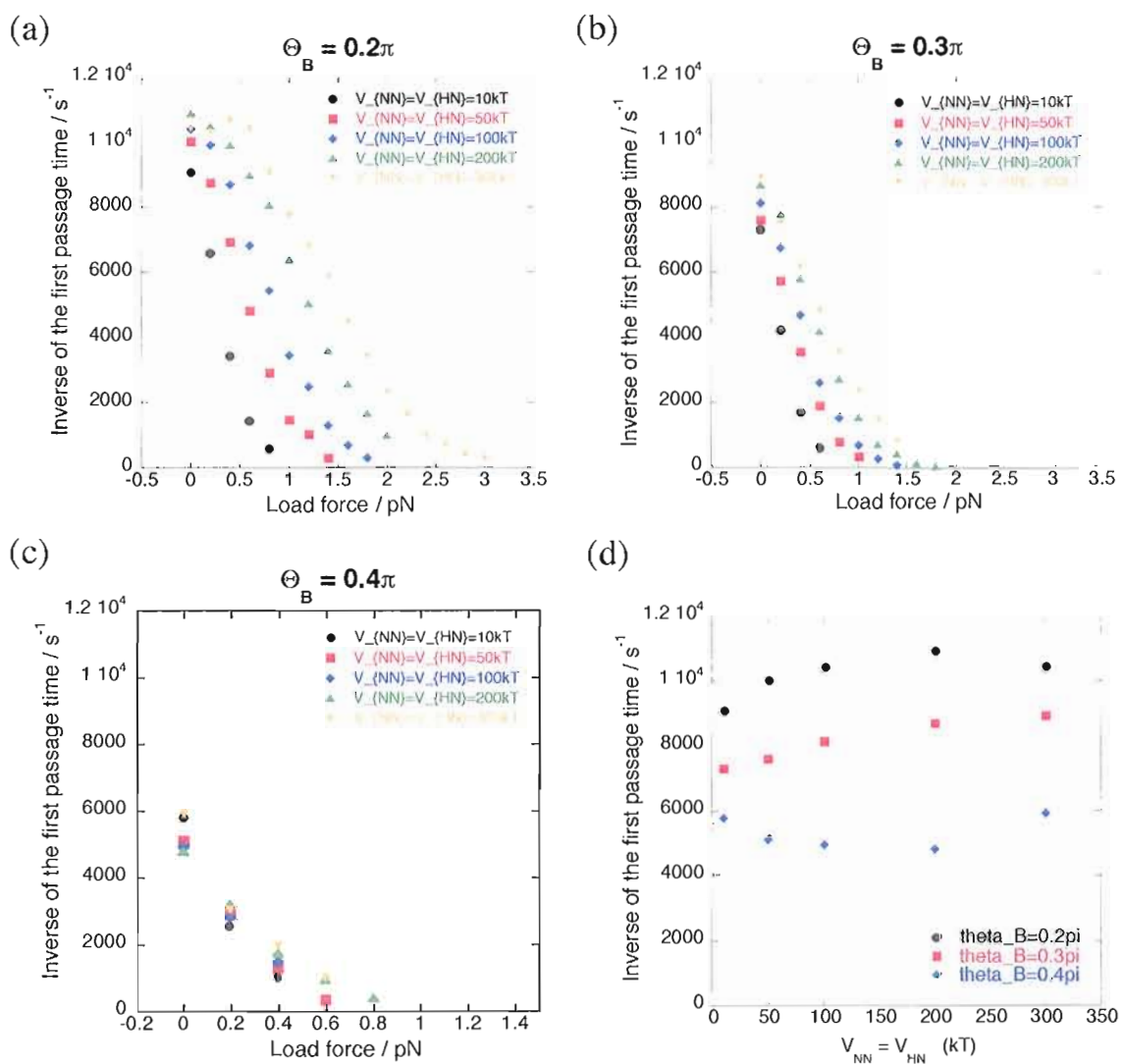


Figure 5.13. Simulations: First passage time for diffusional search. Inverse of the first passage time for a detached head's diffusional search for a binding site, as a function of load applied at the juncture between neck domains, for several values of $V_{NN} = V_{HN}$, is shown for different attachment angles: (a) $\theta_B = 0.2\pi$; (b) $\theta_B = 0.3\pi$; and (c) $\theta_B = 0.4\pi$. (d) The inverse of the first passage time under zero load (from (a), (b), and (c)) shown as a function of $V_{NN} = V_{HN}$ for each value of θ_B . The dashed horizontal line indicates the rate of ATP hydrolysis for comparison. These data suggest that reattachment is limited by ATP hydrolysis rather than the rate of tethered diffusion.

having a forward bias on average. The stall force, which characterizes the maximum amount of force the motor is able to exert, is sensitive to the motor stiffness and the attachment angle. In fig. 5.14(a), the stall force is shown as a function of $V_{NN} = V_{HN}$, for $\theta_B = 0.2\pi$, $\theta_B = 0.3\pi$, and $\theta_B = 0.4\pi$, indicating that the stall force increases approximately linearly with increasing stiffness. These estimated stall forces are based on extrapolating the load force at which the tethered diffusion rate goes to zero in fig. 5.12(a-c). The large uncertainty in the stall force arises from the smaller number of “reattachment” events in simulations in mechanical state III under load conditions close to stall.

In order to estimate a lower bound for the stiffness parameters $V_{NN} = V_{HN}$, we plot the minimum $V_{NN} = V_{HN}$ for which the model produces $f_{stall} > 1.5pN$ as a function of θ_B (fig. 5.14(b)). Because $1.5pN$ is on the low end of experimentally estimated stall forces, this plot can be interpreted as the minimum stiffness necessary to reproduce experimentally measured stall forces for a given choice of θ_B . Earlier in this chapter, the attachment angle $\theta_B \approx 0.4\pi$ was predicted to reproduce the approximately $25nm$ first phase of the myosin-V step average. Fig. 5.14(b) indicates that the motor must have very high stiffness ($V_{NN} = V_{HN} > 300kT$) to also reproduce experimental observations of the motor’s ability to do work against an external load.

However, these predictions of the stall force are all based on simulations with the simplification that the stiffness of the head-neck juncture is the same as the stiffness of any of the neck domain joints ($V_{NN} = V_{HN}$). In reality, non-uniform stiffness

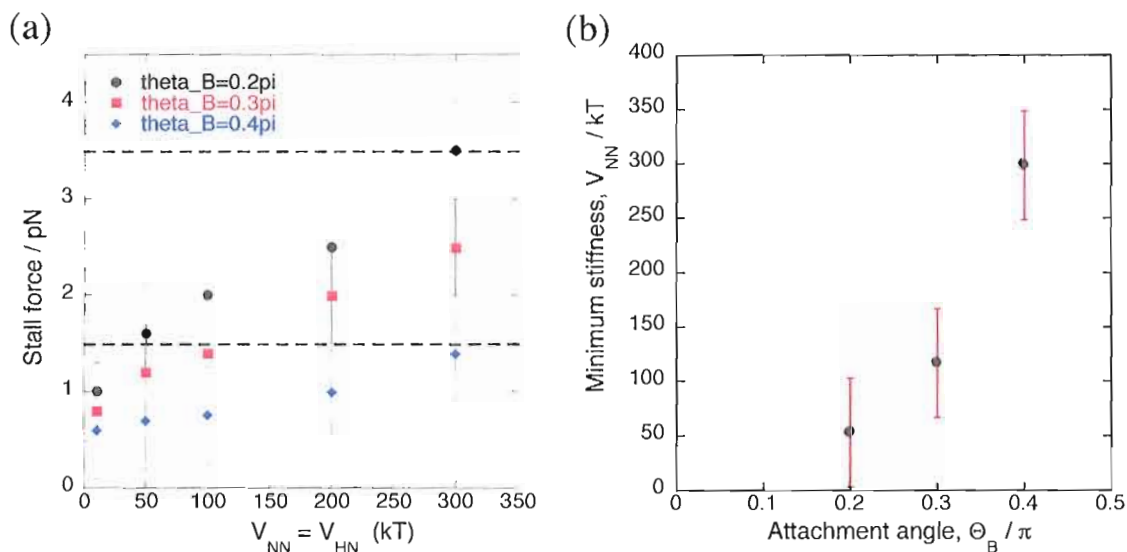


Figure 5.14. Simulations: Dependence of stall force on physical properties of motor. (a) Stall force as a function of $V_{NN} = V_{HN}$ for several values of θ_B . Here, the stall force is defined as the maximum load force under which the motor is still able to take a step forward. We estimate the stall force by extrapolating the force at which the inverse of the first passage time for tethered diffusion to a “forward” binding site goes to zero in fig. 5.13(a-c). The large error in this estimate reflects the small number of times that a detached head reaches a forward binding site in simulations with applied load close to the stall force. Dashed horizontal lines indicate the upper and lower bounds for experimental measurements of the stall force. (b) To illustrate the minimum stiffness needed to reproduce experimental stall force, the minimum $V_{NN} = V_{HN}$ that may produce $f_{stall} \geq 1.5pN$ according to (a) is shown for several values of θ_B .

($V_{NN} \neq V_{HN}$) would change the distribution of internal strain between the neck domain and the head-neck juncture, and could affect the way the motor bends in response to an external load. Now that the approximate ranges of the stall force have been identified for various $V_{NN} = V_{HN}$ and θ_B , more statistics can be gathered from longer simulations in this range, and the performance can be tested for different values of V_{NN}/V_{HN} .

One would expect the run length of myosin-V to decrease in the presence of a load force, because longer first passage times would increase the likelihood for the other head to detach before the first detached head reattaches. Simulations of myosin-V steps in the presence of significant external load would require a model for the kinetic pathway of the dimer in the presence of load forces close to and above the stall force, and is beyond the scope of the work presented here. Please see chapter VI (Discussion and Outlook) for a discussion of how a generalized version of this model could be developed to study the experimentally observed occurrence of backward stepping in the presence of super-stall load forces [92].

Concluding Remarks

In this chapter, a wide range of information from experiments is incorporated into a minimal model for the mechanical features of myosin-V, in the context of the predominant chemical cycle of the motor. By treating the neck domains as semi-

flexible filaments with state-dependent preferred attachment angles, it is possible to reproduce several important performance features of myosin-V.

First, we compare the predicted motion of the neck domain juncture after detachment of the trailing head (referred to as the relaxation distance) with characteristics of the experimentally measured step average for an attached cargo. This comparison allows us to constrain the model parameter θ_B , which represents the preferred attachment angle of a head-neck juncture with respect to the actin filament after phosphate release. The mechanical model predicts a relaxation distance less than 36nm parallel to the filament (x-direction) accompanied by a perpendicular movement away from the filament (z-direction) if $\theta_B > 0.3\pi$, which gives qualitative agreement with experimental measurements. More specifically, if $\theta_B \approx 0.4\pi$, the model predicts a 25nm x-component of the relaxation distance, accompanied by a 5-10 nm movement away from the actin filament, in close quantitative agreement with experimental measurements [98].

Next, we propose an experimentally motivated model for the physical mechanism of coordination between the two heads. In the proposed coordination mechanism, the neck domain serves as a lever that amplifies intra-molecular strain in order to inhibit ADP release from the leading head, thus making it less likely to detach from actin. We suggest that the ADP release rate from a head depends on the angle of attachment between the head and the adjacent neck domain, and is therefore sensitive to torque applied to the neck domain. We demonstrate that this mechanism successfully reproduces the processivity of myosin-V, dramatically increasing the

number of steps before detachment compared with a model in which the kinetic cycles of the two heads are uncoordinated. A prediction for the ratio of leading head detachment to trailing head detachment is made, which depends on the stiffness of the neck domains. To our knowledge, this is the first theoretical study to propose and test a specific mechanical explanation for how intra-molecular strain mediates asymmetric detachment probabilities between the leading and the trailing head. In chapter VI (Outlook), we suggest some possible experiments that could test the model.

Simulated data of the hand-over-hand transport, along with corresponding animations, visualize the strong influence of noise on the stepping process. This model provides a tool that can be used for ongoing analysis of the physical mechanism underlying the myosin-V step.

CHAPTER VI

DISCUSSION AND OUTLOOK

In this dissertation, theoretical models for Brownian and biomolecular motors were studied in order to learn about the operation of machines on the nano-scale. Motors that operate in a thermal environment are fundamentally different than macroscopic motors in that they operate in the presence of substantial thermal noise, and their motion is overdamped.

The work in this dissertation takes a two-pronged approach to the study of nano-scale motors: First, a theoretically established type of Brownian motor called the flashing ratchet was extended to consider how coupling between the motion of the particles affects the transport. Special emphasis was placed on hypothetical experimental considerations such as the size and shape of the particles and time delays in experimental control of a noisy system. The theoretical work here has contributed to the planning and analysis of the experimental realization of artificial Brownian motors.

Secondly, a mechanical model for a specific biological molecular motor, myosin-V, was developed in order to study how the motor takes coordinated steps in a thermal environment. An experimentally-motivated mechanism for mechanical coordination between the stepping cycles of the two myosin-V heads is proposed, suggesting that

the detachment rate of a myosin-V head is related to the angle of attachment of the adjacent neck domain. Below, the key findings of these studies are summarized and ideas for continued work on these topics are discussed.

Coupled Motion in Flashing Ratchets

A flashing ratchet is a type of Brownian motor in which diffusive particles are transported by turning a spatially periodic and asymmetric potential on and off. For non-interacting point particles in a flashing ratchet, net transport is achieved through alternation between free diffusion and asymmetric localization. In chapter III, the basic flashing ratchet system is modified to consider the transport of objects with internal structure. For chains of particles with fixed interparticle separation distance, it is demonstrated that the direction of transport depends on the size of the chain and the temperature of the system. Reversal as a function of size no longer occurs for a rigid particle chain that undergoes three-dimensional rotational diffusion, because the chain will localize with the center-of-mass at the minimum of the potential. In this case, the symmetry of the system is similar to that of non-interacting point particles in that the direction of transport changes as a function of the asymmetry of the ratchet potential but is independent of other system parameters.

Motivated by an experimental flashing ratchet system that uses a scanning line optical trap to create a quasi-one-dimensional flashing ratchet to transport a bead [51], we model the effect of the finite bead size on the symmetry of the effective

potential. We show that the effective value of the asymmetry parameter a (which characterizes the fraction of a piecewise linear potential with negative slope) increases as a function of bead size when the input asymmetry is in the range $0 < a < 1/2$. This is expected to decrease the average velocity of transport because a less asymmetric potential is less effective at achieving flashing ratchet transport. We show that the experimentally characterized effective potential is in close agreement with theoretical predictions for the bead size and ratchet shape currently used in the experiment, which could account for the slightly lower velocity of experimental ratchet transport compared with theoretical predictions for certain control protocols.

The theoretically predicted effective potential for a bead with diameter greater than half the spatial period of the potential has a reversed symmetry ($a_{eff} > 1/2$) from the symmetry of the sawtooth potential ($a < 1/2$), suggesting that beads of different size could be transported in different directions by the same flashing ratchet potential. This prediction has not yet been verified experimentally, but the optical ratchet system discussed above is well-equipped to provide the first experimental demonstration of size-dependent sorting in a flashing ratchet. More distant applications could include mechanically linking the dielectric beads by attaching one bead to each end of a strand of DNA (using methods that have been established for other mechanical experiments on DNA [134]), and using the optical ratchet setup to study flashing ratchet transport of mechanically coupled objects. Such a study would benefit from continued synthesis of theoretical modeling, simulations and experiments.

In chapter IV, the effect of time delay on closed-loop control of a flashing ratchet system is investigated. Closed-loop control (also referred to as feedback control) is defined as control of the system that is enacted in response to information about the internal state of the system. In the case of a flashing ratchet, closed-loop control policies have been introduced in which the potential is turned on and off in response to information about the net force [69, 74] or the positional distribution [18] of the particles, in order to increase the average velocity of the particles. Here, the role of time delay in closed-loop control based on the net force is studied, considering two types of delay: delay in measuring the system and delay in implementing the feedback policy.

It is demonstrated in chapter IV (and in [17, 18]) that these types of time delay impact the system differently for small ensembles of particles than for large ensembles. For small particle numbers, time delay of any kind is detrimental to the effectiveness of the feedback control policy, because it reduces the accuracy of measured information about the state of the system. The study presented in chapter IV of the range of time delays over which closed-loop control of a small ensemble produces a higher velocity than open-loop control is directly relevant to the optical flashing ratchet system discussed above, which has been used to experimentally realize flux enhancement in ratchet transport of 1 – 5 beads through use of closed-loop control.

For large ensembles, a finite delay in implementation can increase the velocity by allowing the state of the system to evolve to a configuration that is more advantageous

for switching the potential. This improvement in the performance of the control mechanism through time delay (originally considered an experimental disadvantage) is possible because the time-evolution of a large ensemble is predictable. An experimental test of this prediction for large particle numbers has not yet been achieved. Doing so would require the development of a ratchet system where the particles are not confined to one-dimensional diffusion, so that a large number of particles can be included without the motion being inhibited by frequent collisions. (However, eventually the collisions themselves could be an interesting aspect of the system to study in their own right.) The feedback control of a large ensemble has relevance beyond the abstract flashing ratchet system. For example, the interaction between news media and public opinion could be considered a form of closed-loop control of a dynamic system, in which timing is crucial.

On the theoretical front, an interesting application for closed-loop feedback protocols would be to consider feedback control of flashing ratchet transport of an object with internal degrees of freedom. For example, in Downton et al. [41], simulations of a semi-flexible polymer in a flashing ratchet demonstrate a mode of transport that relies on conformational changes of the polymer. A conformation-dependent feedback control policy could be developed for this system. It is likely that the performance of such a feedback policy would depend sensitively on the characteristic relaxation times of the polymer, and time delay would have an important and non-trivial impact on the results.

Mechanical Model for Myosin-V Walking Mechanism

In chapter V, a mechanical model is introduced to study the walking mechanism of the biological molecular motor myosin-V. Similar to the flashing ratchet ‘toy model’, myosin-V achieves net transport in a thermal environment and is likely to combine Brownian diffusion and ‘power stroke’ mechanisms to achieve this transport. Myosin-V is a dimeric motor that ‘walks’ along actin in a hand-over-hand manner, whereby the trailing head detaches more frequently than the leading head, and moves forward to reattach as the new leading head. The mechanism of coordination between the two heads that makes the trailing head more likely to detach can be considered a type of conformation-dependent feedback control.

We treat the myosin-V neck domains as semi-flexible filaments that attach to the head domains with average angles that depend on the chemical state of the head. Many of the mechanical parameters of the model were fixed based on experimental measurements. The performance of the motor is compared with experimentally measured performance features to partially constrain several remaining input parameters: the post-phosphate-release preferred attachment angle with respect to the transport direction along actin, θ_B , the neck domain stiffness, V_{NN} , and the stiffness of the head-neck juncture, V_{HN} . By comparing equilibrium conformations in mechanical states of the model with characteristics of experimental step averages, we conclude that $\theta_B \approx 0.4\pi$ reproduces the apparent experimental observation that the center of mass

moves part of a step ($\approx 25nm$) forward and away from the filament ($\approx 6nm$) when the trailing head detaches, and the rest of the step is completed through biased Brownian diffusion. Simulations of the first passage time for the diffusional search of a detached head for a binding site as a function of load applied to the neck domain indicate that the stall force increases with filament stiffness and decreases with increasing θ_B . For $\theta_B \approx 0.4\pi$, experimental stall forces are reproduced for very high values of the stiffness parameters: $V_{NN} = V_{HN} > 300kT$. This is somewhat higher than the broad range of experimental estimates of the neck domain stiffness. The load dependence of tethered diffusion has not yet been studied for $V_{NN} \neq V_{HN}$, and it is possible that non-uniform stiffness will allow the experimental stall force to be realized for a smaller neck domain stiffness.

Ongoing comparison between the model and experimental measurements will continue to constrain and test the model, as well as provide a useful tool for analysis of the experiments. A future goal is to directly compare step averages from the computational data produced by this model to experimental step averages. Theoretical methods for converting a single-molecule time series to an effective potential landscape provide another avenue for comparison between our computational data and experimental measurements [135, 136]. In particular the high resolution of the experimental data of Cappello et al. [98] and Dunn et al. [100] are ideal for such a study, allowing comparison between theoretical and experimental measurements of average quantities such as the phases of the step average, as well as characteristics of fluctuations in the

stepping data. It may be necessary to add certain elements from the experiments to the model to learn how they will affect the theoretical predictions, such as flexibility in the linkage between the motor and the bead being monitored, the drag coefficient of the bead, and other factors that may affect the measurement of the motor's motion.

In addition to studying how the mechanical properties of the motor affect the characteristics of an individual step, as discussed above, the mechanism of coordination between the two heads was addressed in chapter V. A model was introduced in which conformation-dependent feedback between the two heads creates an asymmetry in detachment rates of the trailing and leading head. It is demonstrated that this model can explain the experimentally measured run length, which is significantly longer than what is expected for uncoordinated detachment cycles of the two heads. The relative probability of leading head and trailing head detachment is predicted by this model as a function of the stiffness parameters V_{NN} and V_{HN} .

One of the most important functions of a theoretical model for a biological system is to make predictions that can be tested experimentally. An experimental test of a model provides new information about how the system works either by supporting the assumptions of the model or revealing that some essential aspect is missing from the model in its current state. Below, some hypothetical experiments are suggested that could test or constrain this model for the conformation-dependent coordination of myosin-V transport:

(1) *Direct measurement of how the average attachment angle at the head-neck juncture depends on a force applied to the end of the neck domain.* Perhaps this could be done by FRET labeling a head and some known region of the neck domain, in order to observe how the distance between the acceptor and donor fluorophores depend on a force applied to the neck domain. If such a measurement could be done while simultaneously monitoring the ADP release from the head, a value for the sensitivity parameter, ξ , (equation 5.2, chapter V) could be extracted directly from the experiment rather than having to calibrate this value for different V_{NN} and V_{HN} parameters as explained in chapter V. This also could help constrain the head-neck stiffness parameter, V_{HN} .

(2) *Observation of the number of leading head detachments during a processive run.* This would require single-molecule data with very high spatial resolution. It is possible that the data of Cappello et al. [98] contain this information. In their stepping data, they observe occasional events of increased fluctuation between steps that can not be attributed solely to the thermal motion of the bead. They suggest that these events could correspond to aborted step attempts in which a head detaches and reattaches without resulting in a step. By carefully comparing the features of fluctuations in their data with our computational data, it may be possible to discern more about the type of events that would give rise to the features they observe. An experimental estimate of the frequency of step attempts in which a trailing head detaches and

fails to step forward, and the frequency of leading head detachments, would greatly contribute to the understanding of how myosin-V stepping is coordinated.

In the future, the mechanical model for myosin-V presented in this dissertation could be extended to study other mechanical aspects of myosin-V transport. For example, several studies have observed an increase in the frequency of backward steps under applied load [82, 85, 90–92], and processive backward stepping has been observed for load forces above the stall force [92]. Clemen et al. [92] propose a hypothetical mechanism for mechano-chemical coupling of the transition rates under high load to achieve this processive backward stepping. Our model could be used to quantitatively test their hypothetical mechanism for backward stepping, which would complement ongoing experimental tests of the phenomenon. Understanding how myosin-V walks in the presence of external forces is important for developing a more complete understanding of the mechanical features of the motor, and is relevant to the coordination of intracellular transport in situations where a single cargo is attached to more than one motor [137–143].

Another future extension of the myosin-V model could be to simulate attachment of the heads to actin with a more realistic three-dimensional, helical description of the actin filament. The small step size distribution observed in single-molecule experiments supports the idea that myosin-V walks along one side of actin under normal conditions, due to elastic resistance to azimuthal distortion in the head-neck juncture. Myosin-V with truncated neck domains (fewer IQ motifs) exhibits smaller

step sizes [93, 95, 101], which may indicate that the motor can walk in a helical spiral around the actin filament if it is not able to reach the next available binding site along one side of the filament. Simulations of the myosin-V model here with a more realistic three-dimensional actin filament could help test this interpretation and make specific testable predictions for how the step size distribution will vary as a function of mechanical parameters such as neck length, neck domain and head-neck juncture flexibility, and applied load. Understanding more about the mechanical features that determine the location of reattachment of a detached head is important for understanding how the motor navigates a crowded cellular environment. Also the model could be applied to studying when and how molecular motors switch from one filament to another at intersections in the cytoskeletal network, which is of fundamental importance to the coordination of active transport in cells and has been the subject of several recent studies [144–147].

In summary, the mechanical model for myosin-V transport presented in this dissertation incorporates a wide range of experimental information, makes useful and testable predictions about the behavior of the motor, and provides a framework for continued theoretical investigation of physiologically relevant aspects of the operation of the motor.

APPENDIX

SIMULATIONS OF MECHANICAL MODEL FOR MYOSIN-V

In chapter V, a mechano-chemical model for myosin-V is presented, in which the neck domains are modeled as semi-flexible filaments, defined by the interaction potential

$$U = \frac{1}{2} \sum_{i=2}^8 V_i \left(\cos\phi_i(t) - \cos\phi_i^{pref} \right)^2 \quad (\text{A.1})$$

where ϕ_i is the angle between filament segments that meet at point ‘i’. This is the sum of elastic energy for rotation away from a preferred angle for each point (excluding the end-points). These elastic energy terms can be referred to as three-body interactions, because they involve an interaction of three points. This appendix includes a discussion of how the internal forces for this model are calculated. It also includes a brief explanation of how the first passage time for reattachment of a detached head is simulated.

Neck Domain Joints

The interaction potential U for the polymer model (eq. .1) is the sum of three-body potentials in which the elasticity of joint ‘i’ produces a force on point ‘i’ and on the adjacent two points. The cosine of the angle at any of the joints in the chain

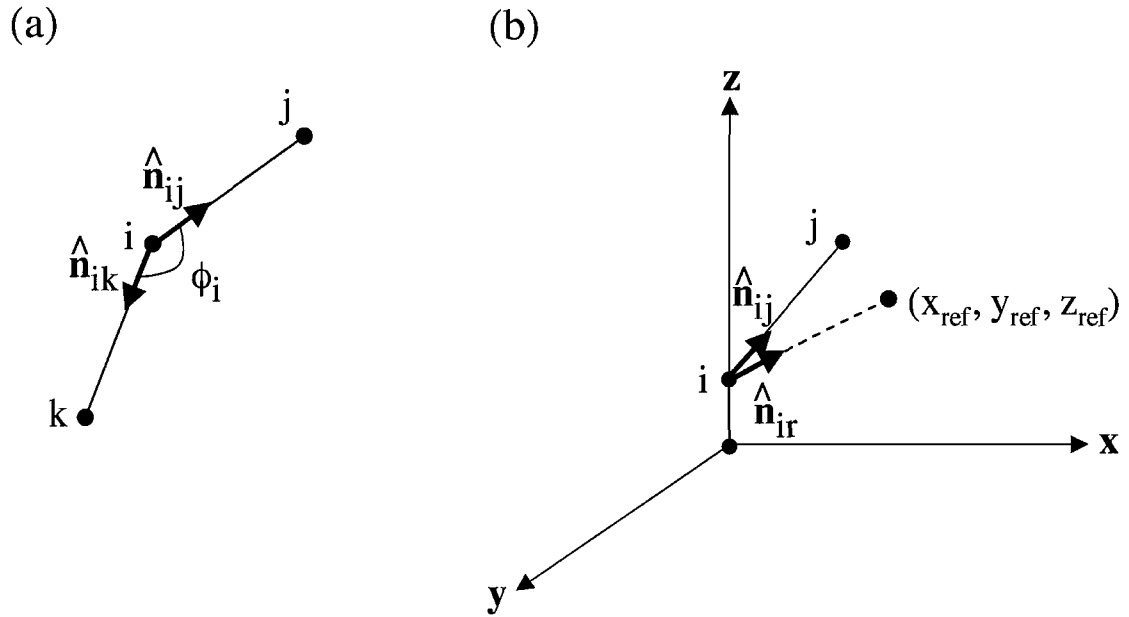


Figure A.1. Schematic: Three-body interactions in semi-flexible polymer model: (a) Schematic to illustrate the calculation of forces due to the elastic three-body interaction at a joint in the neck domain (see text). (b) Schematic to illustrate the calculation of forces due to the elastic interaction at a head-neck juncture for a head that is attached to actin (see text).

depends on the positions of the two surrounding joints: $\cos\phi_i = \hat{\mathbf{n}}_{ij} \cdot \hat{\mathbf{n}}_{ik}$, where $\hat{\mathbf{n}}_{ij}$ is the normal vector pointing from point ‘i’ to point ‘j’ (see fig. A.1(a)). Physically, this means that if any joint in the filament is bent away from the preferred angle, there will be a restoring force on this point and the surrounding two.

The three-body interaction potential for joint ‘i’ in the neck domain is given by the ‘ith’ term of equation V.1, which we will call U_i^{3B} :

$$U_i^{3B} = \frac{1}{2} V_{NN} \left(\hat{\mathbf{n}}_{ij} \cdot \hat{\mathbf{n}}_{ik} - \cos\phi_i^{pref} \right)^2 \quad (\text{A.2})$$

The normal vector $\hat{\mathbf{n}}_{ij}$ can be written out as

$$\hat{\mathbf{n}}_{ij} = \frac{(x_j - x_i)\mathbf{x} + (y_j - y_i)\mathbf{y} + (z_j - z_i)\mathbf{z}}{r_{ij}} \quad (\text{A.3})$$

where r_{ij} is the distance between points ‘i’ and ‘j’:

$$r_{ij} = \sqrt{(x_j - x_i)^2 + (y_j - y_i)^2 + (z_j - z_i)^2} \quad (\text{A.4})$$

The dot product between two normal vectors is then given by:

$$\hat{\mathbf{n}}_{ij} \cdot \hat{\mathbf{n}}_{ik} = \frac{(x_j - x_i)(x_k - x_i) + (y_j - y_i)(y_k - y_i) + (z_j - z_i)(z_k - z_i)}{r_{ij}r_{ik}} \quad (\text{A.5})$$

The components of the force on each point can be calculated by taking the derivative of the potential with respect to those components. For example, the x-component of the force on point ‘j’ resulting from the three-body potential at point ‘i’ is given by: $f_{x_j} = -\frac{\partial U_i^{3B}}{\partial x_j} = -V_{NN}(\hat{\mathbf{n}}_{ij} \cdot \hat{\mathbf{n}}_{ik} - \cos\phi_i^{pref}) \frac{\partial(\hat{\mathbf{n}}_{ij} \cdot \hat{\mathbf{n}}_{ik})}{\partial x_j}$. Calculating this derivative gives an expression that includes x, y, and z coordinates of the position for particles i, j, and k. This expression can be used to update the force f_{x_j} in a simulation.

Head-neck Junctionures

If a head is attached to actin, the three-body interactions for the head-neck juncture (points 2 and 8 in fig. 5.3(a), chapter V) are calculated differently than

junctures in the neck domain. One of the structural assumptions of our mechanical model is that the neck domain has a preferred angle of attachment to the head domain with respect to the actin filament (x-axis). We also assume that there is elastic resistance to azimuthal distortion out of the $y = 0$ plane (fig. A.1(b)). In order to impose these assumptions in the simulations, we use a reference point $(x_{ref}, y_{ref}, z_{ref})$ to represent the ‘preferred’ position of the point adjacent to the head-neck juncture (fig. A.1(b)). As discussed in chapter V, we define the mechanical parameters Θ_A and Θ_B to represent the preferred angle of a head-neck juncture with respect to the x-axis before and after phosphate release, respectively. The reference position for point 3 in a three-body interaction at joint 2 with a preferred angle θ_B , for example, would be given by:

$$x_{ref} = x_2 + L_N \cos \theta_B \quad (\text{A.6})$$

$$y_{ref} = 0 \quad (\text{A.7})$$

$$z_{ref} = L_H + L_N \sin \theta_B \quad (\text{A.8})$$

Here, L_H is the length of a head segment (i.e., the distance between points 1 and 2, or between points 8 and 9 in fig. 5.3(a) in chapter V), and L_N is the length of any of the neck domain segments. We assume that an attached head is oriented vertically with respect to the actin filament (i.e., the x-axis).

For a head attached to actin, the elastic potential for a head-neck joint is given by:

$$U_{HN}^{3B} = \frac{1}{2} V_{HN} (\hat{\mathbf{n}}_{ij} \cdot \hat{\mathbf{n}}_{ir} - 1)^2 \quad (\text{A.9})$$

where $\hat{\mathbf{n}}_{ir}$ is the normal vector pointing from the head-neck juncture to the reference point, and $\hat{\mathbf{n}}_{ij}$ is the normal vector pointing from the head-neck juncture ‘i’ to the adjacent point in the neck domain, ‘j’. This potential is minimized when the point ‘j’ is equal to the reference point. This interaction produces forces on points ‘i’ and ‘j’, which are calculated as $f_{x_i} = -\frac{\partial U_{HN}^{3B}}{\partial x_i}$ and $f_{x_j} = -\frac{\partial U_{HN}^{3B}}{\partial x_j}$, for the x-component, and likewise for the y and z components.

Distance Constraints

The polymer model described above assumes that adjacent points in the particle chain are held at fixed distances from each other. We impose this condition by including a harmonic interaction between adjacent particles:

$$U^{Harm} = \frac{1}{2} K (r_{ij} - r_0)^2 \quad (\text{A.10})$$

where K is the harmonic stiffness, r_0 is the rest length, and r_{ij} is the separation distance between adjacent particles ‘i’ and ‘j’ (eq. A.4). An expression for the force on each particle due to the harmonic interaction with an adjacent particle can

be calculated as $f_{x_i} = -\frac{\partial U^{Harm}}{\partial x_i}$, $f_{x_j} = -\frac{\partial U^{Harm}}{\partial x_j}$, and likewise for the y and z components.

In order to keep the inter-particle separation fixed, without significant fluctuations, a high value of the harmonic stiffness K and a very small value of the program time step dt are required. The simulations in chapter V were calculated with $K = 10^5 kT$ and $dt = 10^{-6} \tau$, where $\tau = 1.175 \times 10^{-4} s$ is the program time unit. This choice of parameters ensures a very small variation in separation distance between particles, such that $\langle |r_{ij} - r_0| \rangle < 0.01 r_0$.

First Passage Time for the Diffusional Search of a Detached Head

In order to learn more about the dynamics of the tethered diffusional search of a detached head in the mechano-chemical model in chapter V, a quantity called the first passage time is simulated. The first passage time for the diffusional search of a detached head is defined as the average amount of time from when the head first detaches until it reaches an available binding site through tethered diffusion. This is a mechanical feature of the model and does not encompass the average time for ATP hydrolysis (another requirement for reattachment). First passage times are calculated as follows: The motor is initially equilibrated in mechanical state II (see chapter V text), and then the trailing head is released at time t_0 . If the detached head comes within a distance R_{screen} of a binding site, the time t is recorded and the simulation starts over. The average value of $t - t_0$ over many iterations gives the mean first

passage time for the diffusional search. The binding parameter R_{screen} is set equal to the Debye length for electrostatic screening in a fluid, $R_{screen} = R_{Debye} \approx 0.6nm$ [131], based on the assumption that the head will attach to actin if it comes close enough to a binding site to electrostatically interact with it.

BIBLIOGRAPHY

- [1] J. Howard, *Mechanics of motor proteins and the cytoskeleton* (Sinauer Associates, Inc., Sunderland, MA, 2001).
- [2] A. Yildiz, J. N. Forkey, S. A. McKinney, T. Ha, Y. E. Goldman, and P. R. Selvin, *Science* **300**, 2061 (2003).
- [3] A. Huxley, *Prog. Biophys. Biophys. Chem.* **7**, 255 (1957).
- [4] S. Leibler and D. Huse, *J. Cell. Biol.* **389**, 1357 (1993).
- [5] T. Duke and S. Leibler, *Biophys. J.* **71**, 1235 (1996).
- [6] A. Vilfan, E. Frey, and F. Schwabl, *Eur. Phys. J. B* **3**, 535 (1998).
- [7] M. Magnasco, *Phys. Rev. Lett.* **71**, 1477 (1993).
- [8] R. D. Astumian and M. Bier, *Biophys. J.* **70**, 637 (1996).
- [9] R. D. Astumian, *Science* **276**, 917 (1997).
- [10] G. N. Stratopoulos, T. E. Dialynas, and G. P. Tsironis, *Phys. Lett. A* **252**, 151 (1999).
- [11] H. Wang and G. Oster, *Appl. Phys. A* **75**, 315 (2002).
- [12] B. Geislinger and R. Kawai, *Phys. Rev. E* **74**, 011912 (2006).
- [13] A. L. R. Bug and B. J. Berne, *Phys. Rev. Lett.* **59**, 948 (1987).
- [14] A. Ajdari and J. Prost, *C. R. Acad. Sci., Ser. II: Mec., Phys., Chim., Sci. Terre Univers* **315**, 1635 (1992).
- [15] J. Prost, J. F. Chauwin, L. Peliti, and A. Ajdari, *Phys. Rev. Lett.* **72**, 2652 (1994).
- [16] E. M. Craig, M. J. Zuckermann, and H. Linke, *Phys. Rev. E* **73**, 051106 (2006).
- [17] E. M. Craig, B. R. Long, J. M. R. Parrondo, and H. Linke, *Europhys. Lett.* **81**, 10002 (2008).

- [18] E. M. Craig, N. J. Kuwada, B. J. Lopez, and H. Linke, *Ann. Phys. (Berlin)* **17**, 115 (2008).
- [19] H. Linke, M. T. Downton, and M. J. Zuckermann, *Chaos* **15**, 026111 (2005).
- [20] P. Hänggi and R. Bartussek, *Lect. Notes Phys.* **476**, 294 (1996).
- [21] R. D. Astumian and P. Hänggi, *Phys. Today* **55**, 33 (2002).
- [22] P. Reimann, *Phys. Rep.* **361**, 57 (2002).
- [23] P. Reimann and P. Hänggi, *Appl. Phys. A: Mater. Sci. Process.* **75**, 169 (2002).
- [24] E. Fermi, *Thermodynamics* (Dover Publications, Inc., New York, 1936).
- [25] L. D. Landau and E. M. Lifshitz, *Statistical Physics: Course of Theoretical Physics, Volume 5* (Nauka, Moscow, 1976).
- [26] R. D. Astumian and M. Bier, *Fluctuation driven ratchets: molecular motors* **72**, 1766 (1994).
- [27] P. Jung, J. G. Kissner, and P. Hänggi, *Phys. Rev. Lett.* **76**, 3436 (1996).
- [28] J. L. Mateos, *Phys. Rev. Lett.* **84**, 258 (2000).
- [29] J. L. Mateos, *Acta Phys. Pol. B* **32**, 307 (2001).
- [30] M. Barbi and M. Salerno, *Phys. Rev. E* **62**, 1988 (2000).
- [31] P. Reimann, R. Bartussek, R. Häussler, and P. Hänggi, *Phys. Lett. A* **215**, 26 (1996).
- [32] M. Kostur and J. Luczka, *Phys. Rev. E* **63**, 021101 (2001).
- [33] A. Ajdari, *J. Phys. I France* **4**, 1577 (1994).
- [34] J.-D. Bao and Y.-S. Zhuo, *Phys. Lett. A* **239**, 228 (1998).
- [35] Y. Aghababaie, G. I. Menon, and M. Plischke, *Phys. Rev. E* **59**, 2578 (1999).
- [36] Y. Li, X. Wu, and Y. Zhuo, *Mod. Phys. Lett. B* **14**, 479 (2000).
- [37] A. Igarashi, S. Tsukamoto, and H. Goko, *Phys. Rev. E* **64**, 051908 (2001).
- [38] S. Klumpp, A. Mielke, and C. Wald, *Phys. Rev. E* **63**, 031914 (2001).
- [39] D. Dan, A. M. Jayannavar, and G. I. Menon, *Physica A* **318**, 40 (2003).
- [40] H.-Y. Wang and J.-D. Bao, *Physica A* **337**, 13 (2004).

- [41] M. T. Downton, M. J. Zuckermann, E. M. Craig, M. Plischke, and H. Linke, *Phys. Rev. E* **73**, 011909 (2006).
- [42] F. Jülicher and J. Prost, *Phys. Rev. Lett.* **75**, 2618 (1995).
- [43] F. Jülicher and J. Prost, *Phys. Rev. Lett.* **78**, 4510 (1997).
- [44] Z. Csahók, F. Family, and T. Vicsek, *Phys. Rev. E* **55**, 5179 (1997).
- [45] T. C. Elston and C. S. Peskin, *SIAM J. Appl. Math.* **61**, 776 (2000).
- [46] M. Badoual, F. Jülicher, and J. Prost, *PNAS* **99**, 6696 (2002).
- [47] A. Igarashi, H. Goko, and S. Tsukamoto, *Physica A* **325**, 62 (2003).
- [48] Y. Shu and H. Shi, *Phys. Rev. E* **69**, 021912 (2004).
- [49] H. Goko and A. Igarashi, *Phys. Rev. E* **71**, 061108 (2005).
- [50] K. B. Zeldovich, J.-F. Joanny, and J. Prost, *Eur. Phys. J. E* **17**, 155 (2005).
- [51] B. J. Lopez, N. J. Kuwada, E. M. Craig, B. R. Long, and H. Linke, manuscript in preparation for *Phys. Rev. Lett.* (2008).
- [52] R. Nambiar, A. Gajraj, and J. C. Meiners, *Biophys. J.* **87**, 1972 (2004).
- [53] J. C. Crocker, J. A. Matteo, A. D. Dinsmore, and A. G. Yodh, *Phys. Rev. Lett.* **82**, 4352 (1999).
- [54] C. Lutz, M. Kollmann, P. Leiderer, and C. Bechinger, *J. Phys., Condens. Matter* **16**, S4075 (2004).
- [55] L. P. Faucheux, L. S. Bourdieu, P. D. Kaplan, and A. J. Libchaber, *Phys. Rev. Lett.* **74**, 1504 (1995).
- [56] K. Gopalsamy, *Stability and Oscillations in Delay Differential Equations of Population Dynamics* (Kluwer Academic Publishers, Dordrecht, The Netherlands, 1992).
- [57] D. F. Hendry, *Oxford Econ. Pap., New Ser.* **40**, 132 (1988).
- [58] S. Nitzan and J. Paroush, *Collective decision making: an economic outlook* (Cambridge University Press, Cambridge, 1985).
- [59] J. M. R. Parrondo, L. Dinis, E. Garcia-Torano, and B. Sotillo, *Eur. Phys. J. Special Topics* **143**, 39 (2007).
- [60] G. P. Harmer and D. Abbott, *Nature* **402**, 864 (1999).

- [61] J. M. R. Parrondo and L. Dinis, *Cont. Phys.* **45**, 147 (2004).
- [62] L. Dinis, *Phys. Rev. E* **77**, 021124 (2008).
- [63] S. R. Neves and R. Iyengar, *BioEssays* **24**, 1110 (2002).
- [64] M. V. Smoluchowski, *Phys. Z* **13**, 1069 (1912).
- [65] R. P. Feynman, R. B. Leighton, and M. Sands, *The Feynman Lectures on Physics* (Addison-Wesley, Reading, MA, 1963).
- [66] H. S. Leff and A. F. Rex, *Maxwell's Demon: Entropy, Information, Computing* (Taylor and Francis, Ltd., United Kingdom, 2002).
- [67] H. Touchette and S. Lloyd, *Phys. Rev. Lett.* **84**, 1156 (2000).
- [68] T. M. Cover and J. A. Thomas, *Elements of Information Theory* (Wiley, New York, 1991).
- [69] F. J. Cao, L. Dinis, and J. M. R. Parrondo, *Phys. Rev. Lett.* **93**, 040603 (2004).
- [70] M. P. Allen and D. J. Tildesley, *Computer simulation of liquids* (Oxford University Press, Inc., New York, 1987).
- [71] A. Einstein, *Annalen der Physik* **19**, 371 (1906).
- [72] A. D. Fokker, *Annalen der Physik* **43**, 810 (1914).
- [73] M. Planck, *Sitz. ber. Preuss. Akad. Wiss.* pp. 324–341 (1917).
- [74] L. Dinis, J. M. R. Parrondo, and F. J. Cao, *Europhys. Lett.* **71**, 536 (2005).
- [75] M. Feito and F. J. Cao, *Eur. Phys. J. B* **59**, 1434 (2007).
- [76] F. J. Cao, M. Feito, and H. Touchette, *Arxiv preprint: cond-mat/0703492* (2008).
- [77] M. Feito and F. J. Cao, *Phys. Rev. E* **76**, 061113 (2007).
- [78] S. L. Reck-Peterson, D. W. Provance, M. S. Mooseker, and J. A. Mercer, *Biochim. Biophys. Acta.* **1496**, 36 (2000).
- [79] R. D. Vale, *Cell* **112**, 467 (2003).
- [80] Y. Lecarpentier, D. Chemla, J. C. Pournay, F.-X. Blanc, and C. Coirault, *J. Appl. Physiol.* **91**, 2479 (2001).
- [81] J. R. Sellers and C. Veigel, *Current Opinion in Cell Biology* **18**, 68 (2006).

- [82] A. D. Mehta, R. S. Rock, M. Rief, J. A. Spudich, M. S. Mooseker, and R. E. Cheney, *Nature* **400**, 590 (1999).
- [83] T. Sakamoto, I. Amitani, E. Yokota, and T. Ando, *Biochem. Biophys. Res. Commun.* **272**, 586 (2000).
- [84] J. R. Moore, E. B. Krementsova, K. M. Trybus, and D. M. Warsaw, *Journal of Cell Biology* **155**, 625 (2001).
- [85] C. Veigel, F. Wang, M. L. Bartoo, J. R. Sellers, and J. E. Molloy, *Nature Cell Biology* **4**, 59 (2002).
- [86] R. D. Vale, *The Journal of Cell Biology* **163**, 445 (2003).
- [87] J. R. Sellers and C. Veigel, *Current Opinion in Cell Biology* **18**, 68 (2006).
- [88] D. M. Warshaw, G. G. Kennedy, S. S. Work, E. B. Krementsova, S. Beck, and K. M. Trybus, *Biophys. J.* **88**, L30 (2005).
- [89] M. Y. Ali, S. Uemera, K. Adachi, H. Itoh, K. Kinoshita, and S. Ishiwata, *PNAS* **102**, 1419 (2005).
- [90] M. Rief, R. S. Rock, A. D. Mehta, M. S. Mooseker, R. E. Cheney, and J. A. Spudich, *PNAS* **97**, 9482 (2000).
- [91] S. Uemera, H. Higuchi, A. O. Olivares, E. M. D. L. Cruz, and S. Ishiwata, *Nat Struct Mol Biol* **9**, 877 (2004).
- [92] A. E. Clemen, M. Vilfan, J. Jaud, J. Zhang, M. Barmann, and M. Rief, *Biophys. J* **88**, 4402 (2005).
- [93] T. J. Purcell, C. Morris, J. A. Spudich, and H. L. Sweeney, *PNAS* **99**, 14159 (2002).
- [94] H. Tanaka, K. Homma, A. H. Iwane, E. Katayama, R. Ikebe, J. Saito, T. Yanagida, and M. Ikebe, *Nature* **415**, 192 (2002).
- [95] T. Sakamoto, A. Yildiz, P. R. Selvin, and J. R. Sellers, *Biochemistry* **44**, 16203 (2005).
- [96] G. E. Snyder, T. Sakamoto, J. A. Hammer, J. R. Sellers, and P. R. Selvin, *Biophys. J.* **87**, 1776 (2004).
- [97] E. M. D. L. Cruz, A. L. Wells, H. L. Sweeney, and E. M. Ostap, *Biochemistry* **39**, 14196 (2000).

- [98] G. Cappello, P. Pierobon, C. Symonds, L. Busoni, J. C. M. Gebhardt, M. Rief, and J. Prost, *PNAS* **104**, 15328 (2008).
- [99] L. Busoni, A. Dornier, J.-L. Viovy, J. Prost, and G. Cappello, *Journal of Applied Physics* **98**, 064302.1 (2005).
- [100] A. R. Dunn and J. A. Spudich, *Nature Structural and Molecular Biology* **14**, 246 (2007).
- [101] T. Sakamoto, F. Wang, S. Schmitz, Y. H. Xu, Q. Xu, J. E. Molloy, C. Veigel, and J. R. Sellers, *Journal of Biological Chemistry* **278**, 29201 (2003).
- [102] C. Veigel, S. Schmitz, F. Wang, and J. R. Sellers, *Nature Cell Biology* **7**, 861 (2005).
- [103] S. Burgess, M. Walker, F. Wang, J. R. Sellers, H. D. White, P. J. Knight, and J. Trinick, *Journal of Cell Biology* **159**, 983 (2002).
- [104] T. Ando, N. Kodera, E. Takai, D. Maruyama, K. Saito, and A. Toda, *PNAS* **98**, 12468 (2001).
- [105] K. Shiroguchi and K. Kinosita, *Science* **316**, 1208 (2007).
- [106] E. M. D. L. Cruz, A. L. Wells, S. S. Rosenfeld, E. M. Ostap, and H. L. Sweeney, *PNAS* **96**, 13726 (1999).
- [107] M. Y. Ali, S. Uemera, K. Adachi, H. Itoh, K. Kinosita, and S. Ishiwata, *Nat. Struct. Biol.* **9**, 464 (2004).
- [108] J. N. Forkey, M. E. Quinlan, M. A. Shaw, J. E. Corrie, and Y. E. Goldman, *Nature* **422**, 399 (2003).
- [109] J. E. Baker, L. B. Krementsova, G. G. Kennedy, A. Armstrong, K. M. Trybus, D. M. Warshaw, and T. D. Pollard, *PNAS* **101**, 5542 (2004).
- [110] T. J. Purcell, H. L. Sweeney, and J. A. Spudich, *PNAS* **102**, 13873 (2005).
- [111] K. M. Trybus, *Nature Cell Biology* **7**, 861 (2005).
- [112] M. L. Walker, S. A. Burgess, J. R. Sellers, F. Wang, J. A. Hammer, J. Trinick, and P. J. Knight, *Nature* **405**, 804 (2000).
- [113] S. S. Rosenfeld and H. L. Sweeney, *Journal of Biological Chemistry* **279**, 40100 (2004).
- [114] D. L. Ermak, *Rapport d'activite scientifique du CECAM* pp. 66–81 (1976).

- [115] D. L. Ermak and H. Buckholtz, *Journal of Computational Physics* **35**, 169 (1980).
- [116] A. Y. Grosberg and A. R. Khokhlov, *Statistical Physics of Macromolecules* (American Institute of Physics, Woodbury, NY, 1994).
- [117] A. Einstein, *Annalen der Physik* **17**, 549 (1905).
- [118] M. Smoluchowski, *Annalen der Physik* **21**, 756 (1906).
- [119] B. R. Long, Ph.D. thesis, University of Oregon, Eugene, Oregon (2008).
- [120] A. E. Cohen and W. E. Moerner, *PNAS* **103**, 4362 (2006).
- [121] A. B. Kolomeisky and M. E. Fisher, *Biophys. J.* **84**, 1642 (2003).
- [122] M. E. Fisher and A. B. Kolomeisky, *PNAS* **96**, 6597 (1999).
- [123] A. Vilfan, *Biophys. J.* **88**, 3792 (2005).
- [124] G. Lan and S. X. Sun, *Biophys. J.* **88**, 999 (2005).
- [125] C. M. Yengo and H. L. Sweeney, *Biochemistry* **41**, 8508 (2002).
- [126] C. M. Yengo and H. L. Sweeney, *Biochemistry* **43**, 2605 (2004).
- [127] R. E. Cheney, [others], and M. S. Mooseker, *Cell* **75**, 13 (1993).
- [128] J. Howard, *Nature* **389**, 561 (1997).
- [129] M. Terrak, G. Rebowski, R. C. Lu, Z. Grabarek, and R. Dominguez, *PNAS* **102**, 12718 (2005).
- [130] F. Wang, K. Thirumurugan, W. F. Stafford, J. A. Hammer, P. J. Knight, and J. R. Sellers, *Virtual Journal of Biological Chemistry* **279**, 2333 (2003).
- [131] N. J. Cordova, B. Ermentrout, and G. F. Oster, *PNAS* **89**, 339 (1992).
- [132] M. Doi and S. F. Edwards, *The theory of polymer dynamics* (Oxford University Press, New York, 1986).
- [133] J. Liu, D. W. Taylor, E. B. Kremenstova, K. M. Trybus, and K. A. Taylor, *Nature* **442**, 208 (2006).
- [134] C. Bustamante, Z. Bryant, and S. B. Smith, *Nature* **421**, 423 (2003).
- [135] A. Baba and T. Komatsuzaki, *PNAS* **104**, 19297 (2007).

- [136] R. Friedrich, S. Siegert, J. Peinke, S. Lück, M. Siefert, M. Lindemann, J. Raethjen, G. Deuschl, and G. Pfister, *Physics Letters A* **271**, 217 (2000).
- [137] S. P. Gross, *Phys. Biol.* **1**, R1 (2004).
- [138] M. A. Welte, *Curr. Biol.* **14**, R525 (2004).
- [139] C. Kural, H. Kim, S. Syed, G. Goshima, V. Gelfand, and P. R. Selvin, *Science* **308**, 1469 (2005).
- [140] A. Gennerich and D. Schild, *Phys. Biol.* **3**, 45 (2006).
- [141] V. Levi, A. S. Serpinskaya, E. Gratton, and V. Gelfand, *J. Cell. Biol.* **90**, 318 (2006).
- [142] M. Y. Ali, H. Lu, C. S. Bookwater, D. M. Warshaw, and K. M. Trybus, *PNAS* **105**, 4691 (2008).
- [143] M. Müller, S. Klumpp, and R. Lipowsky, *PNAS* **105**, 4609 (2008).
- [144] J. Snider, F. Lin, N. Zahedi, V. Rodionov, C. C. Yu, and S. P. Gross, *PNAS* (2004).
- [145] J. L. Ross, H. Shuman, E. L. F. Holzbaur, and Y. E. Goldman, *Biophys. J.* **94**, 3115 (2008).
- [146] J. L. Ross, M. Y. Ali, and D. M. Warshaw, *Curr. Opin. Cell Biol.* **20**, 41 (2008).
- [147] A. Vilfan, *PNAS* **94**, 3405 (2008).